

NASA/TP-2000-210640



# Parameterized Cross Sections for Pion Production in Proton-Proton Collisions

*Steve R. Blattnig, Sudha R. Swaminathan, Adam T. Kruger, Moussa Ngom, and  
John W. Norbury  
University of Wisconsin-Milwaukee  
Milwaukee, Wisconsin*

*R. K. Tripathi  
Langley Research Center  
Hampton, Virginia*

---

December 2000

## The NASA STI Program Office . . . in Profile

Since its founding, NASA has been dedicated to the advancement of aeronautics and space science. The NASA Scientific and Technical Information (STI) Program Office plays a key part in helping NASA maintain this important role.

The NASA STI Program Office is operated by Langley Research Center, the lead center for NASA's scientific and technical information. The NASA STI Program Office provides access to the NASA STI Database, the largest collection of aeronautical and space science STI in the world. The Program Office is also NASA's institutional mechanism for disseminating the results of its research and development activities. These results are published by NASA in the NASA STI Report Series, which includes the following report types:

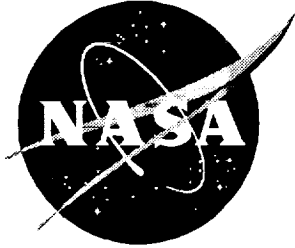
- **TECHNICAL PUBLICATION.** Reports of completed research or a major significant phase of research that present the results of NASA programs and include extensive data or theoretical analysis. Includes compilations of significant scientific and technical data and information deemed to be of continuing reference value. NASA counterpart of peer-reviewed formal professional papers, but having less stringent limitations on manuscript length and extent of graphic presentations.
- **TECHNICAL MEMORANDUM.** Scientific and technical findings that are preliminary or of specialized interest, e.g., quick release reports, working papers, and bibliographies that contain minimal annotation. Does not contain extensive analysis.
- **CONTRACTOR REPORT.** Scientific and technical findings by NASA-sponsored contractors and grantees.
- **CONFERENCE PUBLICATION.** Collected papers from scientific and technical conferences, symposia, seminars, or other meetings sponsored or co-sponsored by NASA.
- **SPECIAL PUBLICATION.** Scientific, technical, or historical information from NASA programs, projects, and missions, often concerned with subjects having substantial public interest.
- **TECHNICAL TRANSLATION.** English-language translations of foreign scientific and technical material pertinent to NASA's mission.

Specialized services that complement the STI Program Office's diverse offerings include creating custom thesauri, building customized databases, organizing and publishing research results . . . even providing videos.

For more information about the NASA STI Program Office, see the following:

- Access the NASA STI Program Home Page at <http://www.sti.nasa.gov>
- Email your question via the Internet to [help@sti.nasa.gov](mailto:help@sti.nasa.gov)
- Fax your question to the NASA STI Help Desk at (301) 621-0134
- Telephone the NASA STI Help Desk at (301) 621-0390
- Write to:  
NASA STI Help Desk  
NASA Center for AeroSpace Information  
7121 Standard Drive  
Hanover, MD 21076-1320

NASA/TP-2000-210640



# Parameterized Cross Sections for Pion Production in Proton-Proton Collisions

*Steve R. Blattnig, Sudha R. Swaminathan, Adam T. Kruger, Moussa Ngom, and  
John W. Norbury  
University of Wisconsin-Milwaukee  
Milwaukee, Wisconsin*

*R. K. Tripathi  
Langley Research Center  
Hampton, Virginia*

National Aeronautics and  
Space Administration

Langley Research Center  
Hampton, Virginia 23681-2199

---

December 2000

## Acknowledgments

The authors would like to thank Sean Ahern and Alfred Tang, University of Wisconsin-Milwaukee, for their help on this project. Blattnig was supported by the Wisconsin Space Grant Consortium, NASA grant NCC-1-260, and NASA Graduate Student Researchers Program Fellowship NGT-52217. Kruger and Ngom were supported by the Wisconsin Space Grant Consortium, NASA grant NCC-1-260, and NSF grant PHY-9507740. Norbury and Swaminathan were supported by NASA grants NCC-1-260 and NCC-1-354.

---

Available from:

NASA Center for Aerospace Information (CASI)  
7121 Standard Drive  
Hanover, MD 21076-1320  
(301) 621-0390

National Technical Information Service (NTIS)  
5285 Port Royal Road  
Springfield, VA 22161-2171  
(703) 605-6000

## Nomenclature

COM center of momentum

$\frac{d\sigma}{dE}$  spectral distribution,  $2\pi p \int_0^{\theta_{max}} d\theta E \frac{d^3\sigma}{dp^3} \sin\theta$

$E$  pion total energy

$E_{cm}$  center of momentum energy

$E \frac{d^3\sigma}{dp^3}$  LIDCS

EAS extensive air shower

LIDCS Lorentz invariant differential cross section

$m_p$  proton mass

$m_\pi$  pion mass

$P_p$  proton momentum

$p$  pion momentum

$p_{max}$  maximum possible momentum scattered pion can have for given  $\sqrt{s}$

$p_\perp$  pion transverse momentum,  $p \sin\theta$

$\sqrt{s}$  magnitude of center of momentum frame four momentum, equal to total energy in center of momentum frame

$T$  pion kinetic energy

$T_{lab}$  laboratory frame kinetic energy of incoming proton

$\theta$  angle of pion scattering with respect to direction of incident particle

$\sigma$  total cross section,  $2\pi \int_0^{\theta_{max}} d\theta \int_{p_{min}}^{p_{max}} dp E \frac{d^3\sigma}{dp^3} \frac{p^2 \sin\theta}{\sqrt{p^2 + m_\pi^2}}$

Quantities with an asterisk (e.g.,  $\theta^*$ ) refer to the quantities in the center of momentum frame, whereas quantities without an asterisk (e.g.,  $\theta$ ) refer to the quantities in the laboratory frame.



## Abstract

*An accurate knowledge of cross sections for pion production in proton-proton collisions finds wide application in particle physics, astrophysics, cosmic ray physics, and space radiation problems, especially in situations where an incident proton is transported through some medium and knowledge of the output particle spectrum is required when given the input spectrum. In these cases, accurate parameterizations of the cross sections are desired. In this paper much of the experimental data are reviewed and compared with a wide variety of different cross section parameterizations. Therefore, parameterizations of neutral and charged pion cross sections are provided that give a very accurate description of the experimental data. Lorentz invariant differential cross sections, spectral distributions, and total cross section parameterizations are presented.*

## 1. Introduction

Pion production in proton-proton collisions has been extensively studied for many years; this knowledge now finds useful applications in a variety of areas as follows:

1. Two important types of particle detectors are the hadronic and electromagnetic calorimeters (ref. 1) where an electromagnetic or hadronic shower is initiated by a high-energy incoming particle; from a Monte-Carlo simulation of the shower, one is able to deduce important characteristics of the incoming particle such as its energy and identity
2. The primary cosmic rays can be detected by a variety of methods, depending on the incident energy; for the very high-energy cosmic rays, where the flux is relatively low, the extensive air showers (EAS's) (refs. 2, 3, and 4) provide the most convenient means of detection; the EAS is analogous to the hadronic or electromagnetic calorimeter used in particle physics but with the atmosphere of the Earth being the active volume in which the shower develops; the EAS has both electromagnetic and hadronic components, and similar to the calorimeter, the energy and identity of primary cosmic ray nuclei can be deduced via Monte-Carlo simulation of the showers (refs. 2 and 3)
3. In long-duration human space flights, such as a mission to Mars, the radiation levels induced by galactic cosmic rays can exceed exposure limits set for astronauts (refs. 5 and 6); in determining the radiation environment inside a spacecraft, one needs to transport the exterior cosmic ray spectrum through the spacecraft wall to determine the interior radiation spectrum
4. In gamma ray (refs. 7 and 8) and high-energy neutrino astronomy (refs. 9 and 10), the diffuse background radiation is due in large part to the gamma rays and neutrinos produced in proton collisions with the protons in the interstellar medium; in addition, pion production from proton-proton collisions finds applications in the calculation of gamma ray emission from the accretion disk around a black hole (ref. 11)

In all these applications, having an accurate knowledge of the cross sections for pion production in proton-proton collisions is crucial. In addition, most of the applications mentioned require solving the transport equations that determine the particle spectrum on one side of a material (active volume of calorimeter, atmosphere of Earth, spacecraft wall, or interstellar medium) given the incident particle spectrum. Use of pion production cross sections in such transport codes requires that the cross section be written in a simple form. The transport codes have many iterative loops, which will take too much computer time if the cross section formulas also contain many iterative loops. Thus it is most advantageous if one can write down simple

formulas which parameterize all experimental data on pion production cross sections; this is the aim of the present work.

In this paper, simple algebraic parameterizations of charged and neutral pion production cross sections valid over a range of energies are presented. The cross sections provided are Lorentz invariant differential cross sections (LIDCS's), laboratory frame spectral distributions (i.e., energy differential cross sections), and total cross sections because they are the types of cross sections most widely used in transport equations. Many such parameterizations have been presented before, but the problem is deciding which are correct and whether a particular parameterization applies only to a limited data set or is valid over a wider range. In the present work, an exhaustive data search has been performed, and as many different parameterizations as possible have been compared with as much data as possible so that definitive conclusions could be reached concerning which is the most accurate parameterization to use.

The cross sections discussed in this paper are for inclusive pion production in proton-proton collisions; that is, the reactions considered are  $p + p \rightarrow \pi + X$ , where  $p$  represents a proton,  $\pi$  represents a pion, and  $X$  represents any combination of particles. An extensive search for LIDCS data was performed, and the data were used to compare all available parameterizations. A method for generating parameterizations for these cross sections is also described and applied to  $\pi^0$  production. Spectral distribution and total cross section formulas were not developed directly because of lack of data. Instead, the most successful LIDCS parameterizations were first transformed into laboratory frame spectral distributions by numerical integration. These spectral distributions were parameterized and then numerically integrated to generate laboratory frame total cross sections. Finally, the total cross sections were compared with available data and parameterized as well. This procedure is discussed, and the parameterizations of the numerical results are given. Multiple checks of the accuracy of all results were made, and some of them are presented.

Finally, there are a lot of figures in this paper. What often happens when various authors come up with a parameterization is that they only apply it to a limited data set. Often when a particular parameterization is applied to other data, it does not work; this is the reason for the large number of figures in the present paper. The aim is to show that the parameterizations in this paper do apply well to a whole range of experimental data.

The derivation of the maximum momentum is presented in appendix A. The kinematic relations between the two reference frames— the center of mass and the laboratory frames— are presented in appendix B. Appendix C presents a synopsis of data transformations.

## 2. Comparison of Lorentz Invariant Differential Cross Sections

The object is to determine an accurate parameterization for inclusive LIDCS's, which can be confidently applied to regions where no experimental data are available. For example, if the formulas were to be used for the purpose of developing radiation shielding materials, the parametric equation would need to be extrapolated to energies lower than those for which data are available. The most convenient formulas are those that are in closed form, since they are easily used and take relatively little computer time in numerical calculations. Some of the formulas that were considered as representations of the LIDCS's were not in closed form but included tabulated functions of energy (i.e., numerical values were given for specific energy values rather than a functional form). When comparing parameterizations, closed-form expressions were given precedence over other equally accurate formulas.

The invariant single-particle distribution is defined by

$$f(AB \rightarrow CX) \equiv E_C \frac{d^3\sigma}{dp_C^3} \equiv E \frac{d^3\sigma}{dp^3} = \frac{E}{p^2} \frac{d^3\sigma}{dp d\Omega} \quad (1)$$

where  $\frac{d^3\sigma}{dp_C^3}$  is the differential cross section (i.e., the probability per unit incident flux) for

detecting a particle  $C$  within the phase-space volume element  $dp_C^3$ ,  $A$  and  $B$  are the initial colliding particles,  $C$  is the produced particle of interest,  $X$  represents all other particles produced in the collision,  $E$  is the total energy of the produced particle  $C$ , and  $\Omega$  is the solid angle. This form (eq. (1)) is favored because the quantity is invariant under Lorentz transformations.

The data for pion production in proton-proton interactions are primarily reported in terms of the kinematic variables,  $\theta^*$ ,  $\sqrt{s}$ , and  $p_\perp$ , which are, respectively, the center of momentum (COM) frame scattering angle, the invariant mass, and the transverse momentum of the produced pion. The mass  $\sqrt{s}$  is a Lorentz invariant quantity and is equal to the total energy in the COM frame;  $p_\perp \equiv p^* \sin \theta^*$ , where  $p^*$  is the COM momentum;  $p_\perp$  is invariant under the transformation from the laboratory (lab) frame to the COM frame. (See appendix B for a more detailed discussion of kinematic variables.) All momenta, energies, and masses are in gigaelectron volts.

## 2.1. Neutral Pions

Büsser et al. (ref. 12) have fitted the LIDCS data obtained in the reaction  $p + p \rightarrow \pi^0 + X$  (where  $p$  represents a proton,  $\pi^0$  represents the neutral pion produced, and  $X$  represents all other produced particles) to an equation of the form

$$E \frac{d^3\sigma}{dp^3} = A p_\perp^{-n} \exp\left(-b \frac{p_\perp}{\sqrt{s}}\right) \quad (2)$$

with  $A = 1.54 \times 10^{-26}$ ,  $n = 8.24$ , and  $b = 26.1$ . Equation (2) is based on a specific set of experimental data with all measurements taken at  $\theta^* \approx 90^\circ$  and was originally intended only for pions with high  $p_\perp$ . Comparison of this parameterization with data available from other experiments (refs. 13 to 19) indicates that the global behavior of the invariant cross section cannot be represented by a function of this form. (See figs. 1 to 96.) The parameterization of Büsser et al. (ref. 12) was not plotted because the cross section is much too small in the  $p_\perp$  range covered by the graph.

The following form has been used by Albrecht et al. (ref. 20) to represent neutral pion production:

$$E \frac{d^3\sigma}{dp^3} = C \left( \frac{p_0}{p_\perp + p_0} \right)^n \quad (3)$$

where  $C$ ,  $n$ , and  $p_0$  are free parameters. Because this equation only has dependence on  $p_\perp$  when the data (refs. 13 to 19) shown in figures 1 to 96 also have dependence on  $\sqrt{s}$  and  $\theta^*$ , this form is not general enough to represent all the data.

Many authors (e.g., ref. 21) have favored a representation for the invariant cross section of the form

$$E \frac{d^3\sigma}{dp^3} = A \left( p_\perp^2 + M^2 \right)^{-N/2} f(x_\perp, \theta^*) \quad (4)$$

where  $f(x_\perp, \theta^*) = (1 - x_\perp)^F$ ,  $N$  and  $F$  are free parameters, the scaling variable  $x_\perp$  is given by  $x_\perp = \frac{p_\perp}{p_\perp^*} \approx \frac{2p_\perp}{\sqrt{s}}$ , and

$$p_\perp^* = \left[ \frac{(s + m_\pi^2 - 4m_p^2)^2}{4s - m_\pi^2} \right]^{1/2}$$

where  $m_\pi$  and  $m_p$  are the mass of the neutral pion and the proton, respectively. (See appendix A for details on  $p_\perp^*$ .) The outline of this basic form has been used by Carey et al. in fitting

the invariant cross section for the inclusive reaction  $p + p \rightarrow \pi^0 + X$ . (See ref. 22.) Their representation is given by

$$E \frac{d^3\sigma}{dp^3} = A (p_{\perp}^2 + 0.86)^{-4.5} (1 - x_R^*)^4 \quad (5)$$

where  $x_R^* = \frac{p^*}{p_{\text{max}}^*}$  is the radial scaling variable and the normalization constant  $A$  has been determined as  $A \approx 5$ . This parameterization accurately reproduces the data for measurements taken at  $\theta^* = 90^\circ$  and  $\sqrt{s} \geq 9.8$  GeV but does not agree well with the data for smaller angles and  $\sqrt{s} = 7$  GeV as can be seen in figures 1 to 96.

Another problem with this parameterization becomes apparent, when one considers that integration over all allowed angles and outgoing particle momenta should yield the total inclusive cross section. The details of this calculation appear in section 3. A comparison of the experimentally determined total cross section data from Whitmore (ref. 23) with the results of the numerical integration of equation (5) shows that the total cross section is greatly underestimated by Carey. (See fig. 5.)

Stephens and Badhwar (ref. 19) obtained data from the photon cross sections given by Fidecaro et al. (ref. 13), which were taken at incident proton kinetic energy of  $T_{\text{lab}} = 23$  GeV and  $p_{\perp} = 0.1 - 1.0$  GeV. (Note: No error was listed by Fidecaro et al. for pion production. Error bars of 10 percent were added to the data in the figures because this level of error was standard for most other data. Also, Stephens and Badhwar use the notation  $E_p$  instead of  $T_{\text{lab}}$ .) Figures 1 to 96 demonstrate the accuracy of the parameterization of Stephens and Badhwar in this region as well as other regions. The parameterization of the  $\pi^0$  invariant cross section proposed by Stephens and Badhwar (ref. 19) is presented as follows:

$$E \frac{d^3\sigma}{dp^3} = Af(T_{\text{lab}})(1 - \tilde{x})^q \exp\left(-\frac{Bp_{\perp}}{1 + 4m_p^2/s}\right) \quad (6)$$

where

$$\tilde{x} = \sqrt{(x_{\parallel}^*)^2 + \left(\frac{4}{s}\right)(p_{\perp}^2 + m_{\pi}^2)}$$

$$q = \frac{C_1 - C_2 p_{\perp} + C_3 p_{\perp}^2}{\sqrt{1 + 4m_p^2/s}}$$

$$f(T_{\text{lab}}) = \left(1 + 23T_{\text{lab}}^{-2.6}\right) \left(\frac{1 - 4m_p^2}{s}\right)^2$$

and  $A = 140$ ,  $B = 5.43$ ,  $C_1 = 6.1$ ,  $C_2 = 3.3$ ,  $C_3 = 0.6$  with  $x_{\parallel}^* \equiv \frac{p_{\parallel}^*}{p_{\text{max}}^*}$ , and  $p_{\parallel}^* = p^* \cos\theta^*$ .

The Stephens-Badhwar parameterization was found to be the best of the previously mentioned representations because it accurately reproduces the data in the low  $p_{\perp}$  region, where the cross section is greatest (figs. 1 to 4), and its integration yields accurate values for the total cross section (fig. 5). Equation (6) is, however, a poor tool for predicting values of the invariant cross section for  $p_{\perp} \geq 2$  GeV because the value predicted underestimates experimental data by  $\approx 10$  orders of magnitude. (See figs. 6 and 7.)

No parameterization currently exists that accurately fits the global behavior of the LIDCS data. Previous equations have suffered from being too specific to a particular set of experimental

data or from failing to reproduce the total cross section upon integration. For these reasons, a new parameterization is desired—one that correctly predicts all available data while maintaining the essential quality of correctly producing the total cross section upon integration.

The approach adopted in the present work is to assume the following form for the invariant cross section:

$$E \frac{d^3\sigma}{dp^3} = (\sin \theta^*)^D (\sqrt{s}, p_\perp, \theta^*) F(\sqrt{s}, p_\perp, \theta^* = 90^\circ) \quad (7)$$

The motivation for an equation of this form is that as the angle decreases, the cross section decreases very slowly at lower  $p_\perp$  values. The approximation that was made in deriving equation (7) is that as  $p_\perp \rightarrow 0$ , the cross section is assumed to be independent of the angle.

Under the assumption that the invariant cross section can be fitted by equation (7), the program goes as follows. Find a representation for the cross section as a function of energy  $\sqrt{s}$  and transverse momentum  $p_\perp$  from experimental data taken at  $\theta^* = 90^\circ$ . The quantity  $F(\sqrt{s}, p_\perp)$  is then completely determined because  $(\sin \theta^*)^D$  is unity at  $\theta^* = 90^\circ$ .

At  $\theta^* = 90^\circ$ , the data are well represented by

$$E \frac{d^3\sigma}{dp^3}(\theta^* = 90^\circ) \equiv F(\sqrt{s}, p_\perp) \quad (8)$$

with

$$F(\sqrt{s}, p_\perp) = \ln \left( \frac{\sqrt{s}}{\sqrt{s_{\min}}} \right) G(q, p_\perp)$$

$$q = s^{1/4}$$

and the COM pion production threshold energy

$$\sqrt{s_{\min}} = 2m_p + m_\pi$$

The function

$$G(q, p_\perp) \equiv \frac{E \frac{d^3\sigma}{dp^3}(\theta^* = 90^\circ)}{\ln \left( \frac{\sqrt{s}}{\sqrt{s_{\min}}} \right)}$$

was parameterized as

$$G(q, p_\perp) = \exp \left( k_1 + k_2 p_\perp + k_3 q^{-1} + k_4 p_\perp^2 + k_5 q^{-2} + k_6 p_\perp q^{-1} + k_7 p_\perp^3 + k_8 q^{-3} \right. \\ \left. + k_9 p_\perp q^{-2} + k_{10} p_\perp^2 q^{-1} + k_{11} p_\perp^{-3} \right) \quad (9)$$

with  $k_1 = 3.24$ ,  $k_2 = -6.046$ ,  $k_3 = 4.35$ ,  $k_4 = 0.883$ ,  $k_5 = -4.08$ ,  $k_6 = -3.05$ ,  $k_7 = -0.0347$ ,  $k_8 = 3.046$ ,  $k_9 = 4.098$ ,  $k_{10} = -1.152$ , and  $k_{11} = -0.0005$ . The parameters  $k_1$  to  $k_{10}$  were obtained with the numerical curve-fitting software, Table Curve 3D (ref. 24), and the eleventh term was added to modify the low  $p_\perp$  behavior of the parameterization.

With  $F(\sqrt{s}, p_\perp)$  determined, the function  $D(\sqrt{s}, p_\perp, \theta^*)$  is the only remaining unknown. Solving for  $D$  yields

$$D(\sqrt{s}, p_\perp, \theta^*) = \frac{\ln \left( E \frac{d^3\sigma}{dp^3} \right) - \ln [F(\sqrt{s}, p_\perp)]}{\ln(\sin \theta^*)} \quad (10)$$

Equations (8) and (9) were then used in equation (10) to calculate values of  $D(\sqrt{s}, p_{\perp}, \theta^*)$ . If the function  $D$  is independent of angle, then equation (10) could be determined for any fixed angle,  $\theta^* \neq 90^\circ$ . Data were compared for a range of angular values, and these data revealed that the function  $D$  is not independent of angle. The angular dependence turned out to be of the form  $(\sin \theta^*)^{-0.45}$ , and

$$D(\sqrt{s}, p_{\perp}, \theta^*) = (\sin \theta^*)^{-0.45} \left[ c_1 p_{\perp}^{c_2} (\sqrt{s})^{c_3} + c_4 \frac{p_{\perp}}{\sqrt{s}} + \frac{c_5}{\sqrt{s}} + \frac{1.0}{s} \right] \quad (11)$$

with  $c_1 = 205.7$ ,  $c_2 = 3.308$ ,  $c_3 = -2.875$ ,  $c_4 = 10.43$ , and  $c_5 = 0.8$ . The final form of our resultant parameterization for the neutral pion invariant cross section in proton-proton collisions is equation (7) with  $D(p_{\perp}, \sqrt{s}, \theta^*)$  given in equation (11),  $F(p_{\perp}, \sqrt{s})$  given in equation (8), and  $G(q, p_{\perp})$  given in equation (9). This form is accurate over a much greater range of transverse momentum values than those covered by previous representations. (See figs. 1 to 96 for comparisons.) For the low transverse momentum region where the cross section is the greatest, the fit is quite similar to that of Stephens and Badhwar (ref. 19). Also, figure 5 shows that both formulas (eqs. (7) and (6)) integrate to approximately the same total cross section, which is in agreement with the data from Whitmore (ref. 23). A more complete comparison of the integrated total cross section to data is given by Stephens and Badhwar (ref. 19).

## 2.2. Charged Pions

The available data for charged pions, consisting mostly of measurements made at  $\theta^* = 90^\circ$ , are less extensive than  $\pi^0$  data. Therefore a higher degree of uncertainty exists in LIDCS's for charged pions. Integration of an LIDCS to get a total cross section and comparison of the results with total cross section data allow a check of the global fit of a parameterization. This check was made for charged as well as neutral pions, but because of a lack of data, it is more important for charged pions. Parameterizations that do not integrate to the correct total cross section can be ruled out, even if the LIDCS data are well represented because the global behavior of the parameterization cannot be accurate. However, producing a correct total cross section upon integration does not necessarily imply that the global behavior of the parameterization is correct. If more measurements were made, a tighter constraint could be placed on possible LIDCS parameterizations. If the spectral distribution is measured at three different values of pion energy for two different proton collision energies, the general behavior of the spectral distribution could be checked. The angular dependence of LIDCS parameterization could then be tested by integrating over the angle and comparing the results with the spectral distribution data. For the purposes of space radiation shielding, measurements at proton lab kinetic energies of 3 and 6 GeV and pion lab kinetic energies of 0.01, 0.1, and 1 GeV would be useful because this is the region with both a large cross section and large galactic cosmic ray fluxes. These measurements would need to be made only for one pion, preferably  $\pi^0$ , because the general behavior of all the pion production cross sections is approximately the same. With these facts in mind, a comparison of LIDCS parameterizations with data from references 15 and 25 to 28 for charged pion production follows.

A parameterization for  $\pi^-$  of the form

$$E \frac{d^3\sigma}{dp^3} = A \exp(-B p_{\perp}^2) \quad (12)$$

has been given by Albrow et al. (ref. 28), where  $A$  and  $B$  are tabulated functions of  $x_R^* \equiv \frac{p^*}{p_{\max}^*}$ , and  $A$  and  $B$  are given only for  $x = 0.18, 0.21, \text{ and } 0.25$ , which limits the usefulness of this parameterization.

Alper et al. (ref. 25) have fitted the data for both  $\pi^+$  and  $\pi^-$  production to the following form:

$$E \frac{d^3\sigma}{dp^3} = A \exp(-Bp_{\perp} + Cp_{\perp}^2) \exp(-Dy^2) \quad (13)$$

where  $y$  is the longitudinal rapidity, and  $A$ ,  $B$ ,  $C$ , and  $D$  are tabulated functions of  $s$  that are also dependent on the type of produced particle ( $\pi^+$  or  $\pi^-$ ). (Note that at  $\theta^* = 90^\circ$ ,  $y$  equals 0.) The fit to the data is excellent for low transverse momentum, as can be seen in figures 97 to 102, but the figures show that this form has an increasing cross section for high  $p_{\perp}$ , which contradicts the trend in the data. Also, there are different sets of constants for each different energy, which makes a generalization to arbitrary energies difficult.

Parameterizations done by Carey et al. (ref. 29) and Ellis and Stroynowski (ref. 21) have a similar form, although Carey's was applied only to  $\pi^-$ . Both underestimate LIDCS's for low  $p_{\perp}$ , where the cross section is the largest. (See figs. 97 to 102.) The following equation is Carey's parameterization:

$$E \frac{d^3\sigma}{dp^3}(\pi^-) = N(p_{\perp}^2 + 0.86)^{-4.5} (1 - x_R)^4 \quad (14)$$

where  $N = 13$  is the overall normalization constant and  $x_R \equiv \frac{p^*}{p_{\max}^*} \approx \frac{2p^*}{\sqrt{s}}$ . The following equation is Ellis's parameterization, which was applied to both  $\pi^+$  and  $\pi^-$  production at  $\theta^* = 90^\circ$ :

$$E \frac{d^3\sigma}{dp^3} = A(p_{\perp}^2 + M^2)^{-N/2} (1 - x_{\perp})^F \quad (15)$$

where  $M$ ,  $N$ , and  $F$  are given constants,  $A$  is an unspecified overall normalization for which we used  $A = 13$ , and  $x_{\perp} \equiv \frac{p_{\perp}}{p_{\max}^*} \approx \frac{2p_{\perp}}{\sqrt{s}}$ .

The most successful previously developed LIDCS parameterization available for charged pion production was found to be the one developed by Badhwar, Stephens, and Golden (ref. 30), which is

$$E \frac{d^3\sigma}{dp^3} = \frac{A(1 - \tilde{x})^q}{(1 + 4m_p^2/s)^r} e^{-Bp_{\perp}/(1+4m_p^2/s)} \quad (16)$$

where  $q$  is a function of  $p_{\perp}$  and  $s$ , such that

$$q = \frac{C_1 + C_2 p_{\perp} + C_3 p_{\perp}^2}{(1 + 4m_p^2/s)^{1/2}}$$

and

$$\tilde{x} \approx \left[ x_{\parallel}^{*2} + \frac{4}{s} (p_{\perp}^2 + m_{\pi}^2) \right]^{1/2}$$

Here  $x_{\parallel}^* = \frac{p_{\parallel}^*}{p_{\max}^*} \approx 2 \frac{p_{\parallel}^*}{\sqrt{s}}$ . For  $\pi^+$ ,  $A = 153$ ,  $B = 5.55$ ,  $C_1 = 5.3667$ ,  $C_2 = -3.5$ ,  $C_3 = 0.8334$ , and  $r = 1$ . For  $\pi^-$ ,  $A = 127$ ,  $B = 5.3$ ,  $C_1 = 7.0334$ ,  $C_2 = -4.5$ ,  $C_3 = 1.667$ , and  $r = 3$ . This form is accurate for low transverse momentum (figs. 97 to 102), which is the most important region for radiation shielding because of the large cross section. It is also in closed form so that extra numerical complexities do not have to be considered. A comparison with a few data points, shown in figures 103 and 104, demonstrates that it integrates to the correct total cross section. A more detailed comparison of the integrated cross section with experimental data is given by Badhwar, Stephens, and Golden (ref. 30). Because of its relative accuracy and simplicity, this

parameterization was integrated to get total cross sections and spectral distributions for charged pions.

Mokhov and Striganov (ref. 31) have also developed the following formulas for both  $\pi^+$  and  $\pi^-$  production:

$$E \frac{d^3\sigma}{dp^3} = A \left(1 - \frac{p^*}{p_{\max}^*}\right)^B \exp\left(-\frac{p^*}{C\sqrt{s}}\right) V_1(p_{\perp}) V_2(p_{\perp}) \quad (17)$$

where

$$V_1 = (1 - D) \exp(-Ep_{\perp}^2) + D \exp(-Fp_{\perp}^2) \quad (p_{\perp} \leq 0.933 \text{ GeV})$$

$$V_1 = \frac{0.2625}{(p_{\perp}^2 + 0.87)^4} \quad (p_{\perp} > 0.933 \text{ GeV})$$

and

$$V_2 = 0.7363 \exp(0.875p_{\perp}) \quad (p_{\perp} \leq 0.35 \text{ GeV})$$

$$V_2 = 1 \quad (p_{\perp} > 0.35 \text{ GeV})$$

with  $A = 60.1$ ,  $B = 1.9$ , and  $C = 0.18$  for  $\pi^+$ ;  $A = 51.2$ ,  $B = 2.6$ , and  $C = 0.17$  for  $\pi^-$ ; and  $D = 0.3$ ,  $E = 12$ , and  $F = 2.7$  for both  $\pi^+$  and  $\pi^-$ . Figures 97 to 102 show that the formula of Badhwar has a better fit to the data in the low  $p_{\perp}$  region where the cross section is the largest.

### 3. Spectral Distributions and Total Cross Sections

#### 3.1. Method of Generating Other Cross Sections From LIDCS's

Although LIDCS's contain all the necessary information for a particular process, sometimes other cross sections are needed. For example, one-dimensional radiation transport requires probability density distributions that are integrated over solid angle. These quantities are calculated in terms of spectral distributions and total cross sections rather than LIDCS's, but with accurate parameterizations of LIDCS's, formulas for both spectral distributions and total cross sections can be developed. LIDCS's for inclusive pion production in proton-proton collisions contain dependence on the energy of the colliding protons  $\sqrt{s}$ , on the energy of the produced pion  $T_{\pi}$ , and on the scattering angle of the pion  $\theta$ . Total cross sections  $\sigma$ , which depend only on  $\sqrt{s}$ , and spectral distributions  $\frac{d\sigma}{dE}$ , which depend on  $\sqrt{s}$  and  $T_{\pi}$ , can be extracted from an LIDCS by integration. If azimuthal symmetry is assumed, these cross sections take the following forms:

$$\frac{d\sigma}{dE} = 2\pi p \int_0^{\theta_{\max}} d\theta E \frac{d^3\sigma}{dp^3} \sin \theta \quad (18)$$

$$\sigma = 2\pi \int_0^{\theta_{\max}} d\theta \int_{p_{\min}}^{p_{\max}} dp E \frac{d^3\sigma}{dp^3} \frac{p^2 \sin \theta}{\sqrt{p^2 + m_{\pi}^2}} \quad (19)$$

where  $\theta_{\max}$ ,  $p_{\max}$ , and  $p_{\min}$  are the extrema of the scattering angle and momentum of the pion, and  $m_{\pi}$  is the rest mass of the pion.

In the COM frame, these extrema can easily be determined. (See appendix A for a detailed analysis.) Using conservation of momentum and energy, one can easily show

$$p^2 = \frac{(s + m_{\pi}^2 - s_x)^2}{4s} - m_{\pi}^2 \quad (20)$$

where  $s_x$  is the square of the invariant mass of the sum of all particles excluding the pion, and  $p$  is the magnitude of the three momentum of the pion. The independence of  $p$  on  $\theta$  implies that  $\theta$  can take on all possible values (i.e.,  $\theta_{\max} = \pi$ ), and the symmetry of the COM frame implies that  $p_{\min} = 0$ . For a given value of  $s$ , it is obvious that momentum is a maximum when  $s_x$  is a minimum. As shown in appendix B, an invariant mass is a minimum when it is equal to the square of the sum of the rest masses of the particles in question. Momentum is, therefore, a maximum when  $s_x$  is the square of the sum of the least massive combination of particles that can be produced and still satisfy all relevant conservation laws. For the reaction  $p + p \rightarrow \pi + x$ , we have  $s_x \approx 4m_p^2$ , where subscript  $p$  represents a proton. Exact formulas are listed in appendix B along with a more detailed analysis.

If a Lorentz transformation is applied to the maximum COM momentum, the integration limits can be determined in other frames. Byckling and Kajantie (ref. 32) have shown that by transforming to the lab frame, the following formula can be obtained:

$$p_{\pi}^{\pm} = \left[ p_a E_{\max}^* \sqrt{s} \cos \theta \pm (E_a + m_p) \sqrt{sp_{\max}^{*2} - m_{\pi}^2 p_a^2 \sin^2 \theta} \right] \left[ s + p_a^2 \sin^2(\theta) \right]^{-1} \quad (21)$$

where quantities with an asterisk are COM variables, quantities without an asterisk are either lab or invariant variables,  $m_p$  is the rest mass of a proton,  $p_a$  is the magnitude of the momentum of the projectile proton, and  $p^+ = p_{\max}$  is the maximum pion momentum. The greater of the two quantities  $p^- = p_{\min}$  and 0 is the minimum pion momentum, and the maximum scattering angle can be determined by the requirement that  $p^{\pm}$  be real. This requirement implies that the quantity under the square root in equation (21) must be greater than or equal to 0. Solving for  $\theta_{\max}$  then gives the formula

$$\theta_{\max} = \sin^{-1} \left( \frac{\sqrt{s} p_{\max}^*}{p_a m_p} \right) \quad (22)$$

With the limits of integration determined, an LIDCS can be turned into a total cross section or a spectral distribution by numerical integration. This procedure will, however, give discrete “data” points not closed-form expressions. Parameterizations of these numerical data are needed, if relatively simple formulas for these cross sections are desired. This process was completed for all three pion species, and the corresponding formulas are given in the next section.

### 3.2. Parameterizations

The surface parameterizations for the spectral distribution as a function of incident proton kinetic energy in the lab frame  $T_{\text{lab}}$  and the lab kinetic energy of the produced pion  $T_{\pi}$  have been completed by numerically integrating LIDCS charged pion parameterizations of Badhwar, Stephens, and Golden (eq. (16) and ref. 30) and the neutral pion cross section from Stephens and Badhwar (eq. (6) and ref. 19). The numerical integration routines were checked by computing total cross sections in both the lab and COM frames and comparing the results. Because total cross section is a Lorentz invariant, the results should be the same in both frames. To accurately fit the integration points for low energies, considering two regions of the surface and determining representations for them individually have been necessary. For each of the three pions, the two regions consist of laboratory kinetic energies  $T_{\text{lab}}$  from 0.3 to 2 GeV and from 2 to 50 GeV.

The neutral pion spectral distribution for the range 0.3 to 2 GeV is given by the following equations:

$$\left. \begin{aligned} F_2 &= A_1 T_\pi^{A_2} + A_3 T_{\text{lab}}^{A_4} \\ F_1 &= \exp\left( A_5 + \frac{A_6}{\sqrt{T_{\text{lab}}}} + A_7 T_{\text{lab}}^{A_8} + A_9 T_\pi^{A_{10}} + A_{11} T_\pi^{A_{12}} \right) \\ \left( \frac{d\sigma}{dE} \right)_{\text{lab}} &= \left[ A_{13} \frac{F_1}{F_2} + A_{14} \exp\left( A_{16} \sqrt{T_\pi} + A_{17} T_\pi^{A_{18}} T_{\text{lab}}^{A_{19}} \right) \right] T_\pi^{A_{15}} \end{aligned} \right\} \quad (23)$$

with constants  $A_i$  given in table 1. The neutral pion spectral distribution for the range 2 to 50 GeV is given by the following equations:

$$\left. \begin{aligned} F_2 &= B_1 T_\pi^{B_2} + B_3 T_{\text{lab}}^{B_4} \\ F_1 &= \exp\left( B_5 + \frac{B_6}{\sqrt{T_{\text{lab}}}} + B_7 T_{\text{lab}}^{B_8} + B_9 T_\pi^{B_{10}} + B_{11} T_\pi^{B_{12}} \right) \\ \left( \frac{d\sigma}{dE} \right)_{\text{lab}} &= B_{13} T_\pi^{B_{14}} \frac{F_1}{F_2} + B_{15} T_\pi^{B_{16}} \exp\left( B_{17} \sqrt{T_\pi} \right) \end{aligned} \right\} \quad (24)$$

with constants  $B_i$  given in table 2.

Table 1. Constants  $A_i$  for Equations (23)

Constant	Value
$A_1$	$6.78 \times 10^{-10}$
$A_2$	-2.86
$A_3$	$1.82 \times 10^{-8}$
$A_4$	-1.92
$A_5$	22.3
$A_6$	0.226
$A_7$	-0.33
$A_8$	-1.75
$A_9$	-32.1
$A_{10}$	0.0938
$A_{11}$	-23.7
$A_{12}$	0.0313
$A_{13}$	$2.5 \times 10^6$
$A_{14}$	1.38
$A_{15}$	0.25
$A_{16}$	-39.4
$A_{17}$	2.88
$A_{18}$	0.025
$A_{19}$	0.75

Table 2. Constants  $B_i$  for Equations (24)

Constant	Value
$B_1$	$1.3 \times 10^{-10}$
$B_2$	-2.86
$B_3$	$4.27 \times 10^{-9}$
$B_4$	-2.4
$B_5$	22.3
$B_6$	-1.87
$B_7$	1.28
$B_8$	-1.25
$B_9$	-33.2
$B_{10}$	0.0938
$B_{11}$	-23.6
$B_{12}$	0.0313
$B_{13}$	$2.5 \times 10^6$
$B_{14}$	0.25
$B_{15}$	60322
$B_{16}$	1.07
$B_{17}$	-67.5

The positively charged pion spectral distribution for the range 0.3 to 2 GeV is given by the following equations:

$$\left. \begin{aligned} F_2 &= C_1 T_\pi^{C_2} + C_3 T_{\text{lab}}^{C_4} \\ F_1 &= \exp \left[ C_5 + \frac{C_6}{\sqrt{T_{\text{lab}}}} + C_7 T_{\text{lab}}^{C_8} + C_9 T_\pi^{C_{10}} + C_{11} T_\pi^{C_{12}} T_{\text{lab}}^{C_{13}} + C_{14} \ln(T_{\text{lab}}) \right] \\ \left( \frac{d\sigma}{dE} \right)_{\text{lab}} &= C_{15} T_\pi^{C_{16}} \frac{F_1}{F_2} + C_{17} T_\pi^{C_{18}} \exp \left( C_{19} \sqrt{T_\pi} + C_{20} \sqrt{T_{\text{lab}}} \right) \end{aligned} \right\} \quad (25)$$

with constants  $C_i$  given in table 3.

The positively charged pion spectral distribution for the range 2 to 50 GeV is given by the following equations:

$$\left. \begin{aligned} F_2 &= D_1 T_\pi^{D_2} + D_3 T_{\text{lab}}^{D_4} \\ F_1 &= \exp \left( D_5 + \frac{D_6}{\sqrt{T_{\text{lab}}}} + D_7 T_\pi^{D_8} + D_9 T_\pi^{D_{10}} \right) \\ \left( \frac{d\sigma}{dE} \right)_{\text{lab}} &= D_{11} T_\pi^{D_{12}} \frac{F_1}{F_2} + D_{13} T_\pi^{D_{14}} \exp \left( D_{15} \sqrt{T_\pi} + D_{16} T_{\text{lab}}^{D_{17}} \right) \end{aligned} \right\} \quad (26)$$

with constants  $D_i$  given in table 4.

Table 3. Constants  $C_i$  for Equations (25)

Constant	Value
$C_1$	$2.2 \times 10^{-8}$
$C_2$	-2.7
$C_3$	$4.22 \times 10^{-7}$
$C_4$	-1.88
$C_5$	22.3
$C_6$	1.98
$C_7$	-0.28
$C_8$	-1.75
$C_9$	-29.4
$C_{10}$	0.0938
$C_{11}$	-24.4
$C_{12}$	0.0312
$C_{13}$	0.0389
$C_{14}$	1.78
$C_{15}$	$2.5 \times 10^6$
$C_{16}$	0.25
$C_{17}$	976
$C_{18}$	2.3
$C_{19}$	-46
$C_{20}$	-0.989

Table 4. Constants  $D_i$  for Equations (26)

Constant	Value
$D_1$	$4.5 \times 10^{-11}$
$D_2$	-2.98
$D_3$	$1.18 \times 10^{-9}$
$D_4$	-2.55
$D_5$	22.3
$D_6$	-0.765
$D_7$	-35.3
$D_8$	0.0938
$D_9$	-22.5
$D_{10}$	0.0313
$D_{11}$	$2.5 \times 10^6$
$D_{12}$	0.25
$D_{13}$	60322
$D_{14}$	1.18
$D_{15}$	-72.2
$D_{16}$	0.941
$D_{17}$	0.1

The negatively charged pion spectral distribution for the range 0.3 to 2 GeV is given by the following equations:

$$\left. \begin{aligned} F_2 &= G_1 T_\pi^{G_2} + G_3 T_{\text{lab}}^{G_4} \\ F_1 &= \exp\left(G_5 + \frac{G_6}{\sqrt{T_{\text{lab}}}} + G_7 T_\pi^{G_8} + G_9 T_\pi^{G_{10}}\right) \\ \left(\frac{d\sigma}{dE}\right)_{\text{lab}} &= T_\pi^{G_{11}} \left[ G_{12} \frac{F_1}{F_2} + G_{13} \exp(G_{14} \sqrt{T_\pi}) \right] \end{aligned} \right\} \quad (27)$$

with constants  $G_i$  given in table 5.

The negatively charged pion spectral distribution for the range 2 to 50 GeV is given by the following equations:

$$\left. \begin{aligned} F_2 &= H_1 T_\pi^{H_2} + H_3 T_{\text{lab}}^{H_4} \\ F_1 &= \exp\left(H_5 + \frac{H_6}{\sqrt{T_{\text{lab}}}} + H_7 T_\pi^{H_8} + H_9 T_\pi^{H_{10}}\right) \\ \left(\frac{d\sigma}{dE}\right)_{\text{lab}} &= H_{11} T_\pi^{H_{12}} \frac{F_1}{F_2} + H_{13} T_\pi^{H_{14}} \exp\left(H_{15} \sqrt{T_\pi} + H_{16} T_{\text{lab}}^{H_{17}}\right) \end{aligned} \right\} \quad (28)$$

with constants  $H_i$  given in table 6.

Table 5. Constants  $G_i$  for Equations (27)

Constant	Value
$G_1$	$1.06 \times 10^{-9}$
$G_2$	-2.8
$G_3$	$3.7 \times 10^{-8}$
$G_4$	-1.89
$G_5$	22.3
$G_6$	-1.5
$G_7$	-30.5
$G_8$	0.0938
$G_9$	-24.6
$G_{10}$	0.0313
$G_{11}$	0.25
$G_{12}$	$2.5 \times 10^6$
$G_{13}$	7.96
$G_{14}$	-49.5

Table 6. Constants  $H_i$  for Equations (28)

Constant	Value
$H_1$	$2.39 \times 10^{-10}$
$H_2$	-2.8
$H_3$	$1.14 \times 10^{-8}$
$H_4$	-2.3
$H_5$	22.3
$H_6$	-2.23
$H_7$	-31.3
$H_8$	0.0938
$H_9$	-24.9
$H_{10}$	0.0313
$H_{11}$	$2.5 \times 10^6$
$H_{12}$	0.025
$H_{13}$	60322
$H_{14}$	1.1
$H_{15}$	-65.9
$H_{16}$	-9.39
$H_{17}$	-1.25

Total inclusive cross sections are given by the following equations:

$$\sigma_{\pi^0} = \left( 0.007 + 0.1 \frac{\ln(T_{\text{lab}})}{T_{\text{lab}}} + \frac{0.3}{T_{\text{lab}}^2} \right)^{-1} \quad (29)$$

$$\sigma_{\pi^+} = \left( 0.00717 + 0.0652 \frac{\ln(T_{\text{lab}})}{T_{\text{lab}}} + \frac{0.162}{T_{\text{lab}}^2} \right)^{-1} \quad (30)$$

$$\sigma_{\pi^-} = \left( 0.00456 + \frac{0.0846}{T_{\text{lab}}^{0.5}} + \frac{0.577}{T_{\text{lab}}^{1.5}} \right)^{-1} \quad (31)$$

For neutral pions, spectral distributions and total cross sections that were based on the present parameterization given in equation (7) were also developed. The formula for the spectral distribution was not divided into two regions and is much simpler than the previous formulas:

$$\left( \frac{d\sigma}{dE} \right)_{\text{lab}} = \exp \left( K_1 + \frac{K_2}{T_{\text{lab}}^{0.4}} + \frac{K_3}{T_{\pi}^{0.2}} + \frac{K_4}{T_{\pi}^{0.4}} \right) \quad (32)$$

where  $K_1 = -5.8$ ,  $K_2 = -1.82$ ,  $K_3 = 13.5$ , and  $K_4 = -4.5$ .

Because equation (7) and Stephens' LIDCS parameterization integrate to nearly the same total cross section (fig. 5), separate total cross section parameterizations are not necessary (i.e., use eq. (29)).

### 3.3. Discussion of Spectral Distributions and Total Cross Sections

As discussed previously, figures 1 to 4 and 6 to 9 show the LIDCS parameterizations for  $\pi^0$  production of Carey et al. (eq. (5) and ref. 14), Stephens and Badhwar (eq. (6) and ref. 19), and of equation (7) plotted with data from references 12 to 17, 20, and 23. The figures are graphs of cross section  $E \frac{d^3\sigma}{dp^3}$  plotted against transverse momentum  $p_{\perp}$  for various values of

COM energy  $E_{cm}$  and COM scattering angle  $\theta^*$ , which can be transformed into lab variables as shown in appendix B. Figures 1 to 3 and 7 show that the parameterization of Carey et al. is not an adequate representation of the data. Figures 6 and 7 show that the parameterization of Stephens and Badhwar fails for high transverse momentum by severely underpredicting the cross section.

Figure 5 shows numerically integrated LIDCS parameterizations of Stephens and Badhwar (eq. (6) and ref. 19), of Carey et al. (eq. (5) and ref. 14), and of equation (7) (referred to as "Kruger") for  $\pi^0$  production plotted with a parameterization of the integrated formulas of Stephens and Badhwar, referred to as "Stephens-total-param" (eq. (29)). Three data points from Whitmore (ref. 23) show that Carey's parameterization does not integrate to the correct values and that the rest are quite accurate. (See ref. 19 for more detail.)

Figures 10 to 96 show  $\pi^0$  LIDCS parameterizations of Carey et al. (eq. (5) and ref. 14), of Stephens and Badhwar (eq. (6) and ref. 19), and of equation (7) plotted with data from references 12 to 17, 19, and 20 over a wide range of angles and energies. These graphs show that equation (7) has the best global fit to all data available.

As discussed previously, figures 97 to 102 show  $\pi^+$  and  $\pi^-$  LIDCS parameterizations of Alper et al. (eq. (13) and ref. 25), of Badhwar, Stephens, and Golden (eq. (16) and ref. 30), of Ellis and Stroynowski (eq. (15) and ref. 21), of Carey et al. (eq. (14) and ref. 29), and of Mokhov

and Striganov (eq. (17) and ref. 31) and LIDCS data from references 18 and 15 plotted against transverse momentum for different values of COM energy  $E_{cm}$  with all at  $\theta^* = 90^\circ$ . These graphs show that the parameterizations of Badhwar and Alper best fit the data, but Alper's parameterization rapidly increases for high transverse momentum which contradicts the trend of the data.

Figure 103 shows numerically integrated LIDCS parameterizations of Badhwar, Stephens, and Golden (eq. (16) and ref. 30) for  $\pi^+$  plotted with parameterizations of the integrated formulas of Badhwar referred to as "present work" (eq. (30)). Figure 104 shows numerically integrated LIDCS parameterizations of Badhwar, Stephens, and Golden (eq. (16) and ref. 30), of Carey et al. (eq. (14) and ref. 29) for  $\pi^-$  plotted with parameterizations of the integrated formulas of Badhwar referred to as "present work" (eq. (31)). Three data points from reference 23 show that Carey's parameterization does not integrate to the correct values and that Badhwar's formula is fairly accurate. The figures also show that the parameterization fits the numerically integrated formulas very well.

Figure 105 shows  $\pi^0$  spectral distribution parameterizations given by equations (23) and (24) plotted with LIDCS parameterization of Stephens numerically integrated at several lab kinetic energies. Figure 106 is the same as figure 105 except that the spectral distribution of equation (32) is plotted with the numerical integration of equation (7).

Figures 107 and 108 show  $\pi^-$  and  $\pi^+$  spectral distribution parameterizations plotted with LIDCS parameterization of Badhwar, Stephens, and Golden (eq. (16) and ref. 30) numerically integrated. Cross section  $\frac{d\sigma}{dE}$  is plotted against the kinetic energy of the produced pion  $T_\pi$  at several values of the lab kinetic energies of the colliding proton.

#### 4. Concluding Remarks

This paper presents parameterization of cross sections for inclusive pion production in proton-proton collisions. The cross sections of interest are Lorentz invariant differential cross sections (LIDCS's), laboratory (lab) frame spectral distributions, and total cross sections. For neutral pions the parameterization of Stephens and Badhwar (*Astrophys. & Space Sci.*, vol. 76, 1981, pp. 213-217) fit the data well for low values of transverse momentum  $p_\perp$  but overpredict the cross section by many orders of magnitude at high  $p_\perp$  values. Because of this inaccuracy, an equation was developed. The final form of our resultant parameterization for the neutral pion invariant cross section in proton-proton collisions is as accurate as that of Stephens and Badhwar at low  $p_\perp$  values but is much more accurate at high  $p_\perp$  values. For charged pions the formula of Badhwar, Stephens, and Golden (*Phys. Rev. D*, vol. 15, 1977, pp. 820-831) was found to best represent the data except at high  $p_\perp$  values and that of Ellis and Stroynowski (*Rev. Modern Phys.*, vol. 49, 1977, pp. 753-775) was quite accurate. The formula of Badhwar, Stephens, and Golden was used in the development of spectral distributions and total cross sections because it was the most accurate at low  $p_\perp$  where the cross section is the greatest.

The data for lab frame spectral distributions and total cross sections are scarce; therefore, parameterizations for these quantities were developed with LIDCS formulas. These formulas were numerically integrated, resulting in discrete numerical data points for the other cross sections, namely spectral distributions and total cross sections. The accuracy of the representations of lab frame spectral distributions and total cross sections is, therefore, limited to the accuracy of the original LIDCS's. The numerical data were then parameterized so that closed-form expressions could be obtained. As a check on the accuracy, the total cross section numerical data were compared with experimental data. They were found to agree quite well, but when the numerical data for the spectral distributions for the formulas for  $\pi^0$  production are compared, they are found to disagree. Because both original LIDCS formulas fit the data well at

low  $p_{\perp}$ , where the cross section is greatest, and both formulas integrate to the correct total cross section, the available data must not be sufficient to uniquely determine the global behavior of the LIDCS's. The data for charged pion production were much more limited than the data for neutral pion production; therefore, the same problem exists for charged pions.

To more accurately determine the cross sections for space radiation applications, measurements of the spectral distribution at lower energies (for example, proton lab kinetic energies of 3 and 8 GeV and pion lab kinetic energies of 0.01, 0.1, and 1 GeV) for one pion species would need to be taken. Only measurements for one pion species would be needed because they all have approximately the same general behavior. These measurements would put a much tighter constraint on the global properties of the LIDCS's, and the spectral distribution parameterizations could also be made more accurate.

## Appendix A

### Derivation of Maximum Momentum

Consider an inelastic two-particle collision. The maximum momentum that a produced particle can have in the COM frame can easily be determined by imposing conservation laws. The reaction considered is a two-particle A and B reaction resulting in a pion  $\pi$  and various other particles X (i.e.,  $A + B \rightarrow \pi + X$ ). Quantities pertaining to the initial particles are labeled with subscripts  $a$  and  $b$ . Quantities pertaining to the pion of interest are labeled with subscript  $\pi$ , and quantities pertaining to the system consisting of all other produced particles are labeled with subscript  $x$ . Units where the speed of light is equal to unity are used.

Conservation of energy implies that the initial energy equals the final energy:

$$E_a + E_b = E_\pi + E_x = \sqrt{s} \quad (\text{A1})$$

where  $\sqrt{s}$  is the invariant mass of the entire system. See appendix B for the relations between various kinematic variables.

In the COM frame, the total three momentum is zero. Therefore,

$$\vec{p}_a + \vec{p}_b = \vec{p}_\pi + \vec{p}_x = 0 \quad (\text{A2})$$

$$\vec{p}_\pi = -\vec{p}_x \quad (\text{A3})$$

$$|\vec{p}_\pi|^2 = |\vec{p}_x|^2 \quad (\text{A4})$$

$$E_\pi^2 - m_\pi^2 = E_x^2 - s_x \quad (\text{A5})$$

where  $s_x$  is the square of the invariant mass of the system consisting of all particles except the pion, and  $m_\pi$  is the rest mass of the pion. By rearranging terms, adding  $E_\pi^2$  to both sides, and a little further algebra, equation (37) becomes

$$E_x^2 + E_\pi^2 = 2E_\pi^2 + s_x - m_\pi^2 \quad (\text{A6})$$

$$E_x^2 + E_\pi^2 + 2E_\pi E_x = 2E_\pi^2 + s_x - m_\pi^2 + 2E_\pi E_x \quad (\text{A7})$$

$$s - s_x + m_\pi^2 = 2E_\pi(E_\pi + E_x) \quad (\text{A8})$$

Substituting equation (A8) into equation (A1) results in

$$2E_\pi\sqrt{s} = s - s_x + m_\pi^2 \quad (\text{A9})$$

$$E_\pi = \frac{s + m_\pi^2 - s_x}{2\sqrt{s}} \quad (\text{A10})$$

$$|\vec{p}_\pi|^2 = \frac{(s + m_\pi^2 - s_x)^2}{4s} - m_\pi^2 \quad (\text{A11})$$

Equation (A11) obviously implies that the pion momentum is a maximum for a given  $s$ , when  $s_x$  is a minimum:

$$|\vec{p}_{\pi\text{max}}|^2 = \frac{(s + m_\pi^2 - s_{x\text{min}})^2}{4s} - m_\pi^2 \quad (\text{A12})$$

To specify  $|\vec{p}_{\pi\max}|^2$  for a given inclusive reaction,  $s_{x\min}$  needs to be derived;  $s_x$  is the square of the invariant mass of an  $N$  particle system, which is defined as the square of the four momentum of that system, as follows:

$$s_x = \left( \sum_{i=1}^N p_i \right)^2 \quad (\text{A13})$$

$$s_x = \sum_{i,j=1}^N p_i \cdot p_j \quad (\text{A14})$$

where  $p_i \cdot p_j$  is a Lorentz scalar and can be calculated in any frame. For simplicity, the calculation is done in the rest frame of the  $i$ th particle, so that  $E_i = m_i$ , the speed  $v_i = 0$ ,  $\vec{p}_i = 0$ , and  $\gamma_i = \sqrt{\frac{1}{1-v_i^2}} = 1$ . For massive particles,

$$p_i \cdot p_j = E_i E_j - \vec{p}_i \cdot \vec{p}_j \quad (\text{A15})$$

$$p_i \cdot p_j = \gamma_i m_i \gamma_j m_j \quad (\text{A16})$$

$$p_i \cdot p_j = \gamma_j m_i m_j \quad (\text{A17})$$

where  $\gamma_j = \sqrt{\frac{1}{1-v_j^2}} \geq 1$ , and  $v_j$  is the speed of the  $j$ th particle. Equation (A17) further implies

$$p_i \cdot p_j \geq m_i m_j \quad (\text{A18})$$

If one particle is massless,  $p_i \cdot p_j$  can be calculated in the rest frame of the massive particle, which can be assumed to be the  $i$ th particle, without a loss of generality:

$$p_i \cdot p_j = E_i E_j - \vec{p}_i \cdot \vec{p}_j \quad (\text{A19})$$

$$p_i \cdot p_j = m_i E_j \quad (i \neq j) \quad (\text{A20})$$

which is a minimum and equals zero in the limit as  $E_j \rightarrow 0$ . If both particles are massless,

$$p_i \cdot p_j = E_i E_j - \vec{p}_i \cdot \vec{p}_j \quad (\text{A21})$$

$$p_i \cdot p_j = E_i E_j - E_i E_j \quad (\text{A22})$$

$$p_i \cdot p_j = 0 \quad (\text{A23})$$

Therefore, for any combination of massive and massless particles,

$$p_i \cdot p_j \geq m_i m_j \quad (\text{A24})$$

Substituting equation (A24) into equation (A14) results in

$$s_x \geq \sum_{i,j=1}^N m_i m_j \quad (\text{A25})$$

Therefore,

$$s_{x_{\min}} = \sum_{i,j=1}^N m_i m_j \quad (\text{A26})$$

$$s_{x_{\min}} = \left( \sum_{i=1}^N m_i \right)^2 \quad (\text{A27})$$

when the sum is over the least massive combination of particles that can be produced while satisfying all relevant conservation laws.

For pions produced in proton-proton collisions, the reactions where  $s_x$  can be a minimum are as follows:

For  $\pi^+$ ,

$$p + p \rightarrow \pi^+ + p + p + e^- + \bar{\nu}_e \quad (\text{A28})$$

$$\Rightarrow s_{x_{\min}} = (2m_p + m_e + m_{\bar{\nu}_e})^2 \approx 4m_p^2 \quad (\text{A29})$$

For  $\pi^0$ ,

$$p + p \rightarrow \pi^0 + p + p \quad (\text{A30})$$

$$\Rightarrow s_{x_{\min}} = 4m_p^2 \quad (\text{A31})$$

For  $\pi^-$ ,

$$p + p \rightarrow \pi^- + p + p + e^+ + \nu_e \quad (\text{A32})$$

$$\Rightarrow s_{x_{\min}} = (2m_p + m_e + m_{\nu_e})^2 \approx 4m_p^2 \quad (\text{A33})$$

where  $p$  represents a proton,  $e$  represents an electron,  $\nu_e$  represents an electron-neutrino,  $\bar{\nu}_e$  represents an electron-antineutrino, and  $e^+$  represents a positron.

## Appendix B

### Kinematic Relations

The two reference frames of interest in this paper are the COM frame and the lab frame. In a two-particle collision, the lab frame is defined so that one of the colliding particles is at rest, and in the COM frame, the net three momentum is zero. Using the fact that the square of the four momentum of a system  $s$  is Lorentz invariant, a relation between COM energies and lab energies can be derived. In the COM frame,

$$\begin{aligned} s &= (E_a^* + E_b^*)^2 - (\vec{p}_a^* + \vec{p}_b^*)^2 \\ &= (E_a^* + E_b^*)^2 \end{aligned} \quad (\text{B1})$$

where  $*$  refers to a COM quantity, and variables without  $*$  are either in the lab frame or they are invariant under the transformation from the lab frame to the COM frame,  $E$  is a total energy,  $\vec{p}$  is a three momentum, and subscripts  $a$  and  $b$  distinguish the two colliding particles. Equation (B1), therefore, implies that  $\sqrt{s}$  is equal to the COM total energy.

In the lab frame where particle  $b$  is at rest, and  $T_{\text{lab}}$  is the kinetic energy of particle  $a$ ,

$$s = (E_a + E_b)^2 - (\vec{p}_a + \vec{p}_b)^2 \quad (\text{B2})$$

$$s = (E_a + m_b)^2 - |\vec{p}_a|^2 \quad (\text{B3})$$

$$s = m_a^2 + m_b^2 + 2E_a m_b \quad (\text{B4})$$

$$s = m_a^2 + m_b^2 + 2(T_{\text{lab}} + m_a)m_b \quad (\text{B5})$$

$$s = (m_a + m_b)^2 + 2T_{\text{lab}}m_b \quad (\text{B6})$$

where  $m_a$  and  $m_b$  are the rest masses of particles  $a$  and  $b$ , respectively,  $T_{\text{lab}} = E_a - m_a$  is the lab frame kinetic energy of the incoming particle, and  $E = \sqrt{|\vec{p}|^2 + m^2}$ . Taken together, equations (B1) and (B6) imply that

$$(E_a^* + E_b^*)^2 = (m_a + m_b)^2 + 2T_{\text{lab}}m_b \quad (\text{B7})$$

The relations between the lab scattering angle  $\theta$ , the magnitude of the lab three momentum  $|\vec{p}|$ , and the corresponding COM quantities can be derived by using the following equations (ref. 32):

$$|\vec{p}|^* \sin \theta^* = |\vec{p}| \sin \theta \quad (\text{B8})$$

$$|\vec{p}|^* \cos \theta^* = \gamma |\vec{p}| \cos \theta - \gamma v E \quad (\text{B9})$$

$$E^* = -\gamma v |\vec{p}| \cos \theta + \gamma E \quad (\text{B10})$$

where  $v = \sqrt{1 - \gamma^{-2}}$  is the relative speed of the lab frame and the COM frame, and for the case of two colliding protons,  $\gamma = \frac{T_{\text{lab}} + 2m_p}{\sqrt{s}}$  (ref. 32). The magnitude of the COM three momentum and the COM scattering angle can now be easily derived in the following manner:

$$|\vec{p}^*|^2 = |\vec{p}|^2(\cos^2 \theta^* + \sin^2 \theta^*) \quad (\text{B11})$$

$$|\vec{p}|^2 = \gamma^2(|\vec{p}| \cos \theta - vE)^2 + |\vec{p}|^2 \sin^2 \theta \quad (\text{B12})$$

and

$$\tan \theta^* = \frac{|\vec{p}|^* \sin \theta^*}{|\vec{p}|^* \cos \theta^*} \quad (\text{B13})$$

$$\tan \theta = \frac{|\vec{p}| \sin \theta}{\gamma |\vec{p}| \cos \theta - \gamma v E} \quad (\text{B14})$$

Therefore,

$$\theta^* = \tan^{-1} \left( \frac{|\vec{p}| \sin \theta}{\gamma |\vec{p}| \cos \theta - \gamma v E} \right) \quad (\text{B15})$$

## Appendix C

### Synopsis of Data Transformations

The data used in the comparison of different parameterizations were given in terms of several different kinematic variables. Some data were transformed so that all data would be expressed in terms of the same variables. A synopsis of the transformations that were performed for the data plotted in the figures is as follows.

The data from Büsser et al. (refs. 12 and 15) and Owen et al. (ref. 17) were given for different values of  $\sqrt{s}$ ,  $p_{\perp}$ , and  $\theta^*$ . No transformations were performed. The data from Carey et al. (ref. 14) were given for different values of  $P_p$ ,  $p_{\perp}$ , and  $\theta$ ;  $P_p$  was transformed to  $\sqrt{s}$  by using equation (B4) and the relation  $E = \sqrt{|\vec{p}|^2 + m^2}$ . Then  $\theta$  was transformed to  $\theta^*$  with equation (B15). Eggert et al. (ref. 16) used  $\sqrt{s}$ ,  $p_{\perp}$ , and  $\theta$ . Equation (B15) was used to transform  $\theta$  to  $\theta^*$ . Alper et al. (ref. 25) used  $\sqrt{s}$ ,  $p_{\perp}$ , and the longitudinal rapidity  $y$ . Only data with  $y = 0$  were used, and when  $y = 0$  then  $\theta^*$  equals  $90^\circ$ . The data from Whitmore (ref. 23) were not transformed.

Stephens and Badhwar (ref. 19) used photon production data from Fidecaro et al. (ref. 13) to derive pion production cross sections. The variables  $T_{\text{lab}}$ ,  $\theta$ , and  $p$  were used by Stephens. Equation (B6) was used to transform  $T_{\text{lab}}$  into  $\sqrt{s}$ . Next,  $\theta$  was transformed to  $\theta^*$  by using equation (B15). Finally,  $p$  was transformed into  $p_t$  by using the equation  $p_t = p \sin \theta$ .

## References

1. Fernow, Richard C.: *Introduction to Experimental Particle Physics*. Cambridge Univ. Press, 1986.
2. Rao, M. V. S.; and Sreekantan, B. V.: *Extensive Air Showers*. World Sci., 1998.
3. Gaisser, Thomas K.: *Cosmic Rays and Particle Physics*. Cambridge Univ. Press, 1990.
4. Sokolsky, Pierre: *Introduction to Ultrahigh Energy Cosmic Ray Physics*. Addison-Wesley Publ. Co., Inc., 1989.
5. Wilson, John W.; Townsend, Lawrence W.; et al.: *Transport Methods and Interactions for Space Radiations*. NASA RP-1257, 1991.
6. Shinn, J. L.; Cucinotta, F. A.; et al.: Validation of a Comprehensive Space Radiation Transport Code. *IEEE Trans. Nucl. Sci.*, vol. 45, no. 6, Dec. 1998, pp. 2711-2719.
7. Longair, M. S.: *High Energy Astrophysics: Volume 2—Stars, the Galaxy and the Interstellar Medium*. Second ed., Cambridge Univ. Press, 1994.
8. Dermer, Charles D.: Binary Collision Rates of Relativistic Thermal Plasmas: II Spectra. *Astrophys. J.*, vol. 307, Aug. 1986, pp. 47-59.
9. Stecker, F. W.; Done, C.; Salamon, M. H.; and Sommers, P.: High-Energy Neutrinos From Active Galactic Nuclei. *Phys. Rev. Lett.*, vol. 66, no. 21, May 1991, pp. 2697-2700; Errata, vol. 69, no. 18, Nov. 1992, p. 2738.
10. Protheroe, R. J.: High Energy Particles From Active Galactic Nuclei. *Nucl. Phys. B (Proc. Suppl.)*, vol. 43, 1995, pp. 229-236.
11. Mahadevan, Rohan; Narayan, Ramesh; and Krolik, Julian: Gamma-Ray Emission From Advection-Dominated Accretion Flows Around Black Holes: Application to the Galactic Center. *Astrophys. J.*, vol. 486, Sept. 1997, pp. 268-275.
12. Büsser, F. W.; Camilleri, L.; et al.: Observation of  $\pi^0$  Mesons With Large Transverse Momentum in High-Energy Proton-Proton Collisions. *Phys. Lett.*, vol. 46B, no. 3, Oct. 1973, pp. 471-476.
13. Fidecaro, M.; Finocchiaro, G.; et al.: Photon Production in Proton-Proton Collisions at 23.1 GeV. *Nuovo Cimento*, vol. XXIV, no. 1, Apr. 1962, pp. 73-86.
14. Carey, D. C.; Johnson, J. R.; et al.: Inclusive  $\pi^0$  Production by High-Energy Protons. *Phys. Rev. D*, vol. 14, no. 5, Sept. 1976, pp. 1196-1216.
15. Büsser, F. W.; Camilleri, L.; et al.: A Study of Inclusive Spectra and Two-Particle Correlations at Large Transverse Momentum. *Nucl. Phys.*, vol. B106, 1976, pp. 1-30.
16. Eggert, K.; Giboni, K. L.; et al.: A Study of High Transverse Momentum  $\pi^0$ 's at ISR Energies. *Nucl. Phys.*, vol. B98, 1975, pp. 49-72.
17. Owen, Lloyd; Abshire, G. W.; et al.: Angular Dependence of High- $p_T$   $\pi^0$  Production. *Phys. Rev. Lett.*, vol. 45, no. 2, July 1980, pp. 89-93.
18. Angelis, A. L. S.; Basini, G.; et al.: Large Transverse Momentum  $\pi^0$  Production in  $aa$ ,  $dd$  and  $pp$  Collisions at the CERN ISR. *Phys. Lett. B*, vol. 185, no. 1 & 2, Feb. 1987, pp. 213-217.
19. Stephens, S. A.; and Badhwar, G. D.: Production Spectrum of Gamma Rays in Interstellar Space Through Neutral Pion Decay. *Astrophys. & Space Sci.*, vol. 76, 1981, pp. 213-233.
20. Albrecht, R.; Antonenko, V.; et al.: Transverse Momentum Distributions of Neutral Pions From Nuclear Collisions at 200 A GeV. *Eur. Phys. J. C*, vol. 5, 1998, pp. 255-267.
21. Ellis, S. D.; and Stroynowski, R.: Large  $p_T$  Physics: Data and the Constituent Models. *Rev. Modern Phys.*, vol. 49, no. 4, Oct. 1977, pp. 753-775.
22. Carey, D. C.; Johnson, J. R.; et al.: Inclusive  $\pi^0$  Production in  $pp$  Collisions at 50-400 GeV/c\*. *Phys. Rev. Lett.*, vol. 33, no. 5, July 1974, pp. 327-330.
23. Whitmore, J.: Experimental Results on Strong Interactions in the NAL Hydrogen Bubble Chamber. *Phys. Rep.*, vol. 10, no. 5, 1974, pp. 273-373.
24. SPSS Inc.: *Table Curve 3D*, Version 3.0. AISN Software Inc., 1997.
25. Alper, B.; Böggild, H.; et al.: Production Spectra of  $\pi^\pm$ ,  $K^\pm$ ,  $p^\pm$  at Large Angles in Proton-Proton Collisions in the CERN Intersecting Storage Rings. *Nucl. Phys.*, vol. B100, 1975, pp. 237-290.

26. Capiluppi, P.; Giacomelli, G.; et al.: Charged Particle Production in Proton-Proton Inclusive Reactions at Very High Energies. *Nucl. Phys. B*, vol. 79, 1974, pp. 189–258.
27. Capiluppi, P.; Giacomelli, G.; et al.: Transverse Momentum Dependence in Proton-Proton Inclusive Reactions at Very High Energies. *Nucl. Phys. B*, vol. 70, 1974, pp. 1–38.
28. Albrow, M. G.; Barber, D. P.; et al.: The Distribution in Transverse Momentum of 5 GeV/c Secondaries Produced at 53 GeV in the Centre of Mass. *Phys. Lett.*, vol. 42B, no. 2, Nov. 1972, pp. 279–282.
29. Carey, D. C.; Johnson, J. R.; et al.: Unified Description of Single-Particle Production in  $pp$  Collisions. *Phys. Rev. Lett.*, vol. 33, no. 5, July 1974, pp. 330–333.
30. Badhwar, G. D.; Stephens, S. A.; and Golden, R. L.: Analytic Representation of the Proton-Proton and Proton-Nucleus Cross-Sections and Its Application to the Sea-Level Spectrum and Charge Ratio of Muons. *Phys. Rev. D*, vol. 15, no. 3, Feb. 1977, pp. 820–831.
31. Mokhov, N. V.; and Striganov, S. I.: Model for Pion Production in Proton-Nucleus Interactions. *Workshop on the Front End of a Muon Collider*, S. Geer and R. Raja, eds., Am. Inst. Phys., 1998, pp. 453–459.
32. Byckling, E.; and Kajantie, K.: *Particle Kinematics*. John Wiley & Sons, 1973.

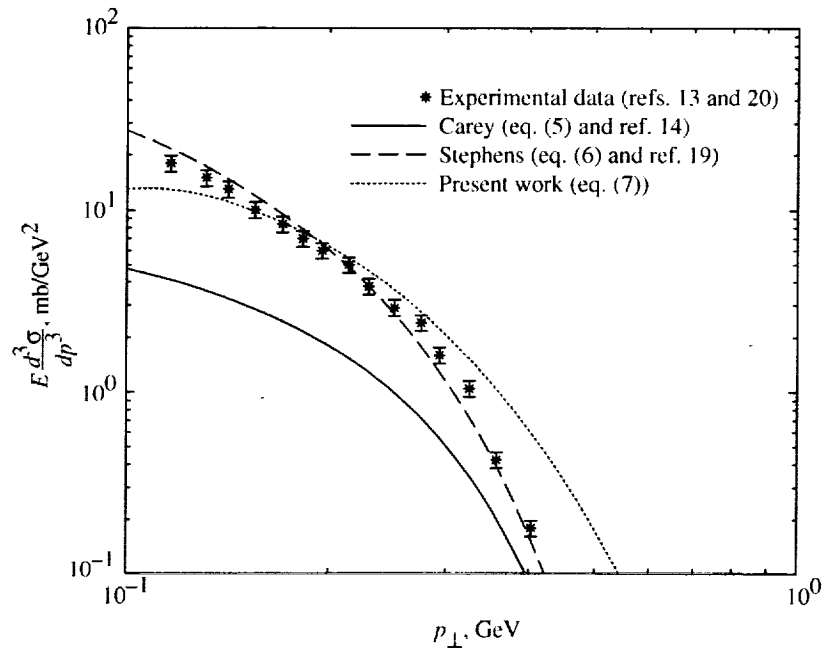


Figure 1. LIDCS plotted against transverse momentum for  $\pi^0$  production for  $E_{cm} = 7$  GeV and  $\theta^* = 12^\circ$  with data at  $12.2^\circ < \theta^* < 12.4^\circ$ .

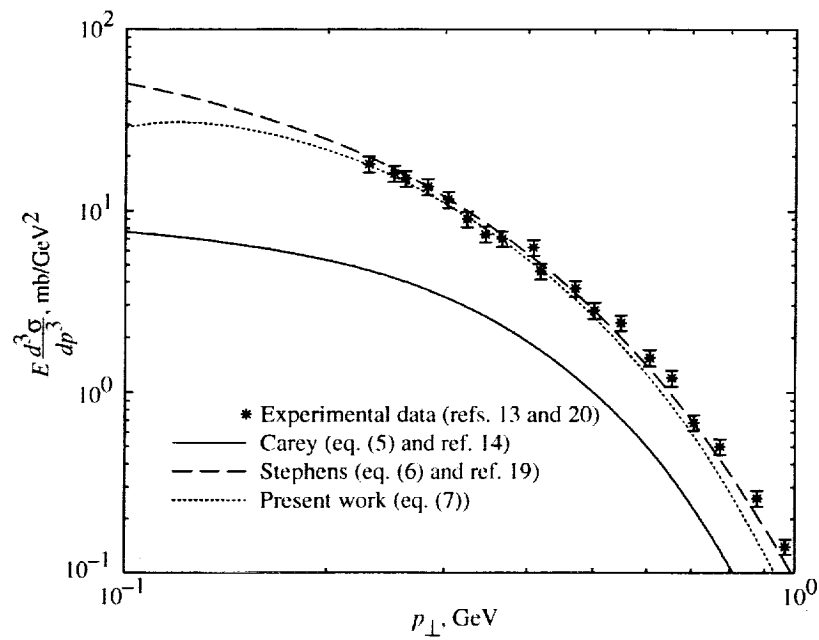


Figure 2. LIDCS plotted against transverse momentum for  $\pi^0$  production for  $E_{cm} = 7$  GeV and  $\theta^* = 41^\circ$  with data at  $40.3^\circ < \theta^* < 41.9^\circ$ .

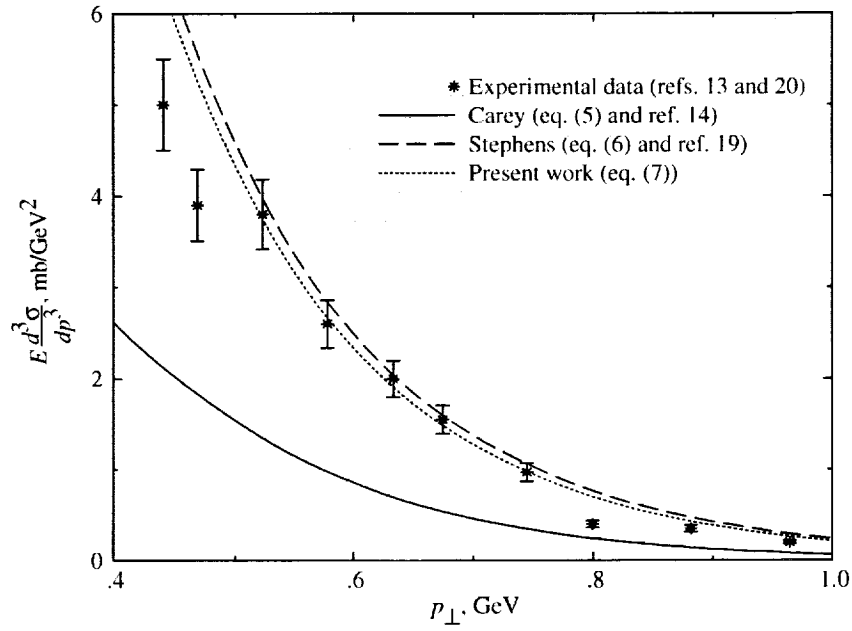


Figure 3. LIDCS plotted against transverse momentum for  $\pi^0$  production for  $E_{cm} = 7$  GeV and  $\theta^* = 89^\circ$  with data at  $88.3^\circ < \theta^* < 90^\circ$ .

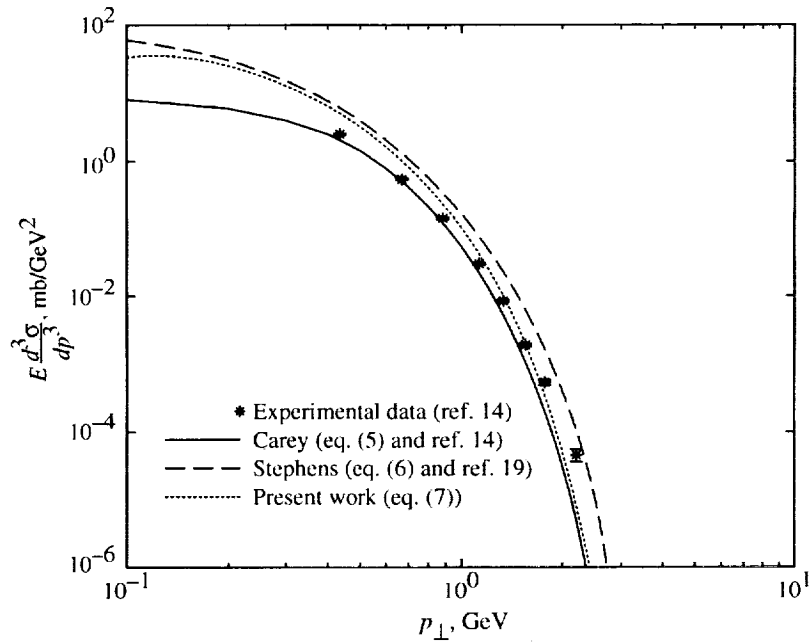


Figure 4. LIDCS plotted against transverse momentum for  $\pi^0$  production for  $E_{cm} = 9.8$  GeV and  $\theta^* = 37^\circ$  with data at  $37.1^\circ < \theta^* < 37.5^\circ$ .

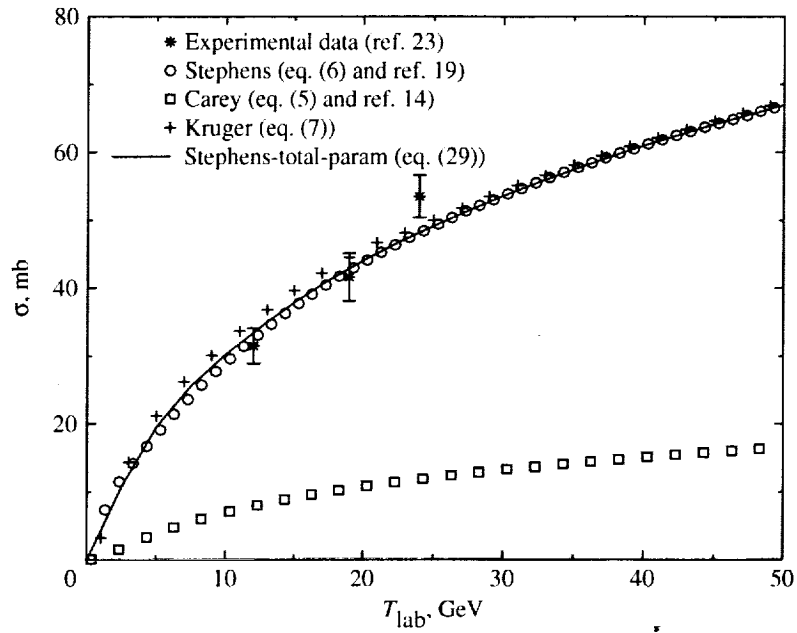


Figure 5. Parameterization of total  $\pi^0$  production cross section plotted with numerically integrated LIDCS parameterizations.

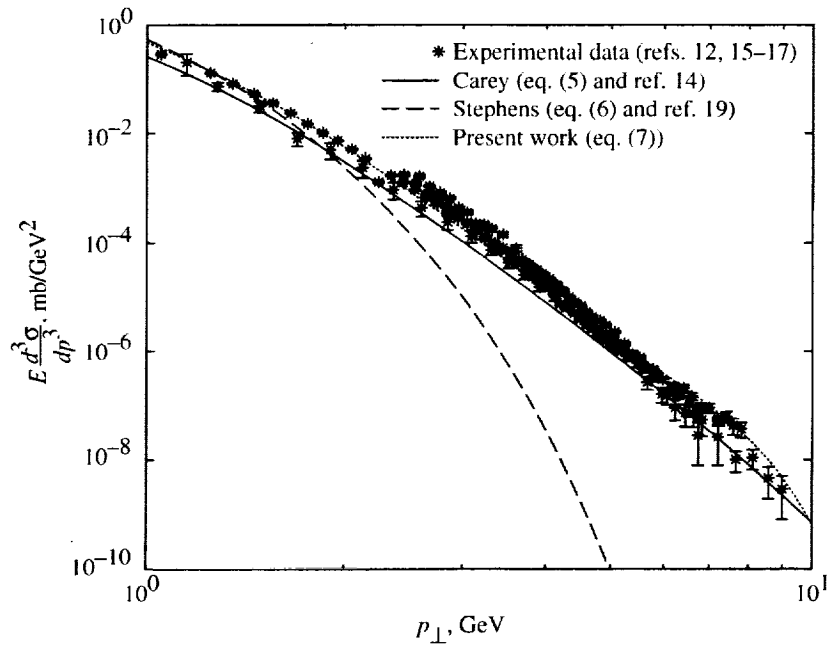


Figure 6. LIDCS plotted against transverse momentum for  $\pi^0$  production for  $E_{cm} = 53$  GeV and  $\theta^* = 90^\circ$  with data at  $\theta^* = 90^\circ$ .

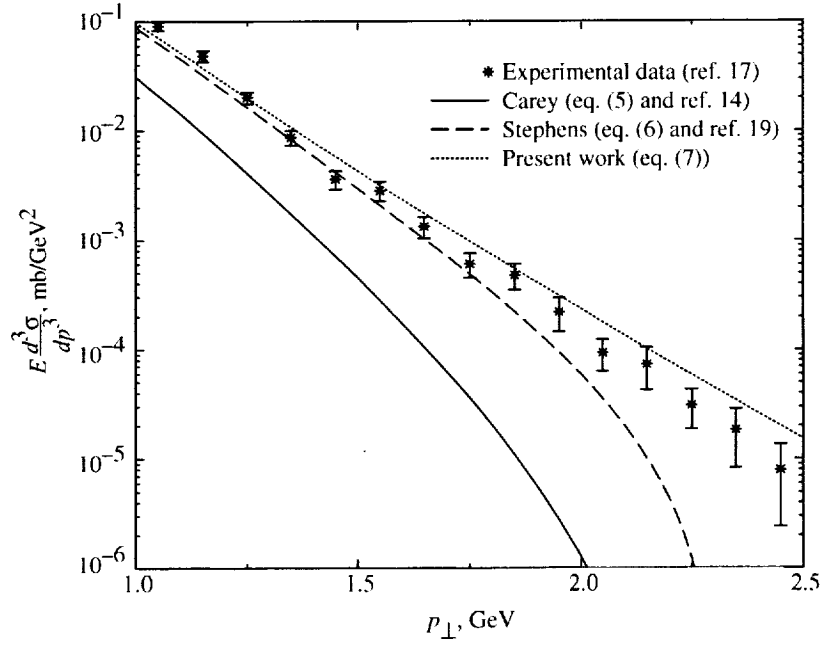


Figure 7. LIDCS plotted against transverse momentum for  $\pi^0$  production for  $E_{cm} = 53$  GeV and  $\theta^* = 5^\circ$  with data at  $\theta^* = 5^\circ$ .

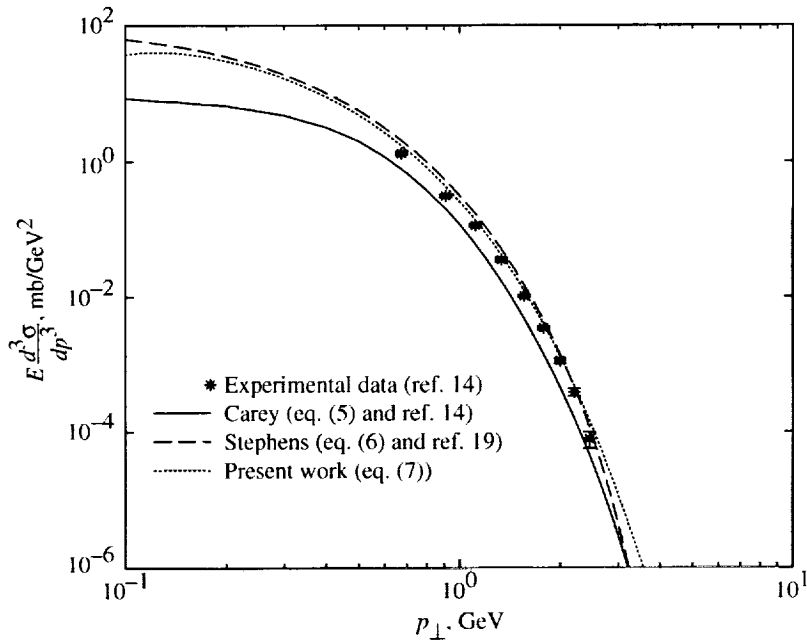


Figure 8. LIDCS plotted against transverse momentum for  $\pi^0$  production for  $E_{cm} = 9.8$  GeV and  $\theta^* = 87^\circ$  with data at  $86.8^\circ < \theta^* < 87.9^\circ$ .

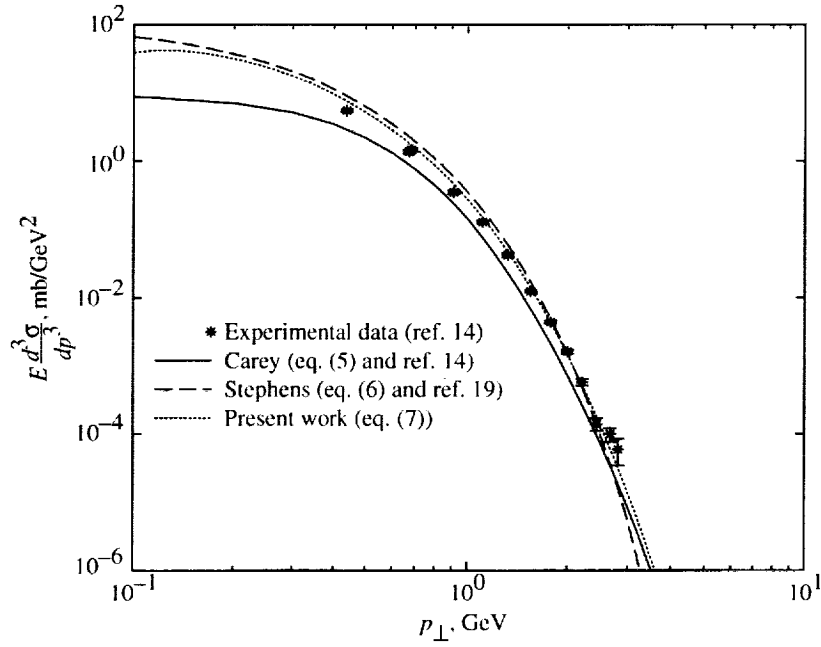


Figure 9. LIDCS plotted against transverse momentum for  $\pi^0$  production for  $E_{cm} = 12$  GeV and  $\theta^* = 76^\circ$  with data at  $74.4^\circ < \theta^* < 76.4^\circ$ .

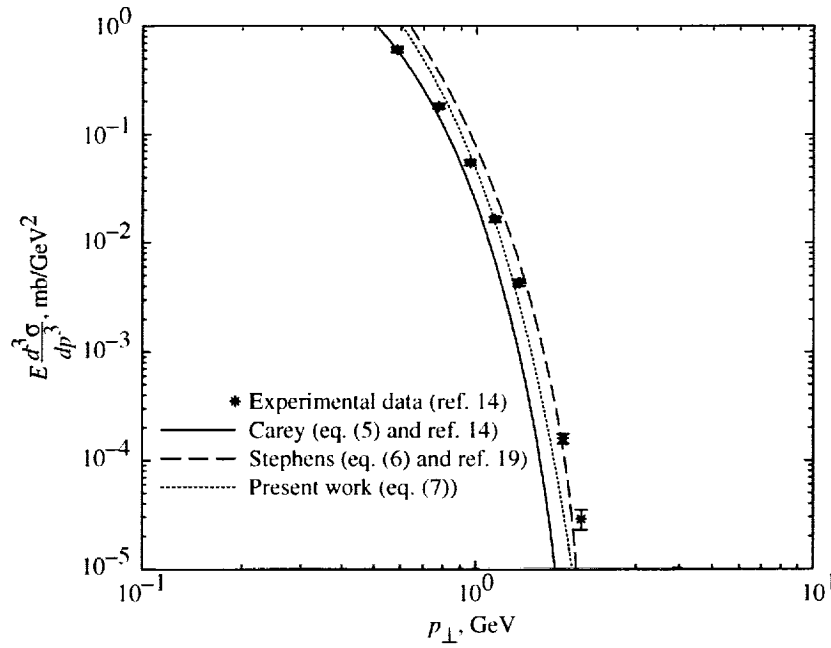


Figure 10. LIDCS plotted against transverse momentum for  $\pi^0$  production for  $E_{cm} = 12$  GeV and  $\theta^* = 21^\circ$  with data at  $21.4^\circ < \theta^* < 21.6^\circ$ .

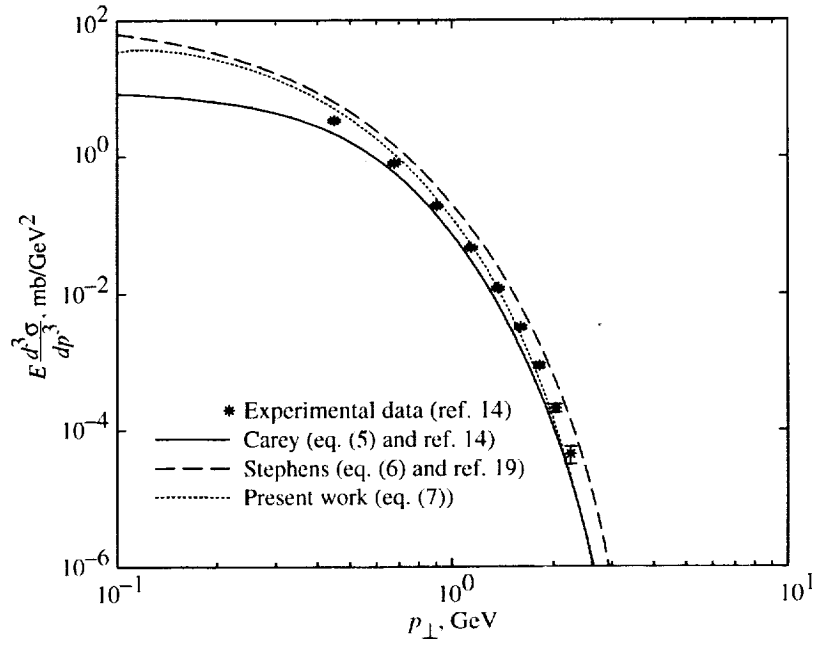


Figure 11. LIDCS plotted against transverse momentum for  $\pi^0$  production for  $E_{cm} = 12$  GeV and  $\theta^* = 35^\circ$  with data at  $35.1^\circ < \theta^* < 35.4^\circ$ .

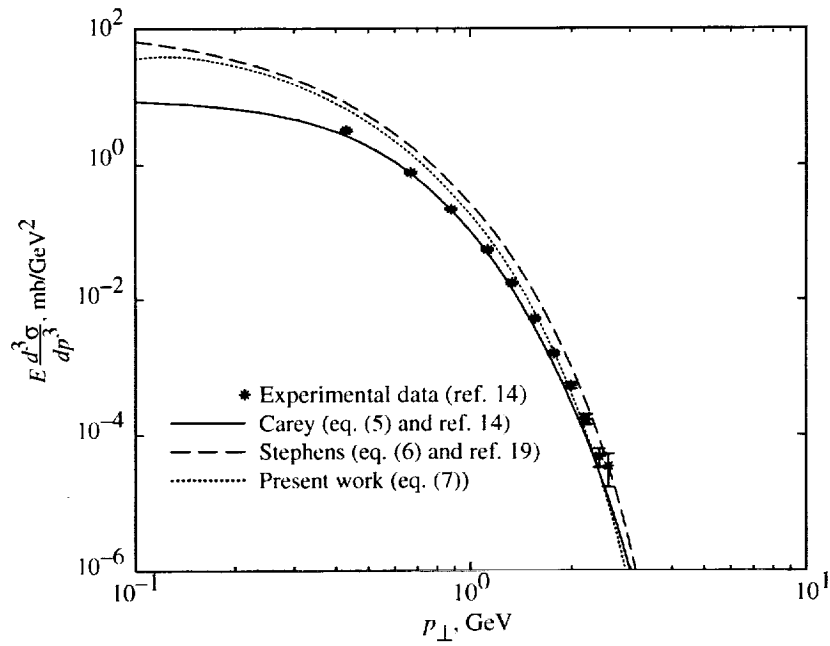


Figure 12. LIDCS plotted against transverse momentum for  $\pi^0$  production for  $E_{cm} = 12$  GeV and  $\theta^* = 45^\circ$  with data at  $44.7^\circ < \theta^* < 45.3^\circ$ .

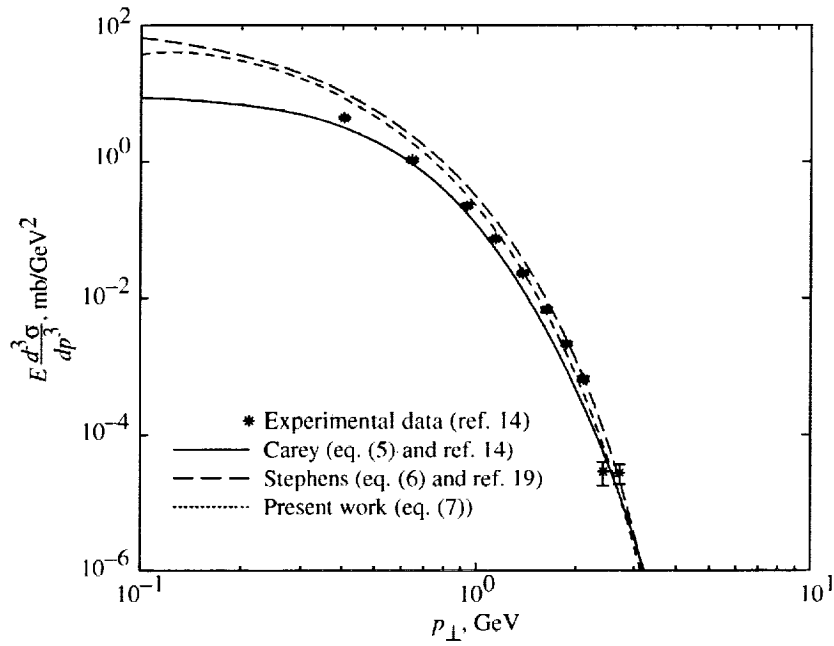


Figure 13. LIDCS plotted against transverse momentum for  $\pi^0$  production for  $E_{cm} = 12$  GeV and  $\theta^* = 54^\circ$  with data at  $53.7^\circ < \theta^* < 54.8^\circ$ .

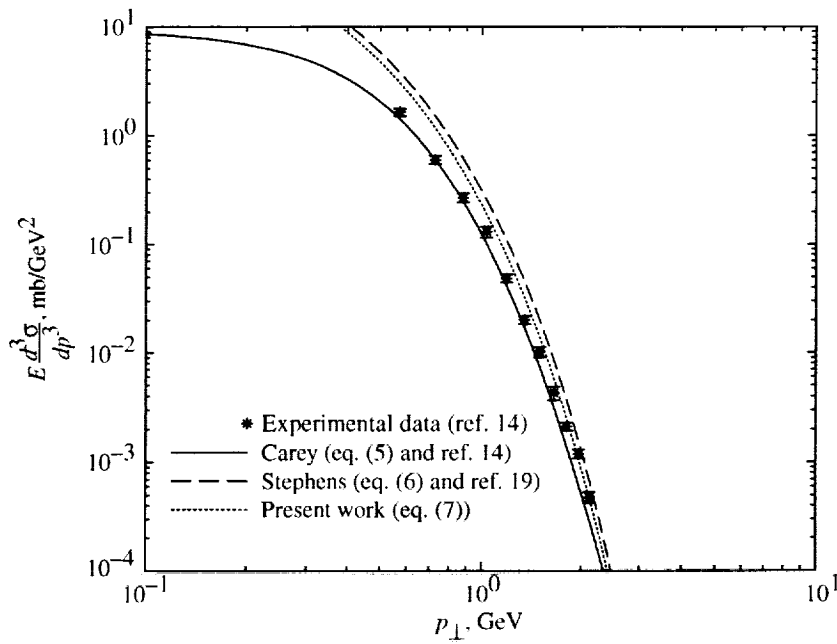


Figure 14. LIDCS plotted against transverse momentum for  $\pi^0$  production for  $E_{cm} = 12$  GeV and  $\theta^* = 58^\circ$  with data at  $57.5^\circ < \theta^* < 59.4^\circ$ .

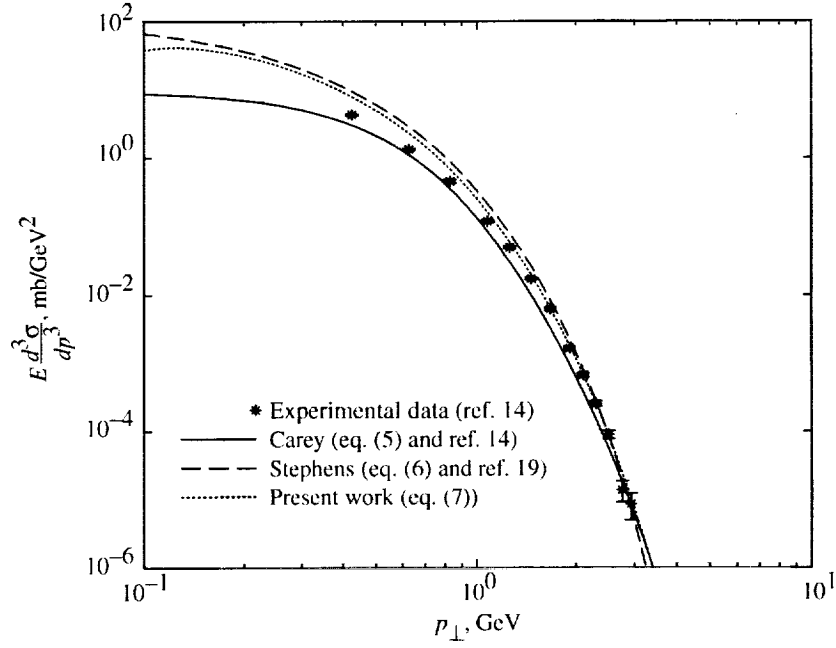


Figure 15. LIDCS plotted against transverse momentum for  $\pi^0$  production for  $E_{cm} = 12$  GeV and  $\theta^* = 65^\circ$  with data at  $64.6^\circ < \theta^* < 66.2^\circ$ .

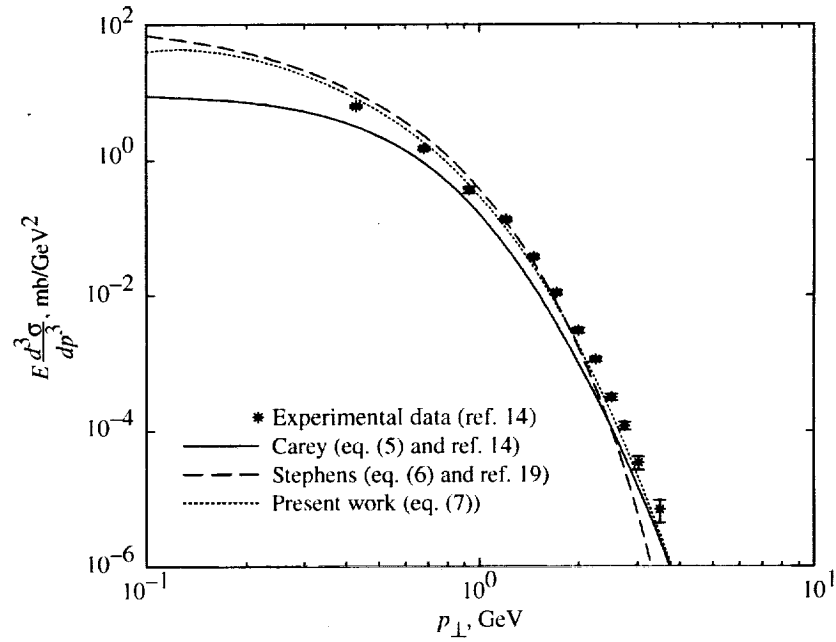


Figure 16. LIDCS plotted against transverse momentum for  $\pi^0$  production for  $E_{cm} = 13.7$  GeV and  $\theta^* = 83^\circ$  with data at  $82.2^\circ < \theta^* < 84.7^\circ$ .

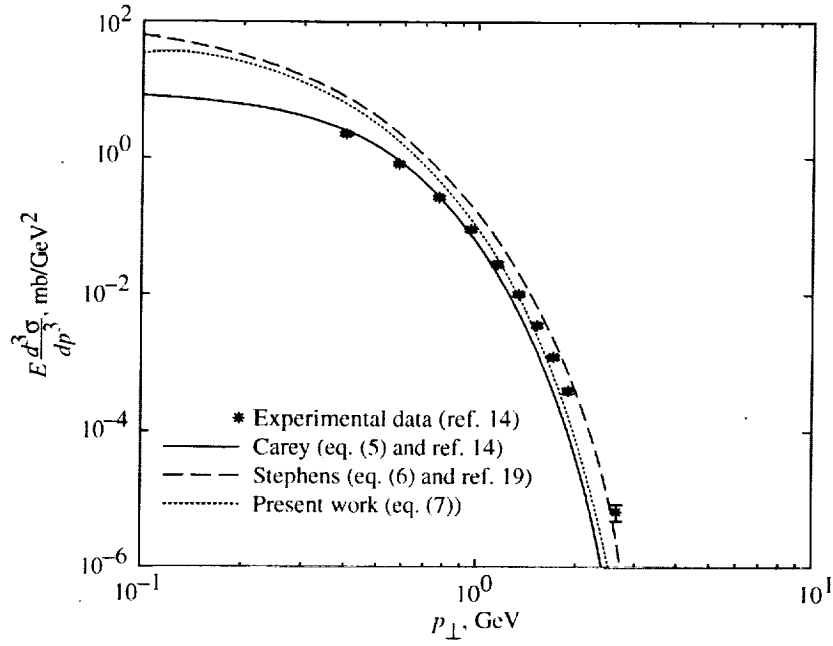


Figure 17. LIDCS plotted against transverse momentum for  $\pi^0$  production for  $E_{cm} = 14$  GeV and  $\theta^* = 25^\circ$  with data at  $24.7^\circ < \theta^* < 24.9^\circ$ .

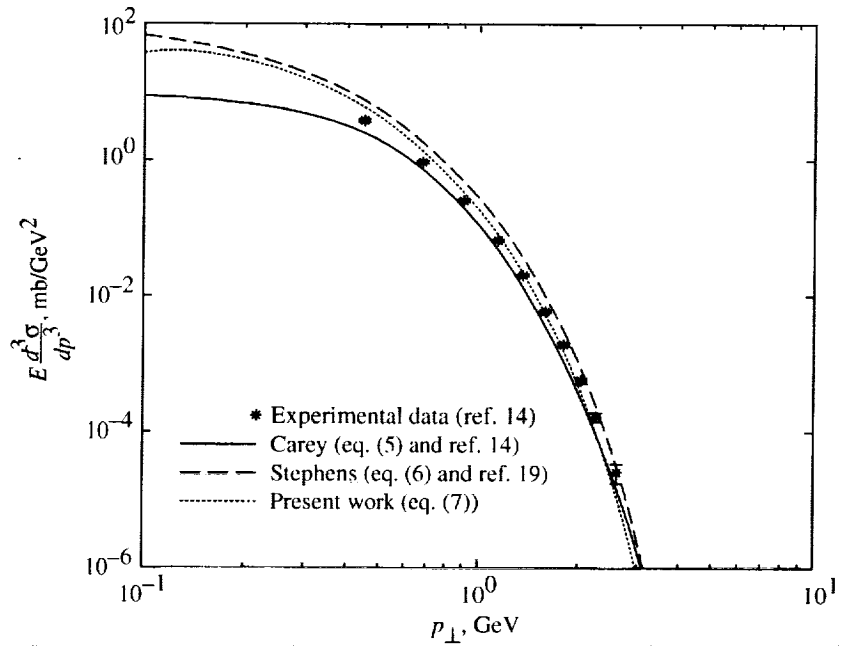


Figure 18. LIDCS plotted against transverse momentum for  $\pi^0$  production for  $E_{cm} = 14$  GeV and  $\theta^* = 40^\circ$  with data at  $40.1^\circ < \theta^* < 40.6^\circ$ .

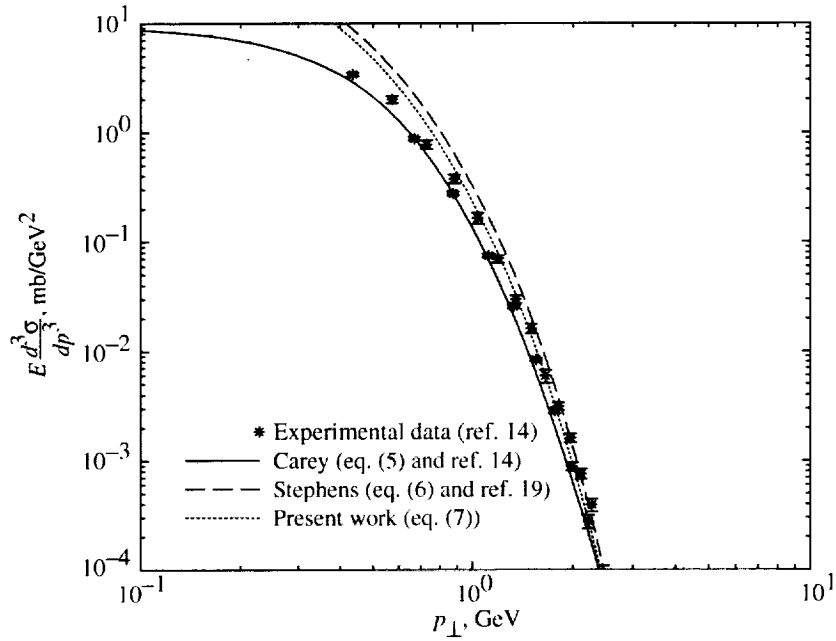


Figure 19. LIDCS plotted against transverse momentum for  $\pi^0$  production for  $E_{cm} = 14$  GeV and  $\theta^* = 51^\circ$  with data at  $50.7^\circ < \theta^* < 52.6^\circ$ .

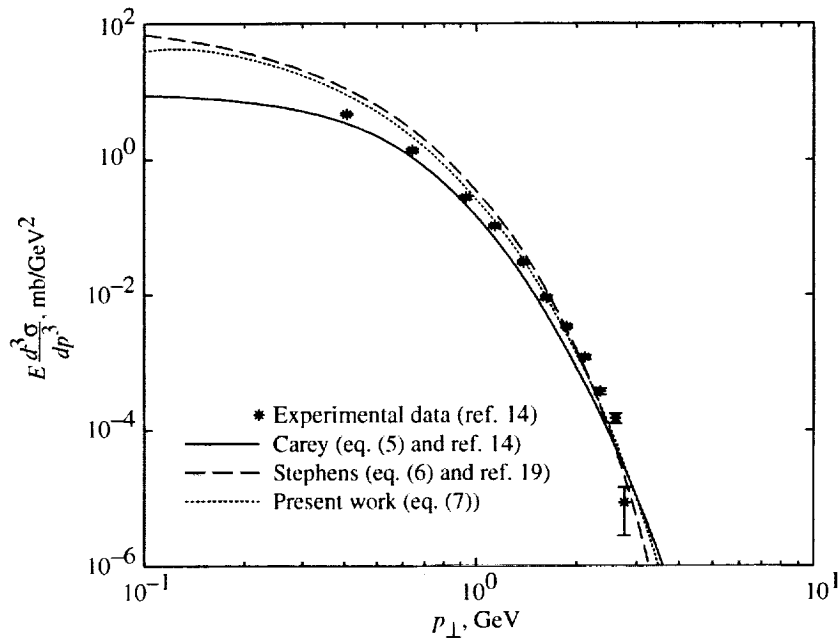


Figure 20. LIDCS plotted against transverse momentum for  $\pi^0$  production for  $E_{cm} = 14$  GeV and  $\theta^* = 61^\circ$  with data at  $60.6^\circ < \theta^* < 62.1^\circ$ .

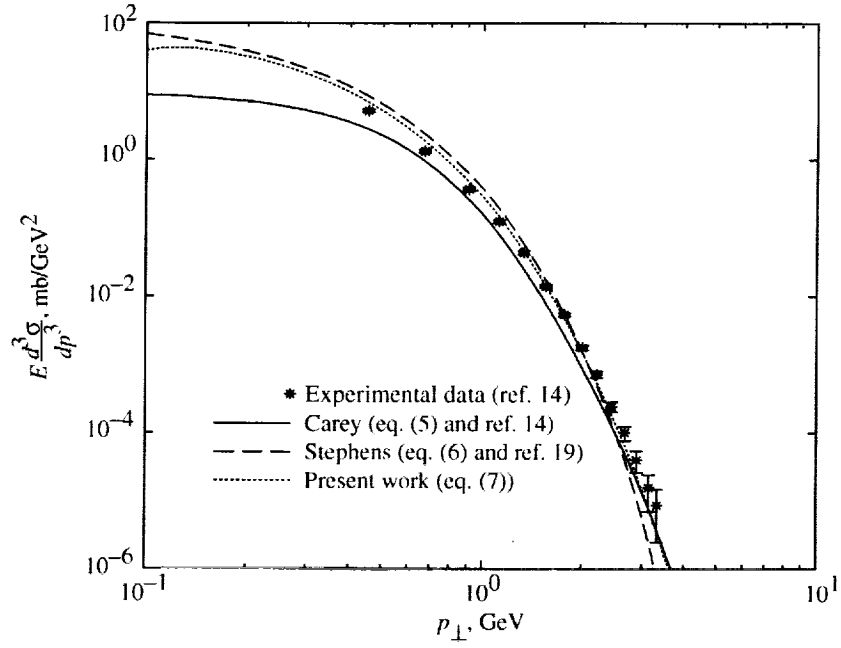


Figure 21. LIDCS plotted against transverse momentum for  $\pi^0$  production for  $E_{cm} = 14$  GeV and  $\theta^* = 67^\circ$  with data at  $65.5^\circ < \theta^* < 68.6^\circ$ .

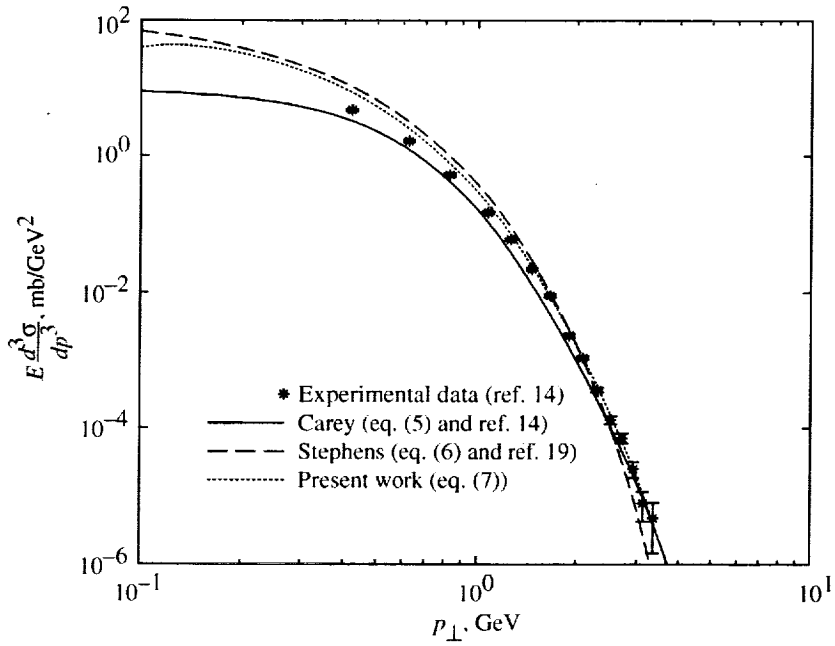


Figure 22. LIDCS plotted against transverse momentum for  $\pi^0$  production for  $E_{cm} = 14$  GeV and  $\theta^* = 73^\circ$  with data at  $72.3^\circ < \theta^* < 74.3^\circ$ .

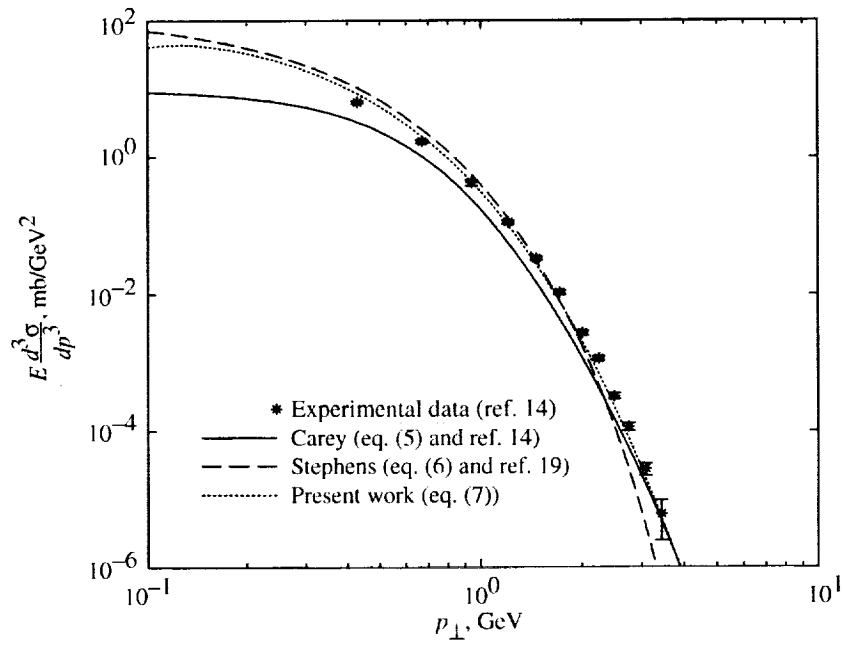


Figure 23. LIDCS plotted against transverse momentum for  $\pi^0$  production for  $E_{cm} = 15.3$  GeV and  $\theta^* = 89^\circ$ , with data at  $88.6^\circ < \theta^* < 89.8^\circ$ .

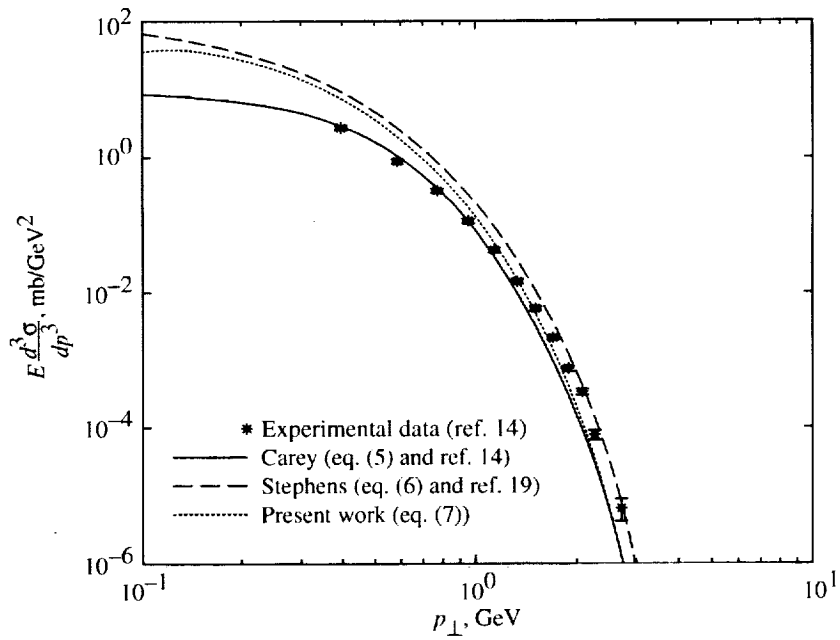


Figure 24. LIDCS plotted against transverse momentum for  $\pi^0$  production for  $E_{cm} = 15.4$  GeV and  $\theta^* = 28^\circ$  with data at  $27.5^\circ < \theta^* < 27.7^\circ$ .

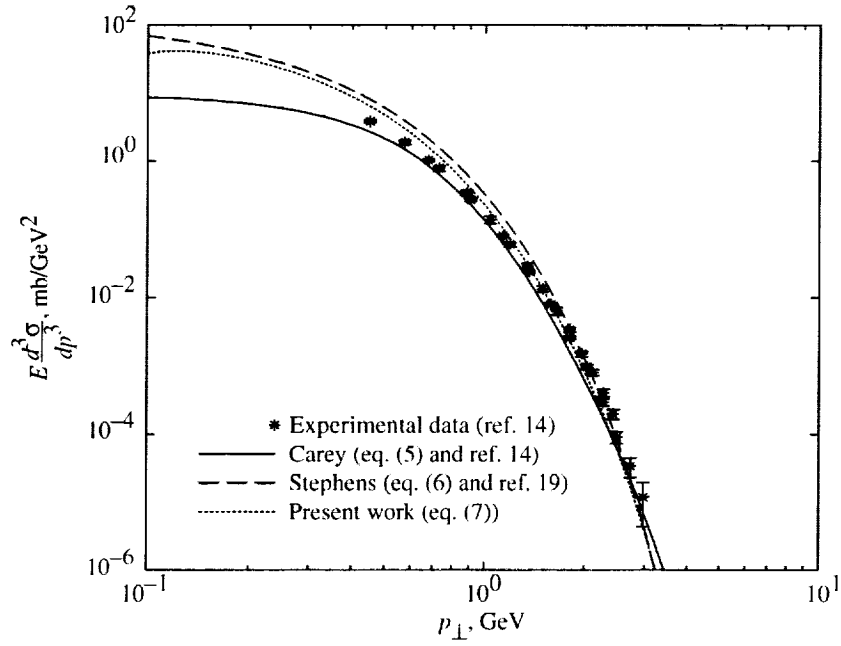


Figure 25. LIDCS plotted against transverse momentum for  $\pi^0$  production for  $E_{cm} = 15.4$  GeV and  $\theta^* = 45^\circ$  with data at  $44.4^\circ < \theta^* < 47.7^\circ$ .

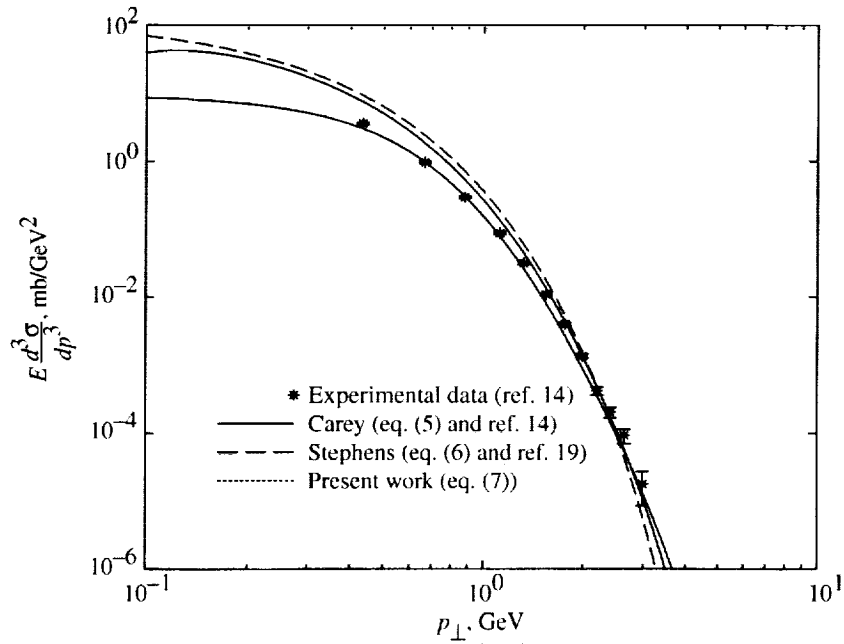


Figure 26. LIDCS plotted against transverse momentum for  $\pi^0$  production for  $E_{cm} = 15.4$  GeV and  $\theta^* = 56^\circ$  with data at  $55.9^\circ < \theta^* < 57^\circ$ .

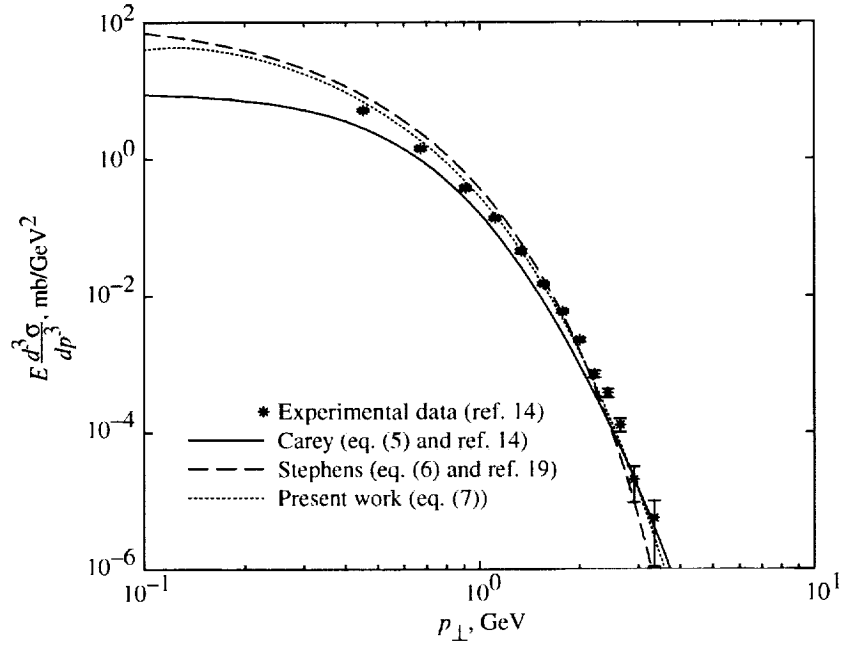


Figure 27. LIDCS plotted against transverse momentum for  $\pi^0$  production for  $E_{cm} = 15.4$  GeV and  $\theta^* = 61^\circ$  with data at  $59.6^\circ < \theta^* < 62.8^\circ$ .

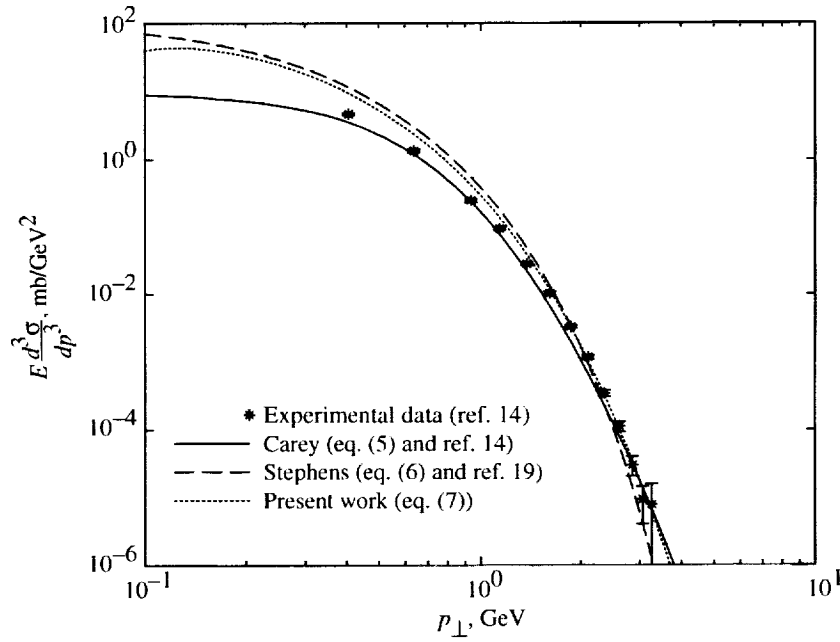


Figure 28. LIDCS plotted against transverse momentum for  $\pi^0$  production for  $E_{cm} = 15.4$  GeV and  $\theta^* = 67^\circ$  with data at  $66.5^\circ < \theta^* < 68.3^\circ$ .

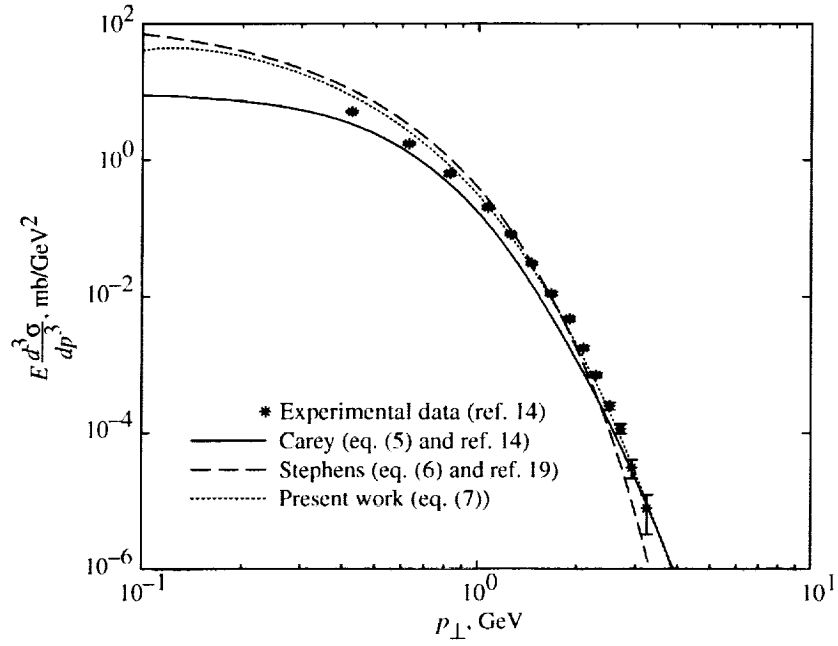


Figure 29. LIDCS plotted against transverse momentum for  $\pi^0$  production for  $E_{cm} = 15.4$  GeV and  $\theta^* = 79^\circ$  with data at  $78.5^\circ < \theta^* < 80.8^\circ$ .

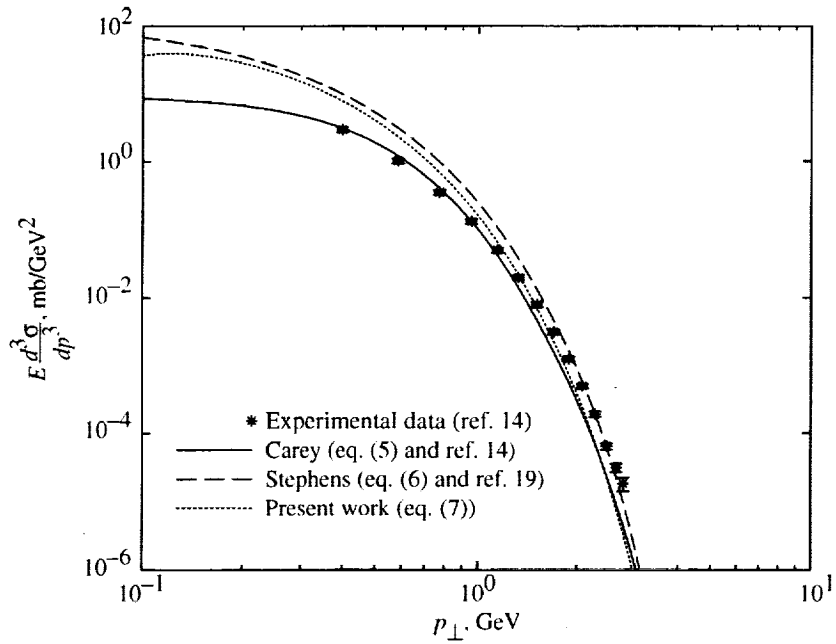


Figure 30. LIDCS plotted against transverse momentum for  $\pi^0$  production for  $E_{cm} = 16.9$  GeV and  $\theta^* = 30^\circ$  with data at  $30.0^\circ < \theta^* < 30.3^\circ$ .

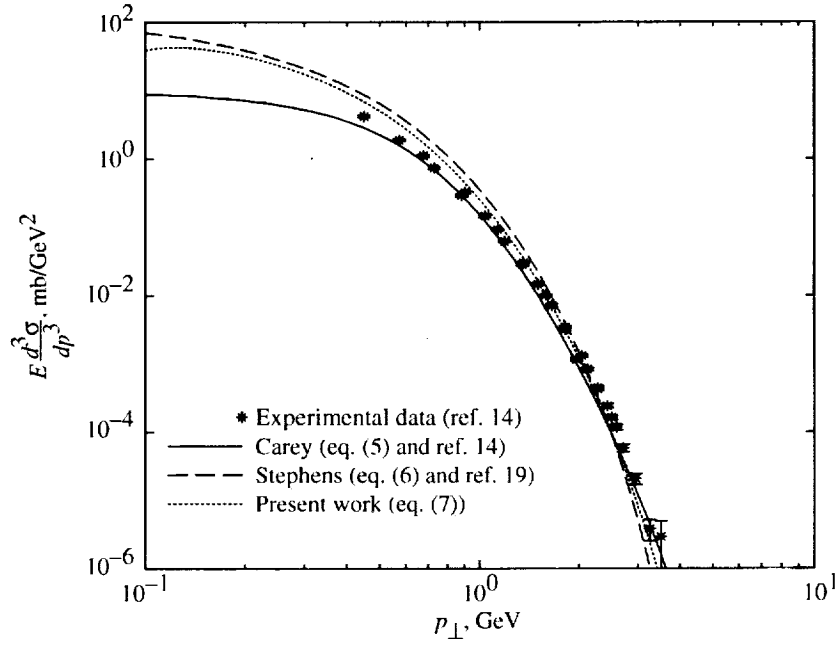


Figure 31. LIDCS plotted against transverse momentum for  $\pi^0$  production for  $E_{cm} = 16.9$  GeV and  $\theta^* = 48^\circ$  with data at  $42.2^\circ < \theta^* < 48.9^\circ$ .

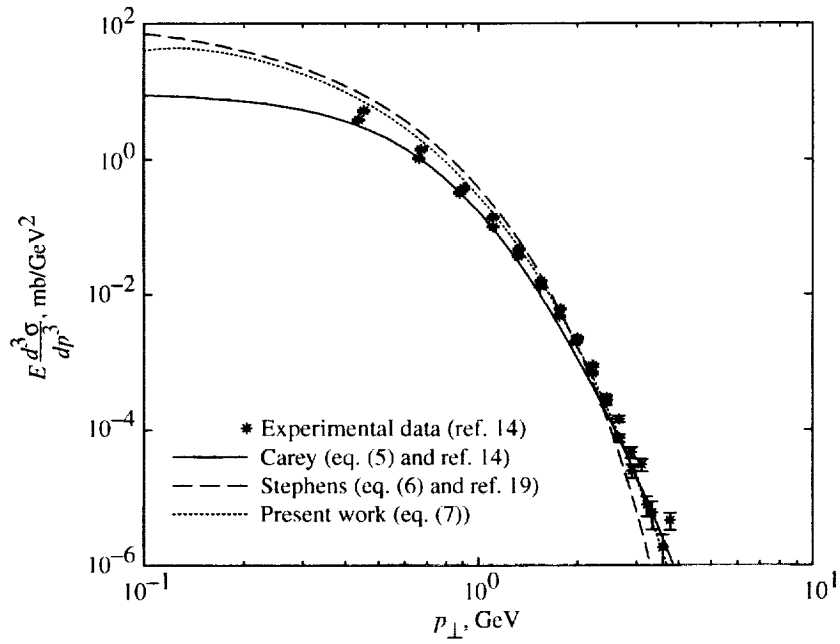


Figure 32. LIDCS plotted against transverse momentum for  $\pi^0$  production for  $E_{cm} = 16.9$  GeV and  $\theta^* = 61^\circ$  with data at  $55.1^\circ < \theta^* < 61.6^\circ$ .

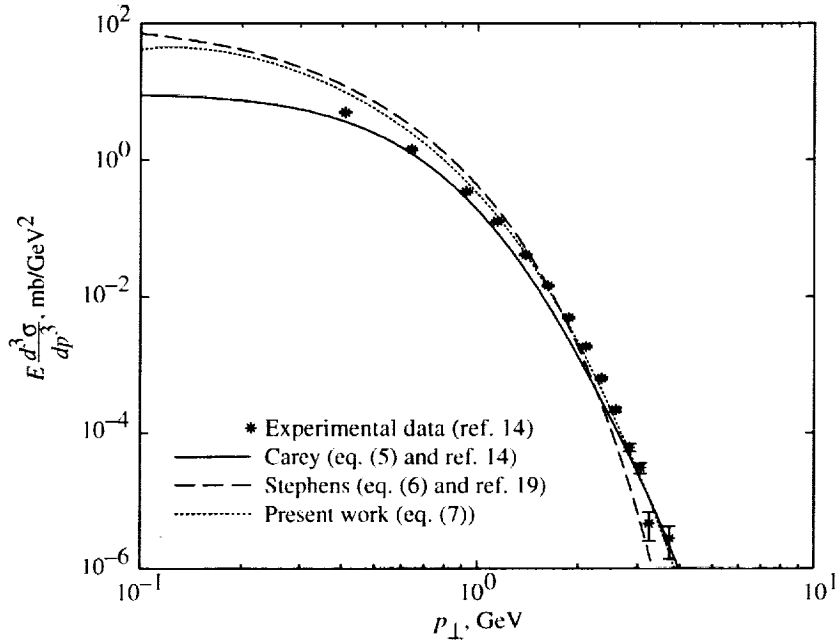


Figure 33. LIDCS plotted against transverse momentum for  $\pi^0$  production for  $E_{cm} = 16.9$  GeV and  $\theta^* = 72^\circ$  with data at  $71.3^\circ < \theta^* < 73.4^\circ$ .

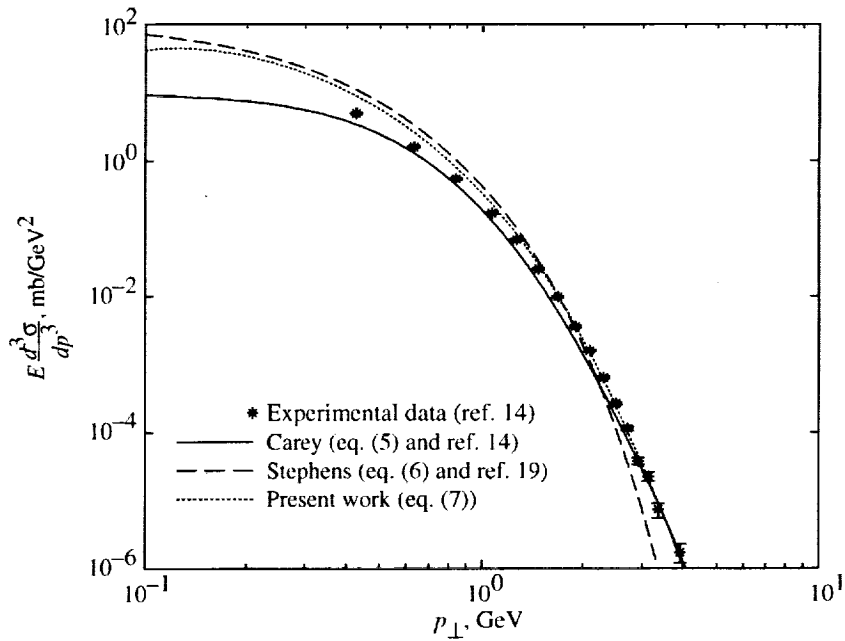


Figure 34. LIDCS plotted against transverse momentum for  $\pi^0$  production for  $E_{cm} = 16.9$  GeV and  $\theta^* = 84^\circ$  with data at  $83.6^\circ < \theta^* < 86.2^\circ$ .

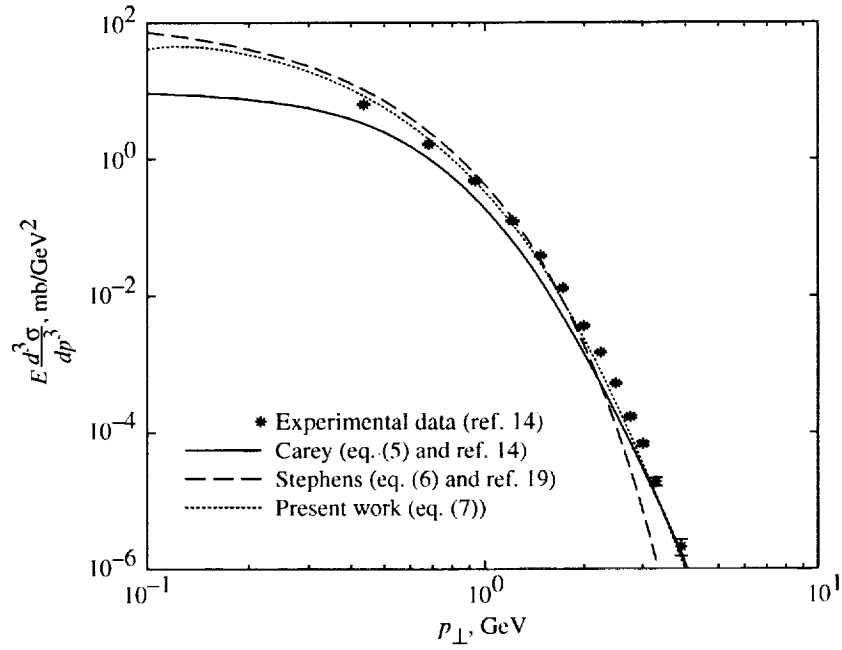


Figure 35. LIDCS plotted against transverse momentum for  $\pi^0$  production for  $E_{cm} = 17.3$  GeV and  $\theta^* = 84^\circ$  with data at  $81.2^\circ < \theta^* < 84.3^\circ$ .

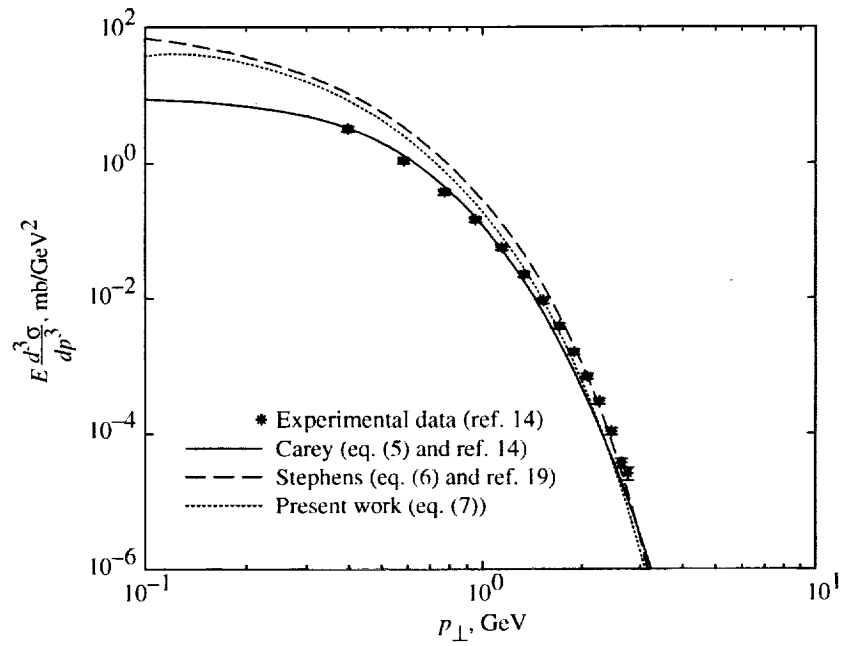


Figure 36. LIDCS plotted against transverse momentum for  $\pi^0$  production for  $E_{cm} = 18.2$  GeV and  $\theta^* = 32^\circ$  with data at  $32.3^\circ < \theta^* < 32.5^\circ$ .

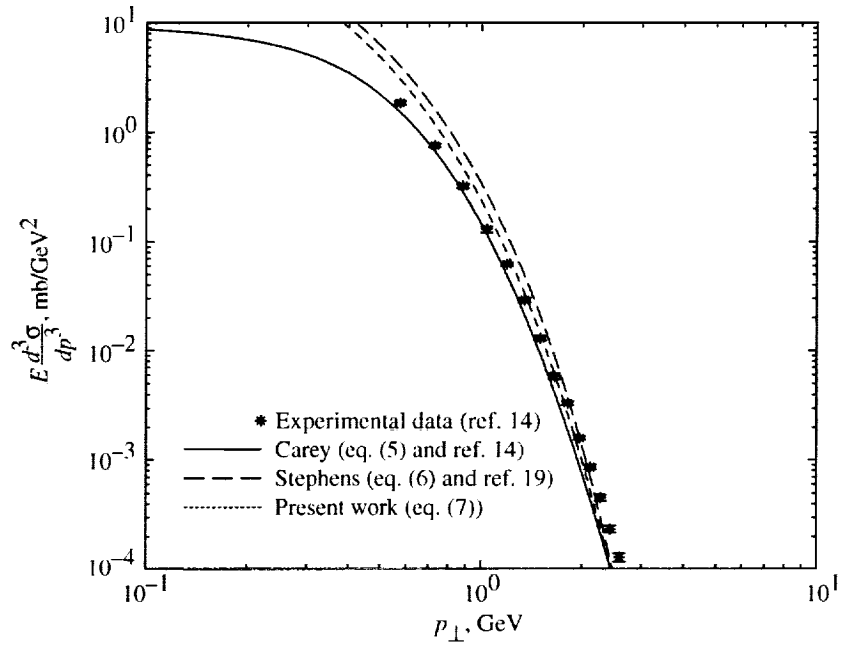


Figure 37. LIDCS plotted against transverse momentum for  $\pi^0$  production for  $E_{cm} = 18.2$  GeV and  $\theta^* = 40^\circ$  with data at  $39.2^\circ < \theta^* < 41^\circ$ .

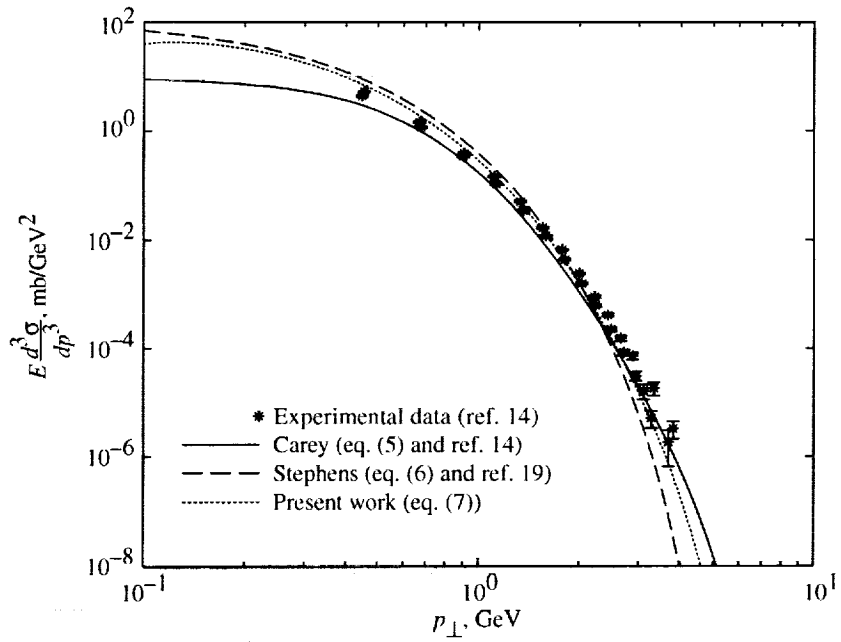


Figure 38. LIDCS plotted against transverse momentum for  $\pi^0$  production for  $E_{cm} = 18.2$  GeV and  $\theta^* = 52^\circ$  with data at  $51.5^\circ < \theta^* < 54.6^\circ$ .

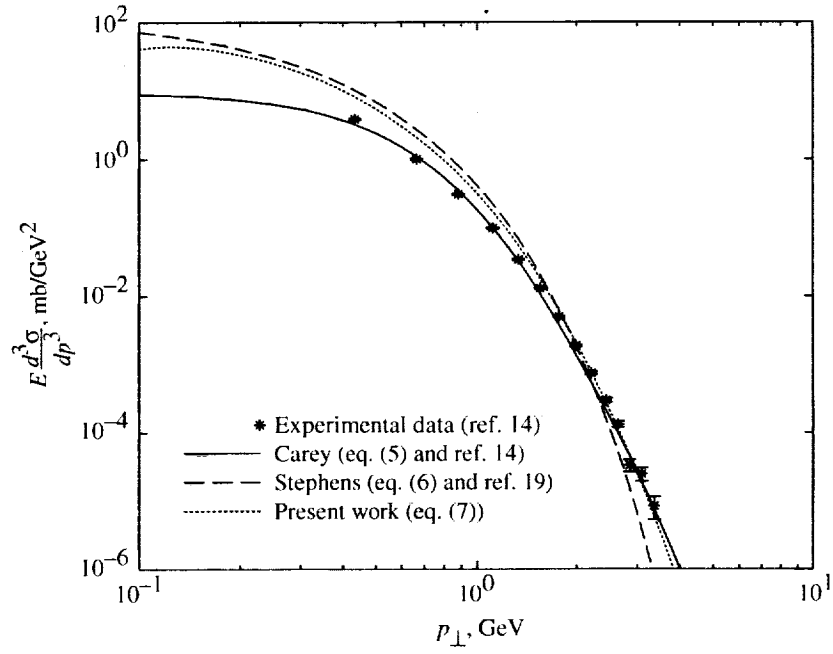


Figure 39. LIDCS plotted against transverse momentum for  $\pi^0$  production for  $E_{cm} = 18.2$  GeV and  $\theta^* = 64^\circ$  with data at  $64.2^\circ < \theta^* < 65.7^\circ$ .

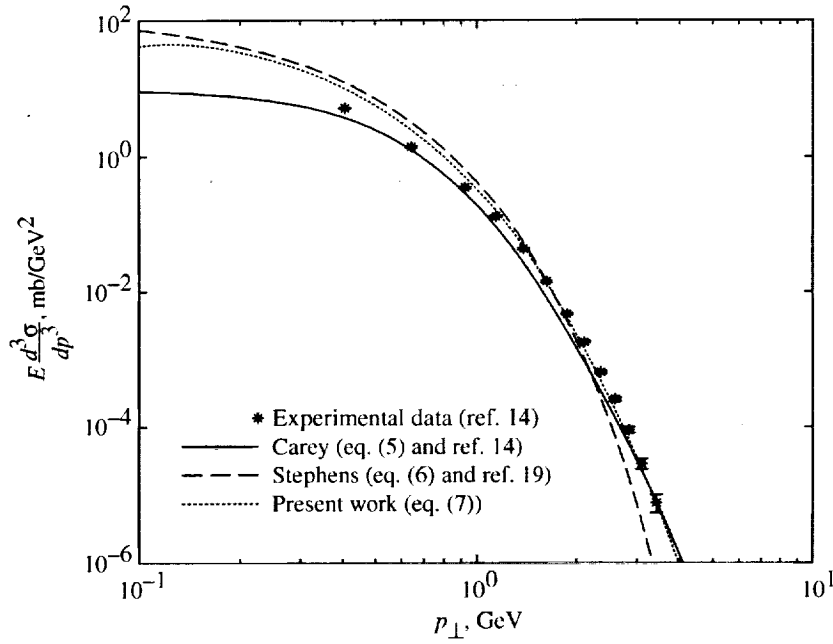


Figure 40. LIDCS plotted against transverse momentum for  $\pi^0$  production for  $E_{cm} = 18.2$  GeV and  $\theta^* = 76^\circ$  with data at  $75.5^\circ < \theta^* < 77.9^\circ$ .

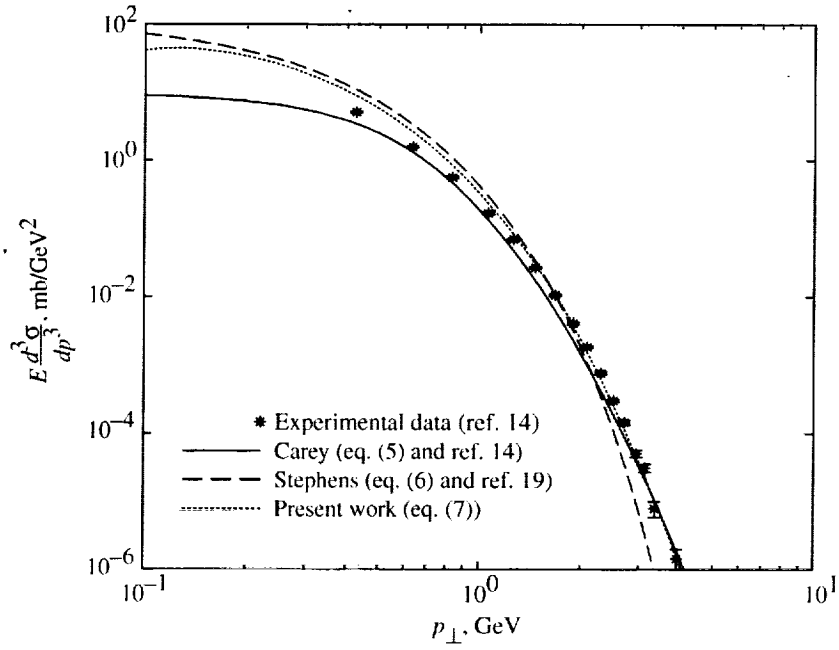


Figure 41. LIDCS plotted against transverse momentum for  $\pi^0$  production for  $E_{cm} = 18.2$  GeV and  $\theta^* = 88^\circ$  with data at  $88^\circ < \theta^* < 89.2^\circ$ .

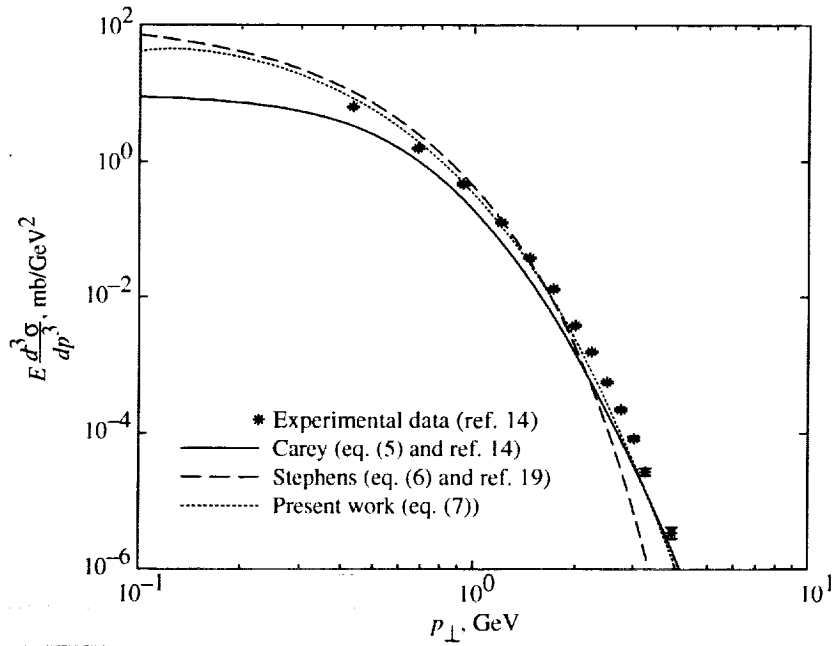


Figure 42. LIDCS plotted against transverse momentum for  $\pi^0$  production for  $E_{cm} = 18.6$  GeV and  $\theta^* = 80^\circ$  with data at  $76.9^\circ < \theta^* < 80.1^\circ$ .

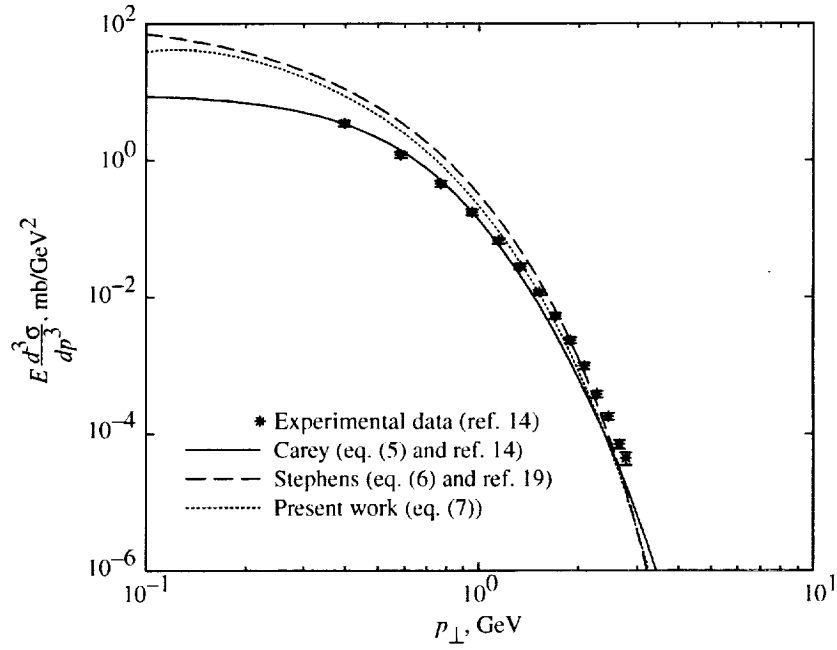


Figure 43. LIDCS plotted against transverse momentum for  $\pi^0$  production for  $E_{cm} = 19.4$  GeV and  $\theta^* = 34^\circ$  with data at  $34.4^\circ < \theta^* < 34.8^\circ$ .

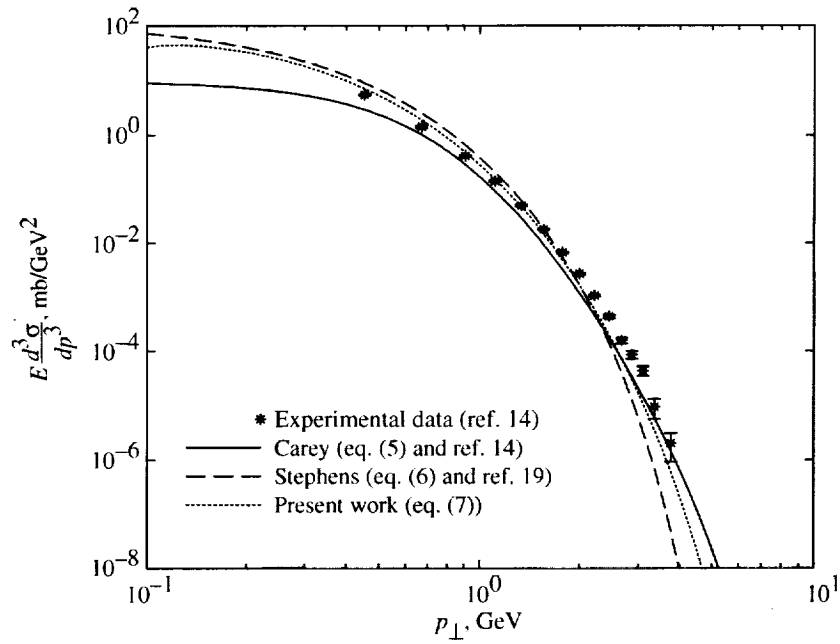


Figure 44. LIDCS plotted against transverse momentum for  $\pi^0$  production for  $E_{cm} = 19.4$  GeV and  $\theta^* = 50^\circ$  with data at  $48.4^\circ < \theta^* < 51.5^\circ$ .

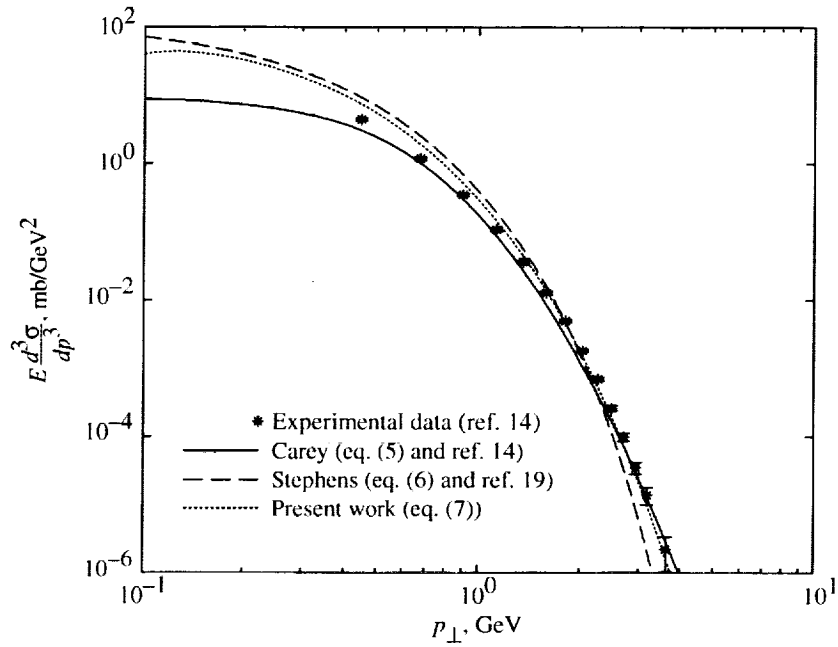


Figure 45. LIDCS plotted against transverse momentum for  $\pi^0$  production for  $E_{cm} = 19.4$  GeV and  $\theta^* = 55^\circ$  with data at  $54.6^\circ < \theta^* < 55.6^\circ$ .

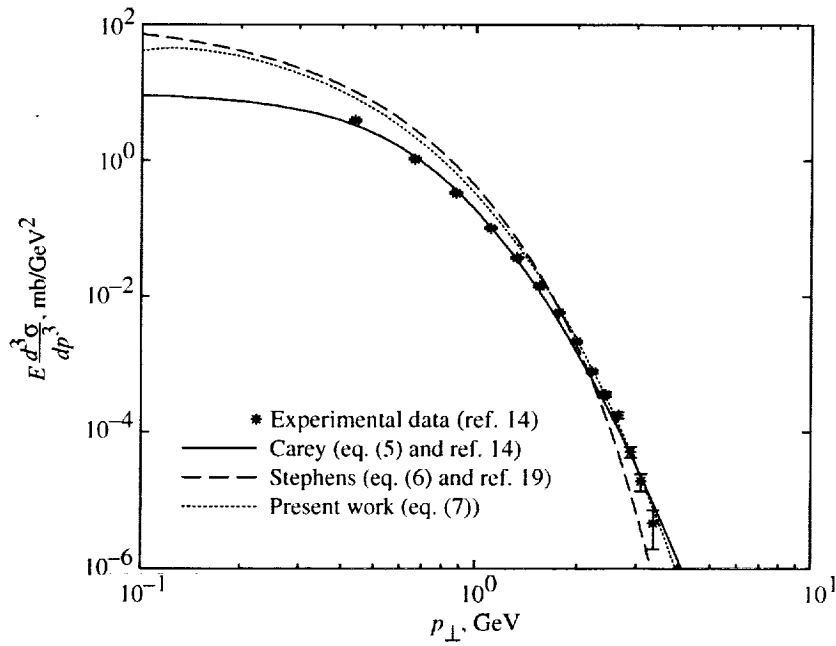


Figure 46. LIDCS plotted against transverse momentum for  $\pi^0$  production for  $E_{cm} = 19.4$  GeV and  $\theta^* = 68^\circ$  with data at  $67.7^\circ < \theta^* < 69.4^\circ$ .

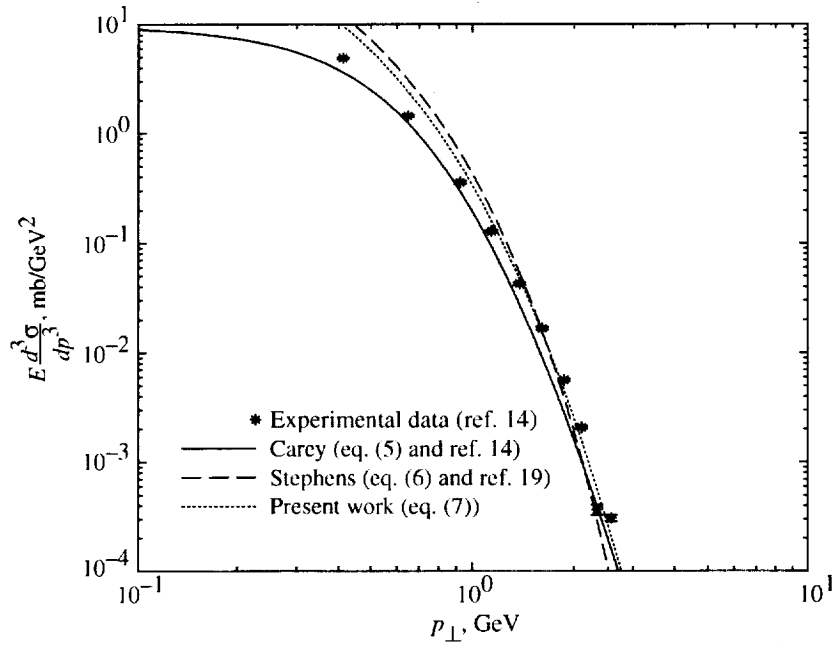


Figure 47. LIDCS plotted against transverse momentum for  $\pi^0$  production for  $E_{cm} = 19.4$  GeV and  $\theta^* = 80^\circ$  with data at  $79.1^\circ < \theta^* < 81.6^\circ$ .

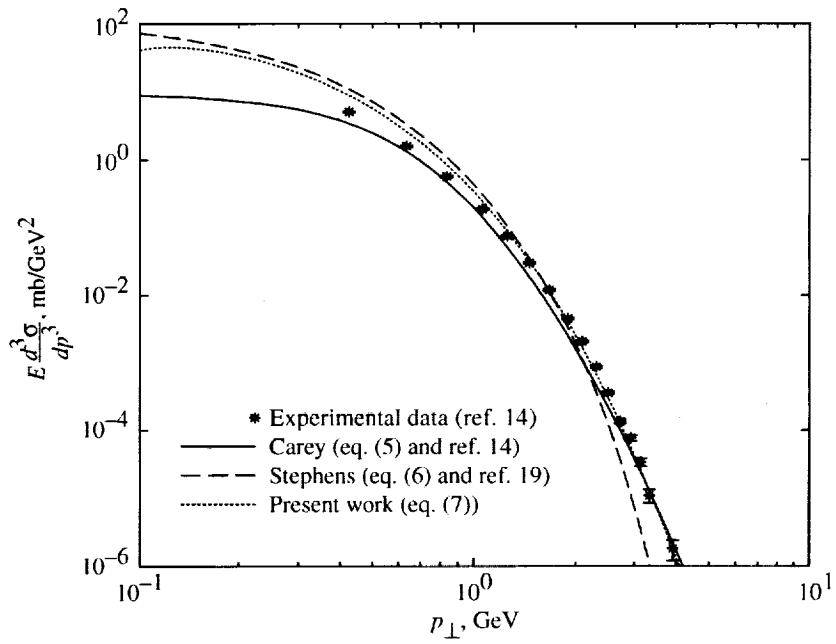


Figure 48. LIDCS plotted against transverse momentum for  $\pi^0$  production for  $E_{cm} = 19.4$  GeV and  $\theta^* = 87^\circ$  with data at  $85.1^\circ < \theta^* < 88.1^\circ$ .

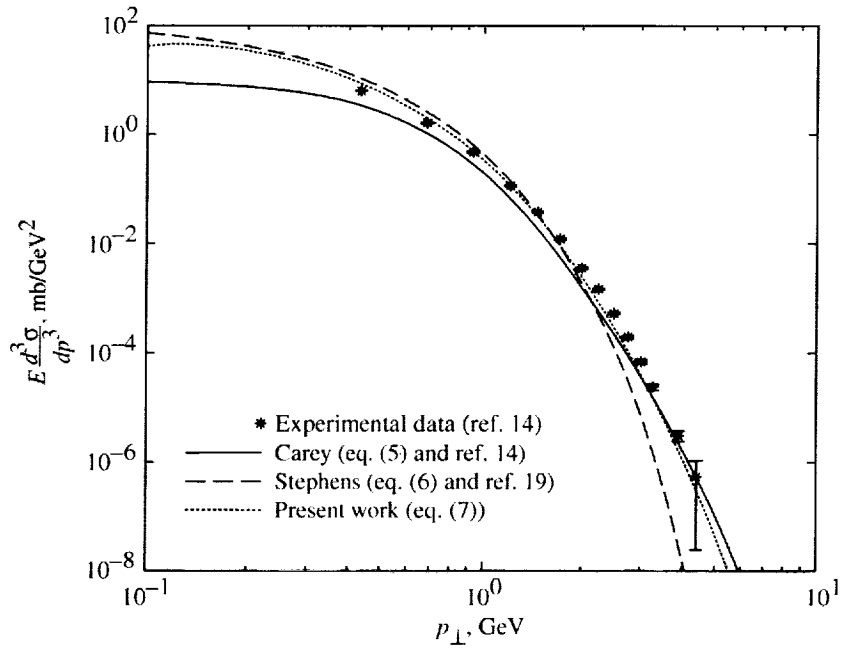


Figure 49. LIDCS plotted against transverse momentum for  $\pi^0$  production for  $E_{cm} = 19.8$  GeV and  $\theta^* = 75^\circ$  with data at  $73.2^\circ < \theta^* < 76.5^\circ$ .

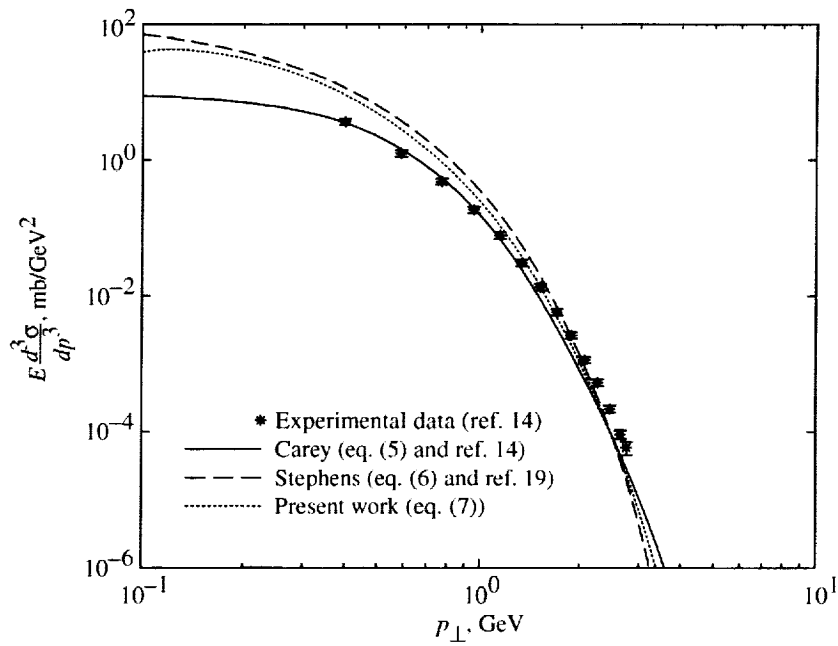


Figure 50. LIDCS plotted against transverse momentum for  $\pi^0$  production for  $E_{cm} = 20.6$  GeV and  $\theta^* = 36^\circ$  with data at  $36.3^\circ < \theta^* < 36.8^\circ$ .

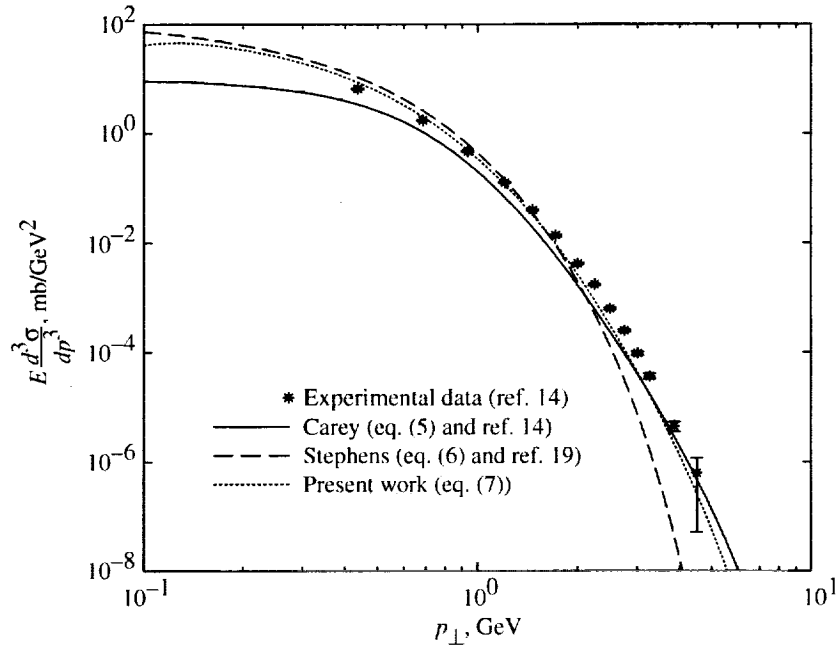


Figure 51. LIDCS plotted against transverse momentum for  $\pi^0$  production for  $E_{cm} = 21.0$  GeV and  $\theta^* = 73^\circ$  with data at  $70^\circ < \theta^* < 73.4^\circ$ .

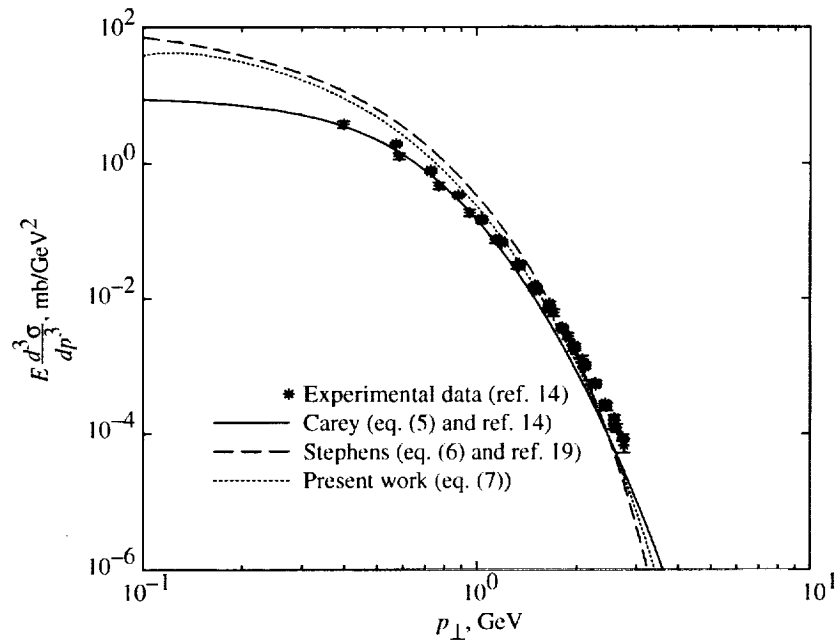


Figure 52. LIDCS plotted against transverse momentum for  $\pi^0$  production for  $E_{cm} = 21.7$  GeV and  $\theta^* = 34^\circ$  with data at  $33.2^\circ < \theta^* < 36.4^\circ$  and  $E_{cm} = 20.6$  and  $21.7$  GeV.

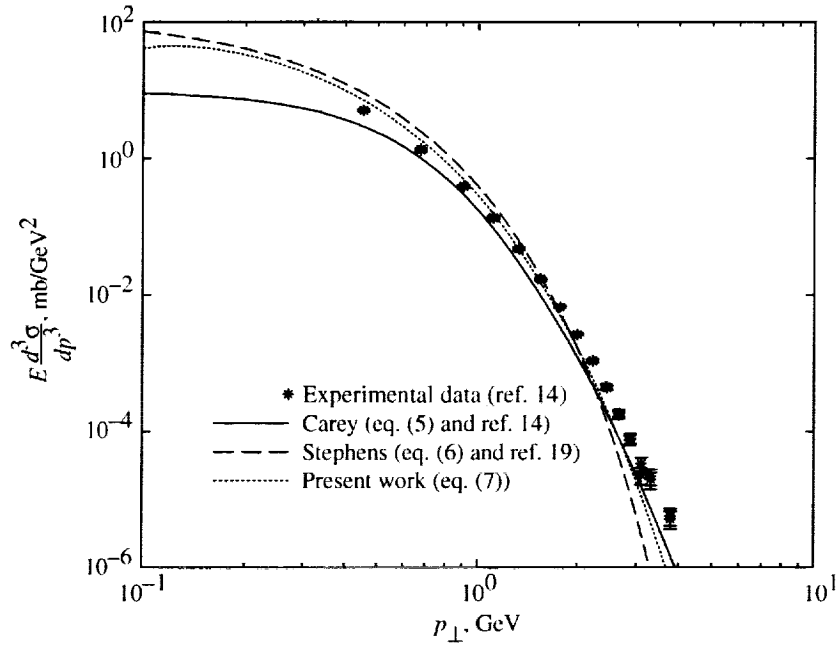


Figure 53. LIDCS plotted against transverse momentum for  $\pi^0$  production for  $E_{cm} = 21.7$  GeV and  $\theta^* = 45^\circ$  with data at  $43.7^\circ < \theta^* < 48.9^\circ$  and  $E_{cm} = 20.6$  and  $21.7$  GeV.

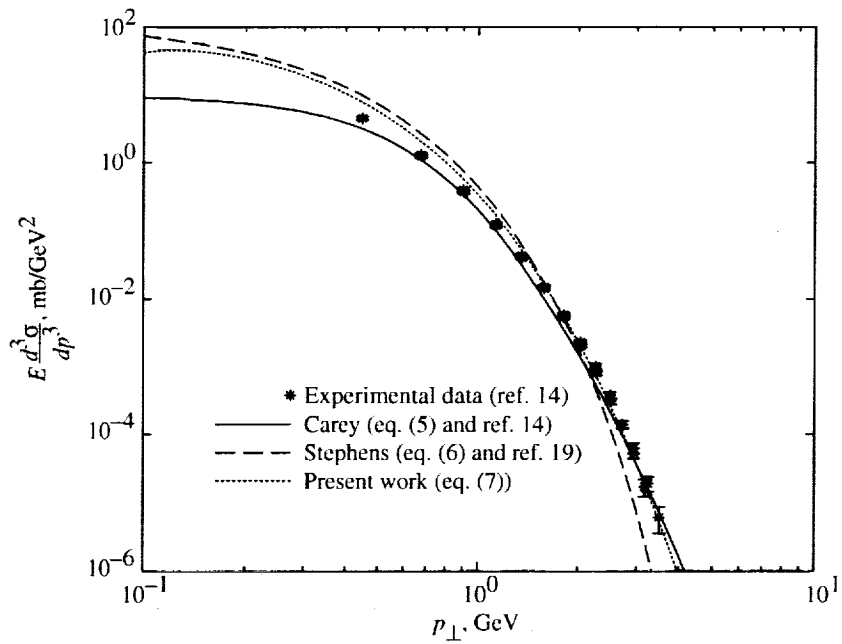


Figure 54. LIDCS plotted against transverse momentum for  $\pi^0$  production for  $E_{cm} = 21.7$  GeV and  $\theta^* = 60^\circ$  with data at  $57.4^\circ < \theta^* < 61.2^\circ$  and  $E_{cm} = 20.6$  and  $21.7$  GeV.

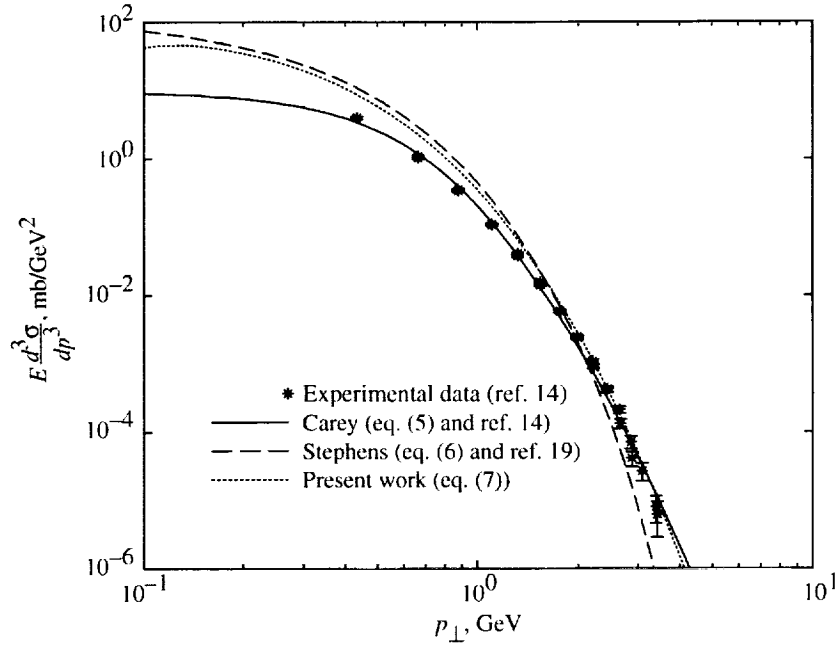


Figure 55. LIDCS plotted against transverse momentum for  $\pi^0$  production for  $E_{cm} = 21.7$  GeV and  $\theta^* = 74^\circ$  with data at  $70.9^\circ < \theta^* < 75.8^\circ$  and  $E_{cm} = 20.6$  and  $21.7$  GeV.

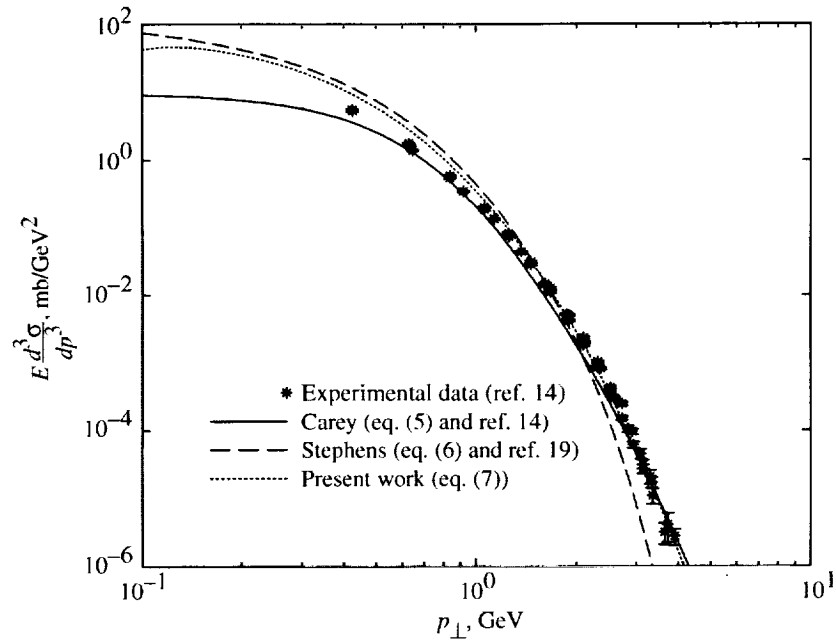


Figure 56. LIDCS plotted against transverse momentum for  $\pi^0$  production for  $E_{cm} = 21.7$  GeV and  $\theta^* = 80^\circ$  with data at  $78.5^\circ < \theta^* < 85.2^\circ$  and  $E_{cm} = 20.6$  and  $21.7$  GeV.

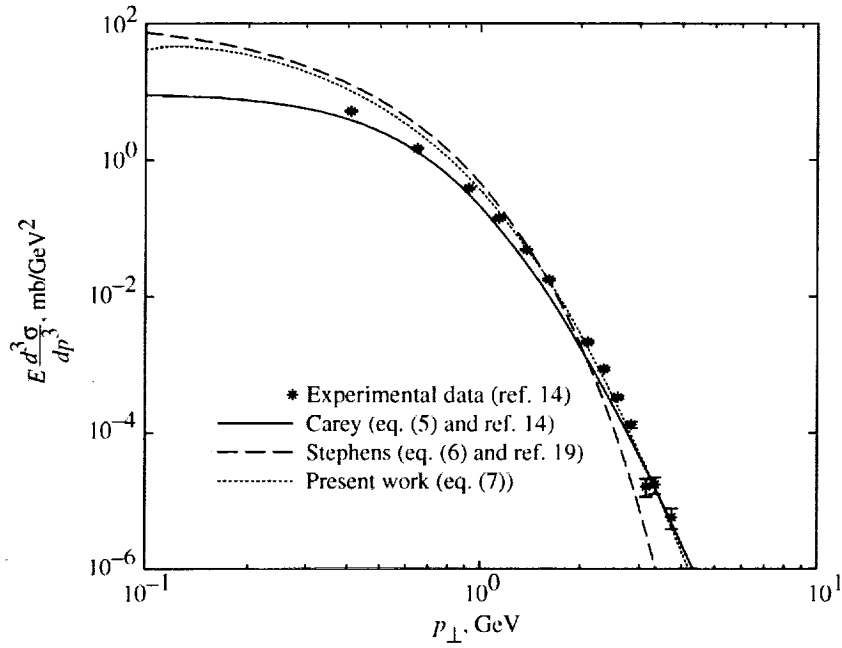


Figure 57. LIDCS plotted against transverse momentum for  $\pi^0$  production for  $E_{cm} = 21.7$  GeV and  $\theta^* = 86^\circ$  with data at  $85.5^\circ < \theta^* < 88.4^\circ$ .

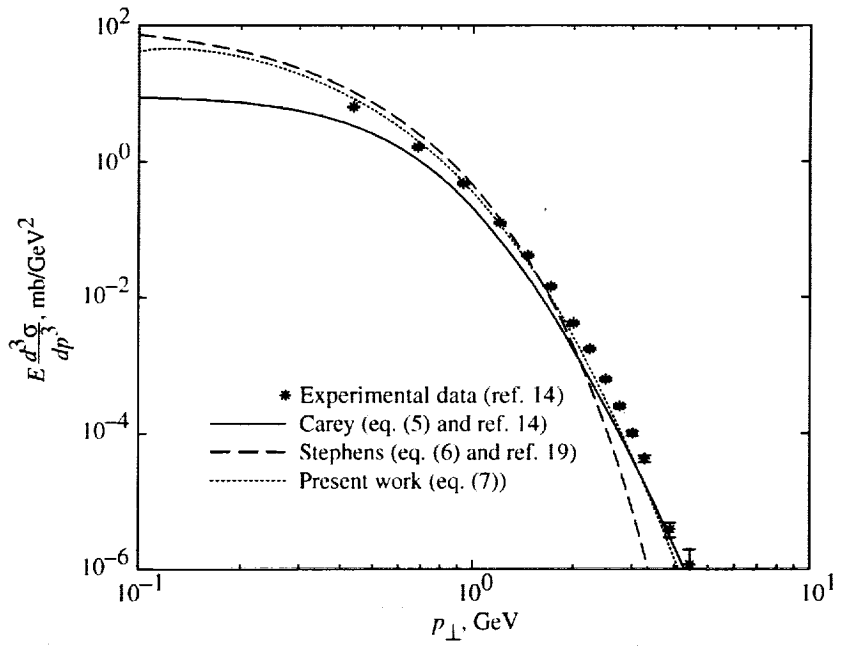


Figure 58. LIDCS plotted against transverse momentum for  $\pi^0$  production for  $E_{cm} = 22.1$  GeV and  $\theta^* = 70^\circ$  with data at  $67.2^\circ < \theta^* < 70.7^\circ$ .

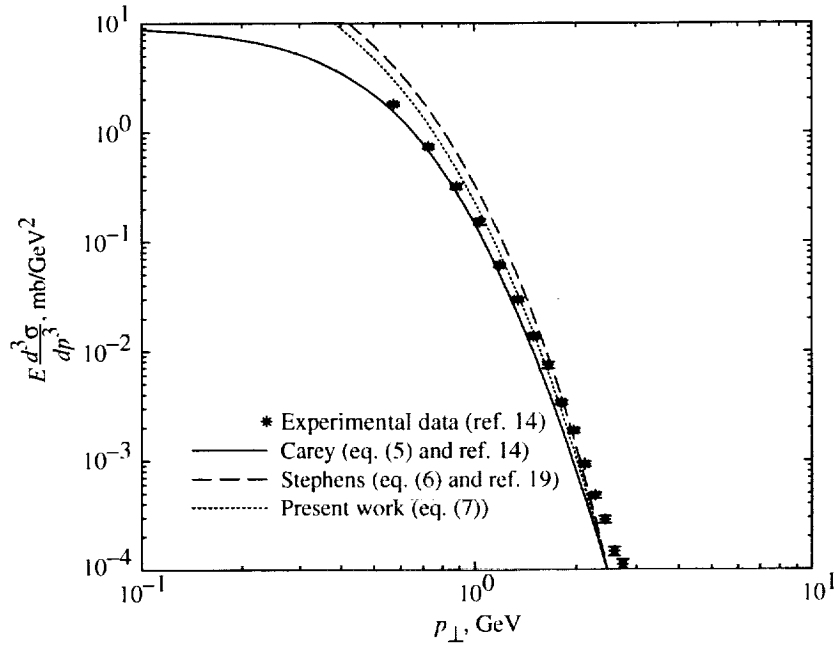


Figure 59. LIDCS plotted against transverse momentum for  $\pi^0$  production for  $E_{cm} = 22.8$  GeV and  $\theta^* = 32^\circ$  with data at  $31.7^\circ < \theta^* < 33.2^\circ$ .

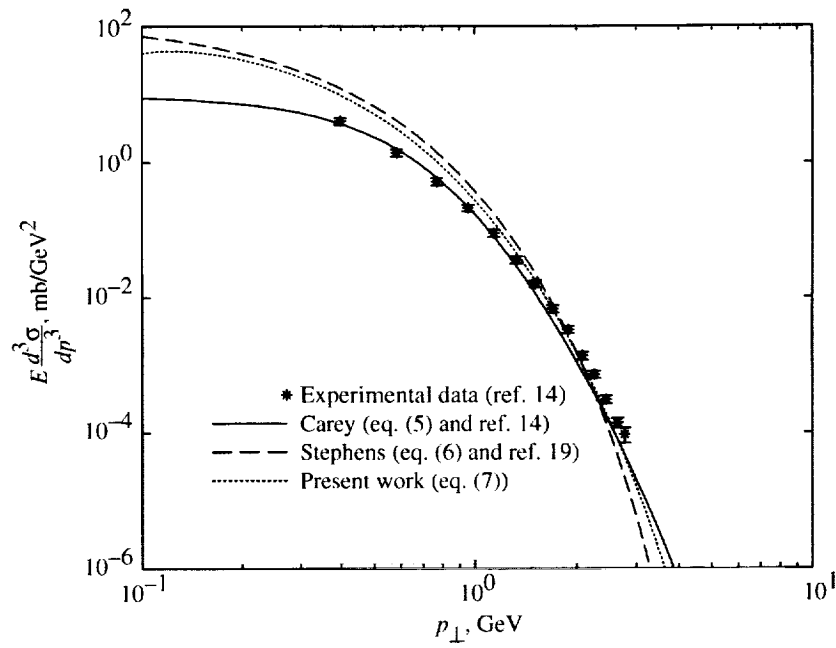


Figure 60. LIDCS plotted against transverse momentum for  $\pi^0$  production for  $E_{cm} = 22.8$  GeV and  $\theta^* = 40^\circ$  with data at  $39.9^\circ < \theta^* < 40.4^\circ$ .

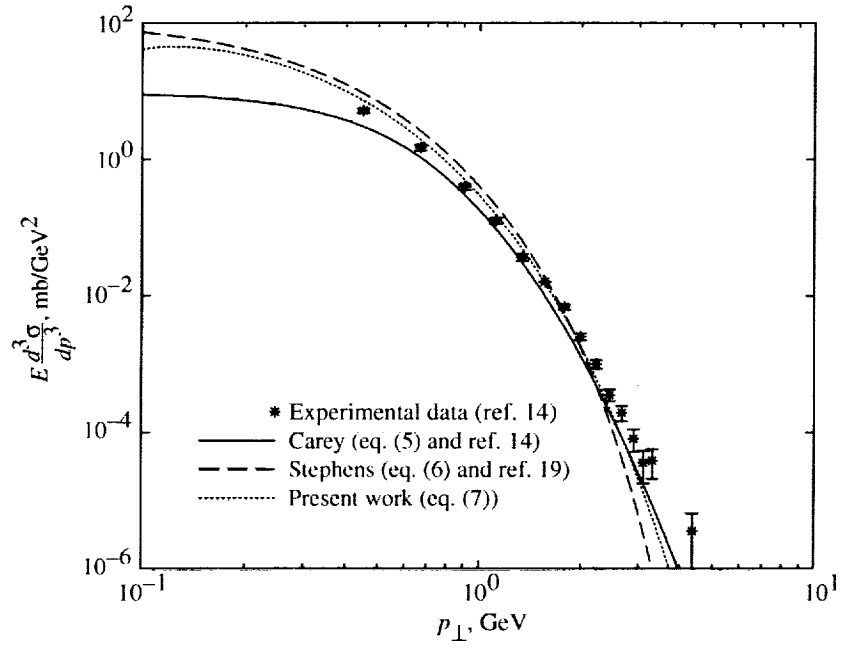


Figure 61. LIDCS plotted against transverse momentum for  $\pi^0$  production for  $E_{cm} = 22.8$  GeV and  $\theta^* = 44^\circ$  with data at  $41.8^\circ < \theta^* < 44.8^\circ$ .

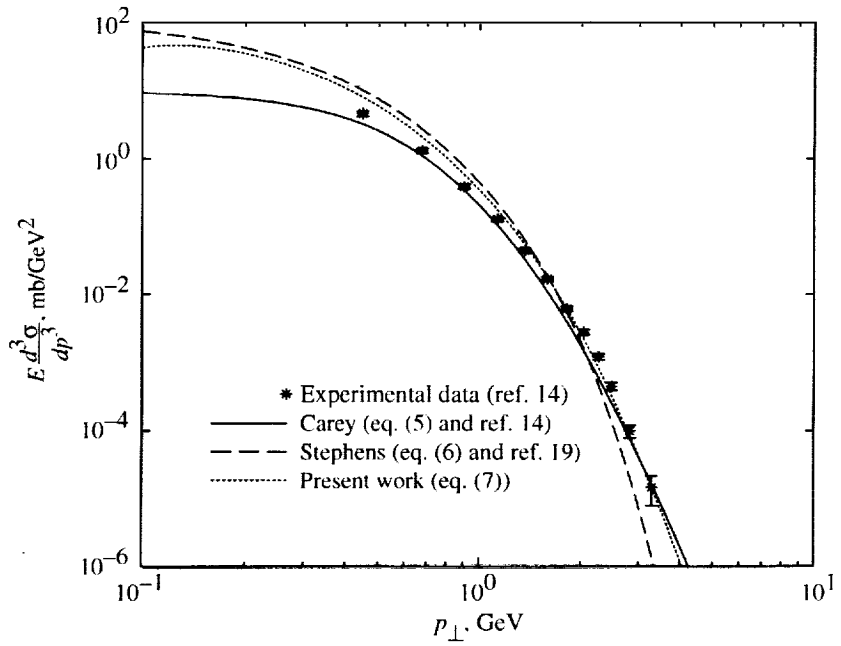


Figure 62. LIDCS plotted against transverse momentum for  $\pi^0$  production for  $E_{cm} = 22.8$  GeV and  $\theta^* = 63^\circ$  with data at  $62.4^\circ < \theta^* < 63.7^\circ$ .

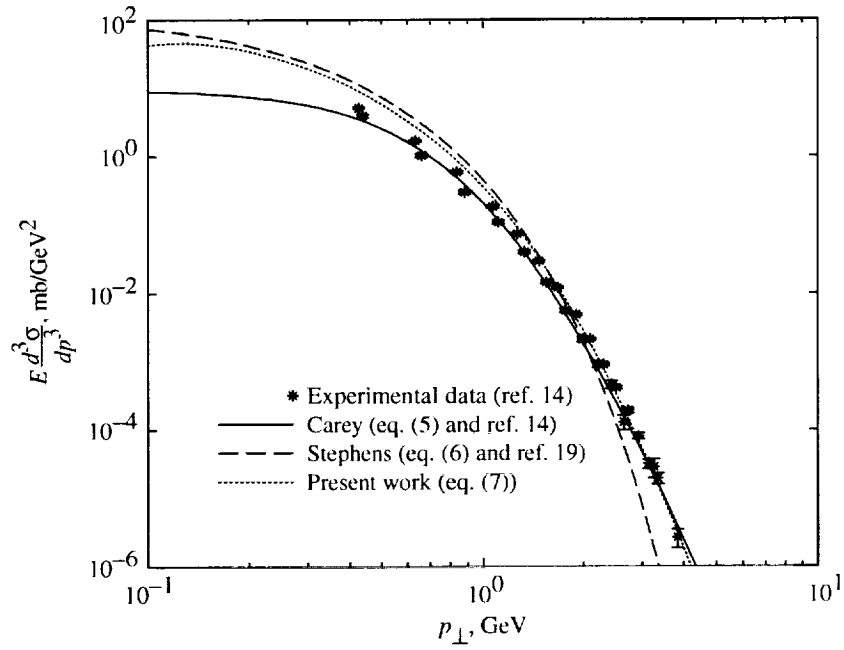


Figure 63. LIDCS plotted against transverse momentum for  $\pi^0$  production for  $E_{cm} = 22.8$  GeV and  $\theta^* = 77^\circ$  with data at  $76.4^\circ < \theta^* < 78.5^\circ$ .

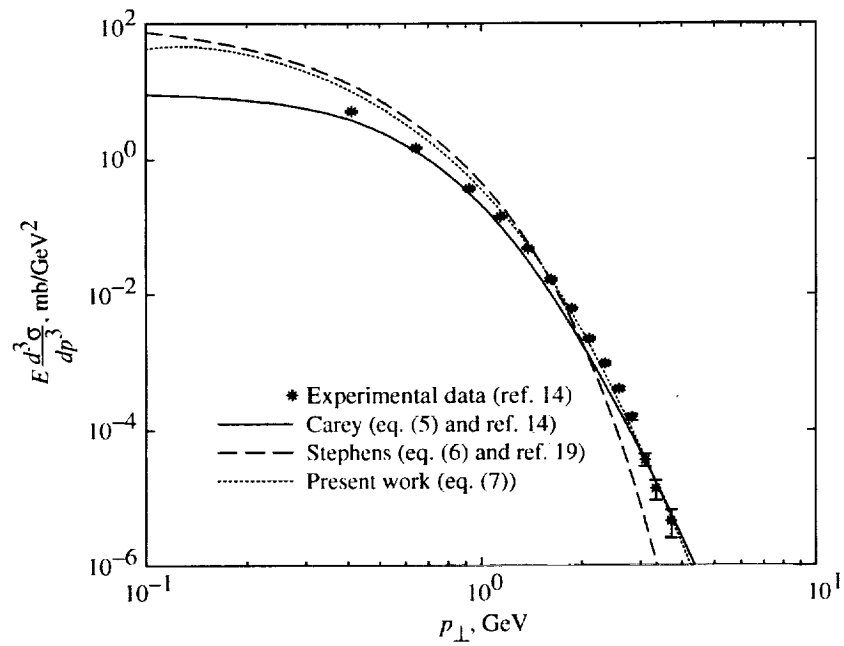


Figure 64. LIDCS plotted against transverse momentum for  $\pi^0$  production for  $E_{cm} = 22.8$  GeV and  $\theta^* = 89^\circ$  with data at  $88.2^\circ < \theta^* < 88.9^\circ$ .

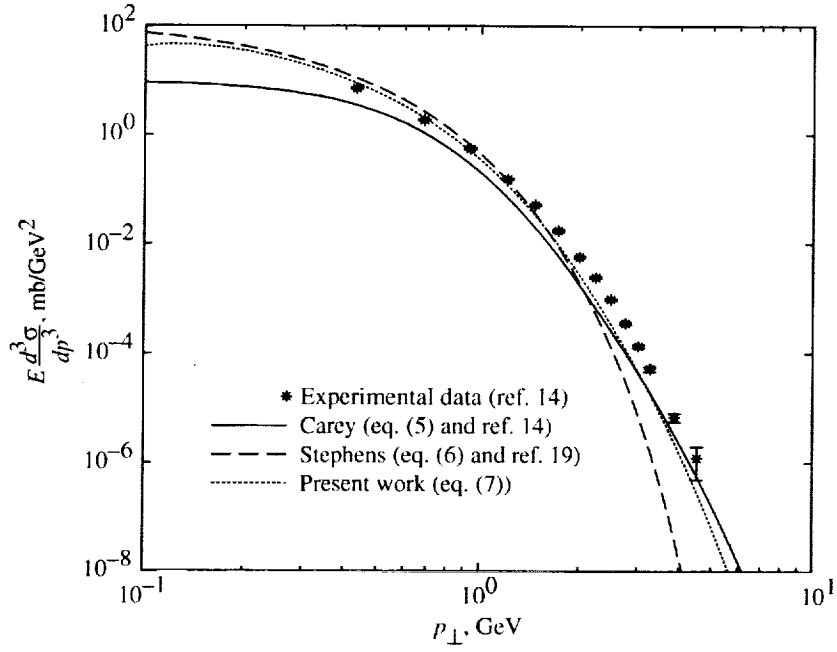


Figure 65. LIDCS plotted against transverse momentum for  $\pi^0$  production for  $E_{cm} = 23.1$  GeV and  $\theta^* = 67^\circ$  with data at  $64.7^\circ < \theta^* < 68.2^\circ$ .

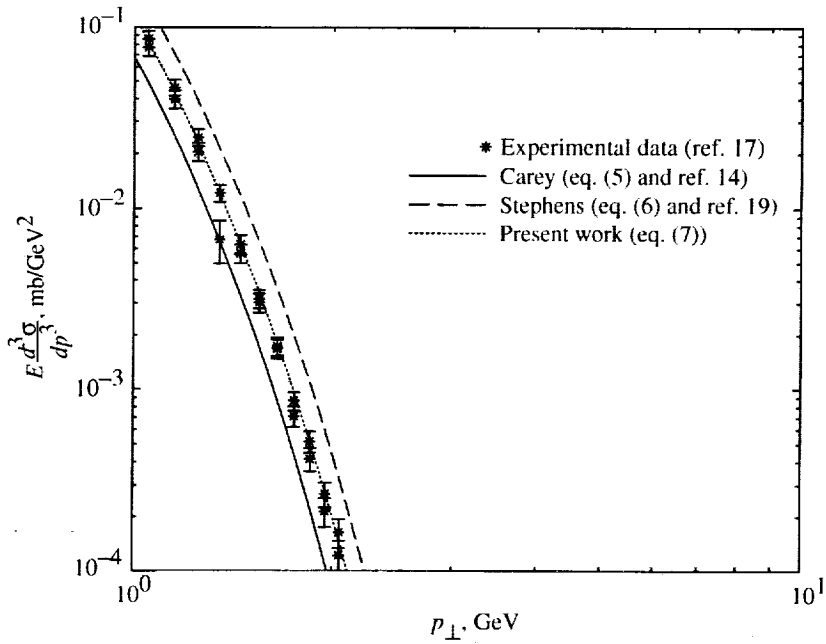


Figure 66. LIDCS plotted against transverse momentum for  $\pi^0$  production for  $E_{cm} = 23.3$  GeV and  $\theta^* = 16^\circ$  with data at  $\theta^* = 15^\circ$  and  $17.5^\circ$ .

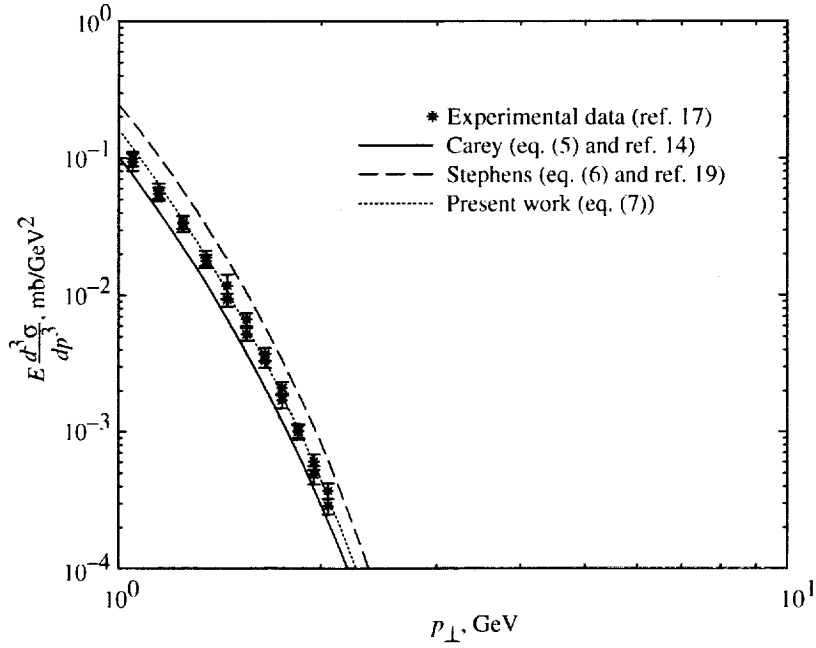


Figure 67. LIDCS plotted against transverse momentum for  $\pi^0$  production for  $E_{cm} = 23.3$  GeV and  $\theta^* = 21^\circ$  with data at  $\theta^* = 20^\circ$  and  $22^\circ$ .

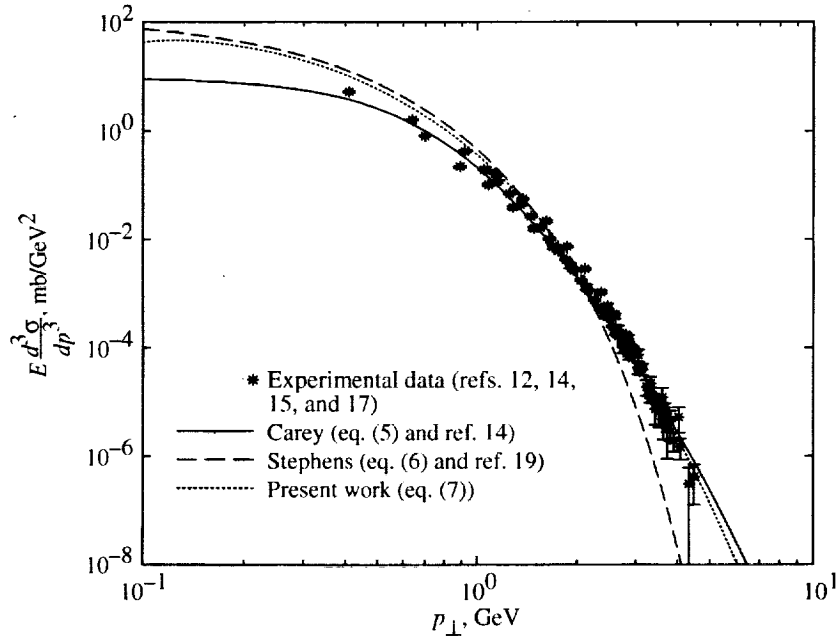


Figure 68. LIDCS plotted against transverse momentum for  $\pi^0$  production for  $E_{cm} = 23.5$  GeV and  $\theta^* = 90^\circ$  with data at  $86.1^\circ < \theta^* < 90^\circ$  and  $23.5 < E_{cm} < 23.8$  GeV.

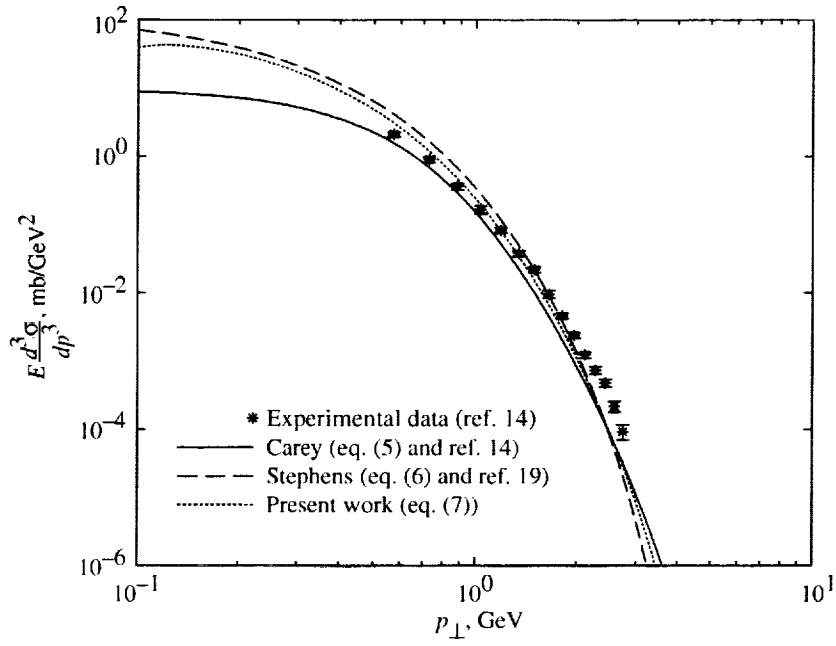


Figure 69. LIDCS plotted against transverse momentum for  $\pi^0$  production for  $E_{cm} = 23.8$  GeV and  $\theta^* = 31^\circ$  with data at  $30.4^\circ < \theta^* < 31.9^\circ$ .

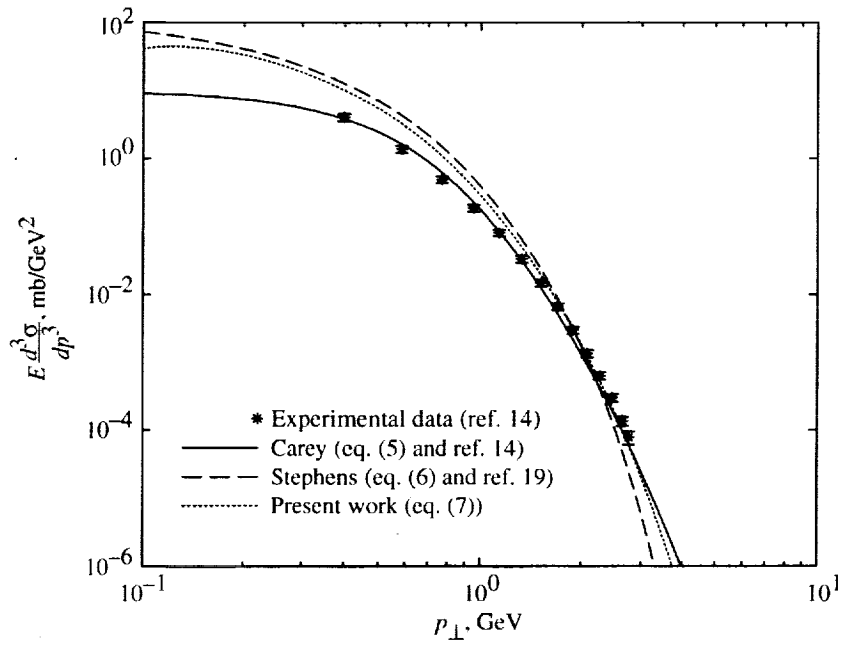


Figure 70. LIDCS plotted against transverse momentum for  $\pi^0$  production for  $E_{cm} = 23.8$  GeV and  $\theta^* = 42^\circ$  with data at  $41.5^\circ < \theta^* < 42.1^\circ$ .

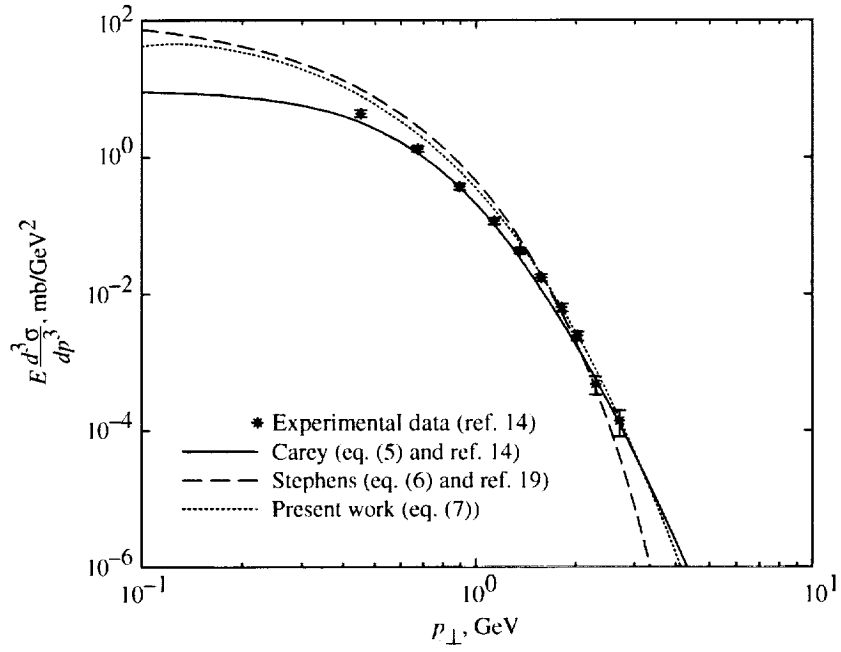


Figure 71. LIDCS plotted against transverse momentum for  $\pi^0$  production for  $E_{cm} = 23.8$  GeV and  $\theta^* = 65^\circ$  with data at  $64.6^\circ < \theta^* < 66.0^\circ$ .

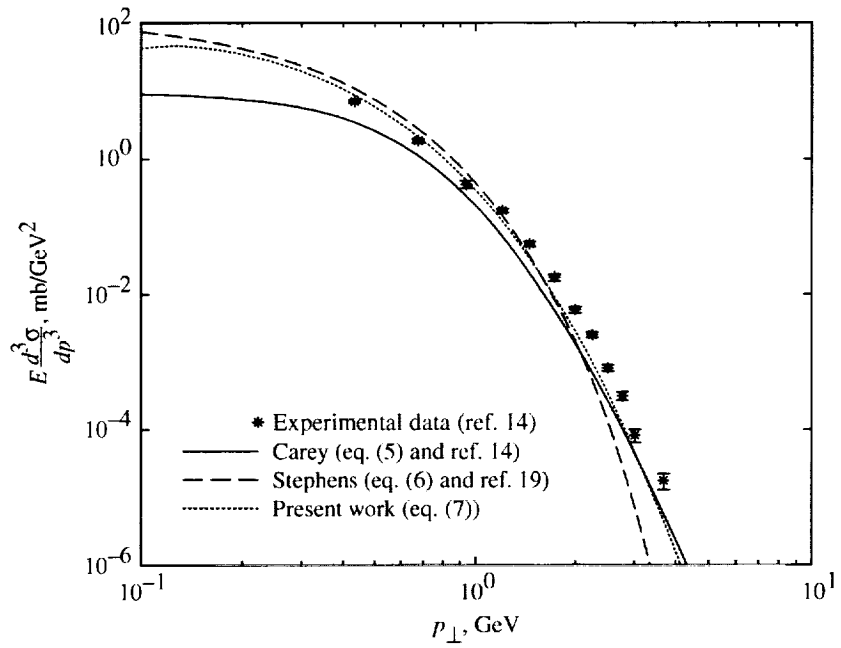


Figure 72. LIDCS plotted against transverse momentum for  $\pi^0$  production for  $E_{cm} = 23.8$  GeV and  $\theta^* = 66^\circ$  with data at  $63.2^\circ < \theta^* < 66.7^\circ$ .

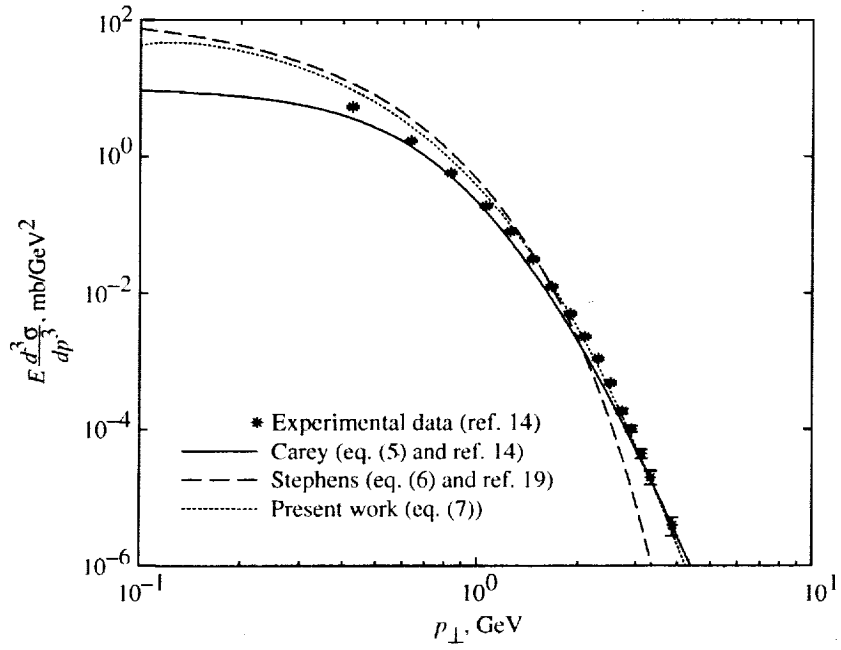


Figure 73. LIDCS plotted against transverse momentum for  $\pi^0$  production for  $E_{cm} = 23.8$  GeV and  $\theta^* = 76^\circ$  with data at  $73.2^\circ < \theta^* < 76.6^\circ$ .

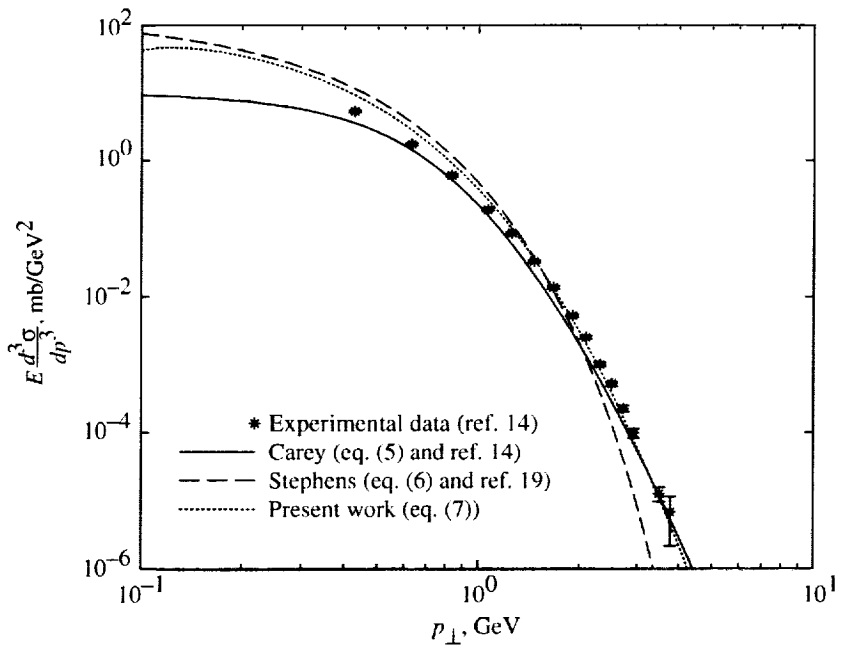


Figure 74. LIDCS plotted against transverse momentum for  $\pi^0$  production for  $E_{cm} = 24.8$  GeV and  $\theta^* = 73^\circ$  with data at  $71.0^\circ < \theta^* < 74.4^\circ$ .

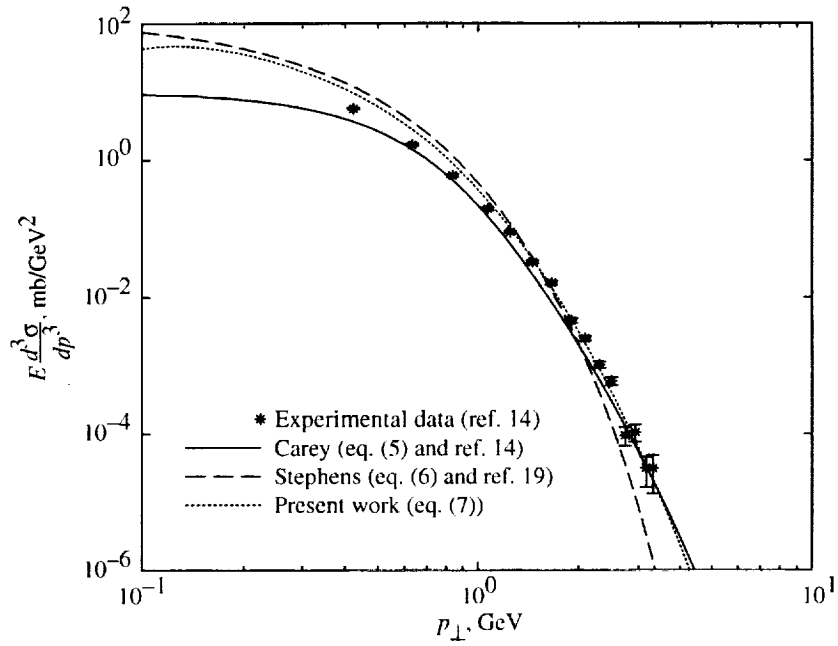


Figure 75. LIDCS plotted against transverse momentum for  $\pi^0$  production for  $E_{cm} = 25.7$  GeV and  $\theta^* = 71^\circ$  with data at  $68.8^\circ < \theta^* < 72.4^\circ$ .

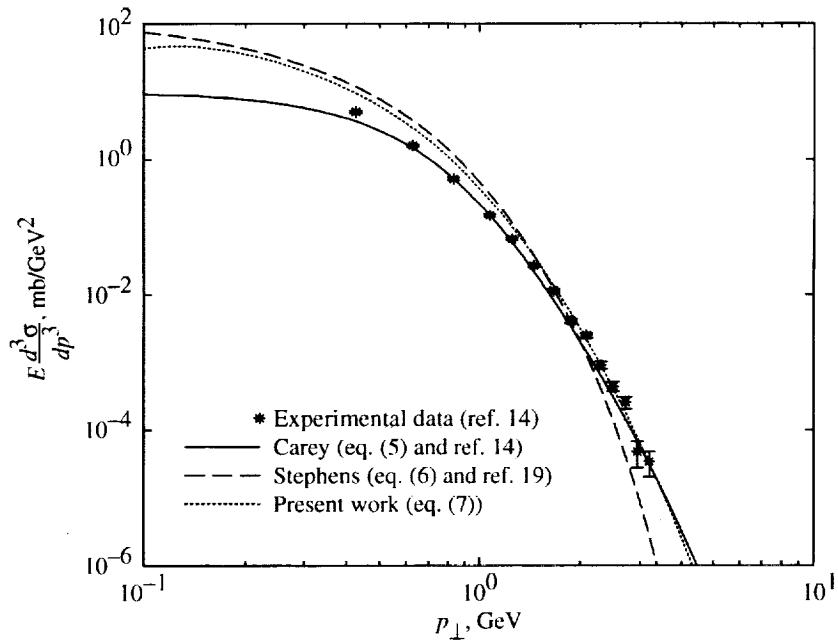


Figure 76. LIDCS plotted against transverse momentum for  $\pi^0$  production for  $E_{cm} = 26.6$  GeV and  $\theta^* = 70^\circ$  with data at  $66.9^\circ < \theta^* < 70.5^\circ$ .

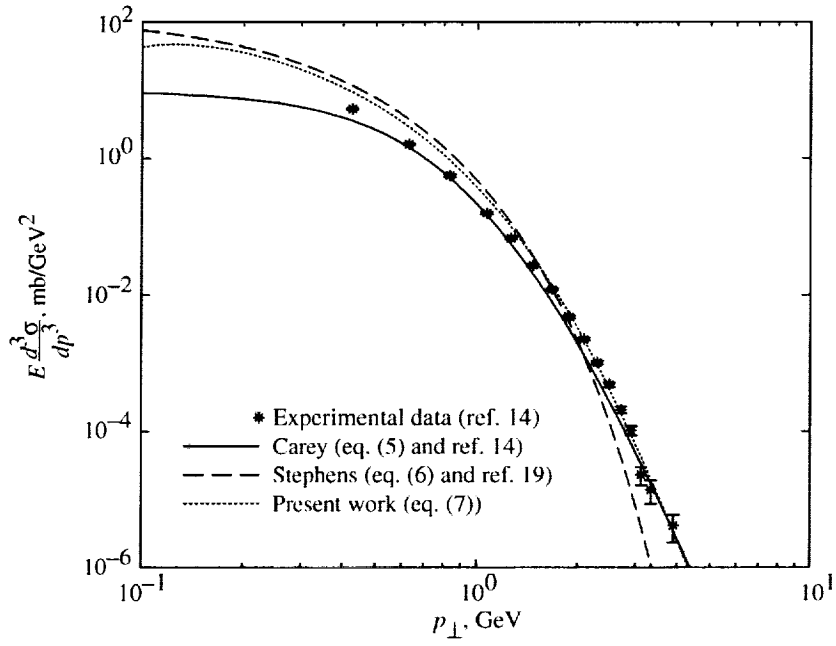


Figure 77. LIDCS plotted against transverse momentum for  $\pi^0$  production for  $E_{cm} = 27.4$  GeV and  $\theta^* = 67^\circ$  with data at  $65.2^\circ < \theta^* < 68.8^\circ$ .

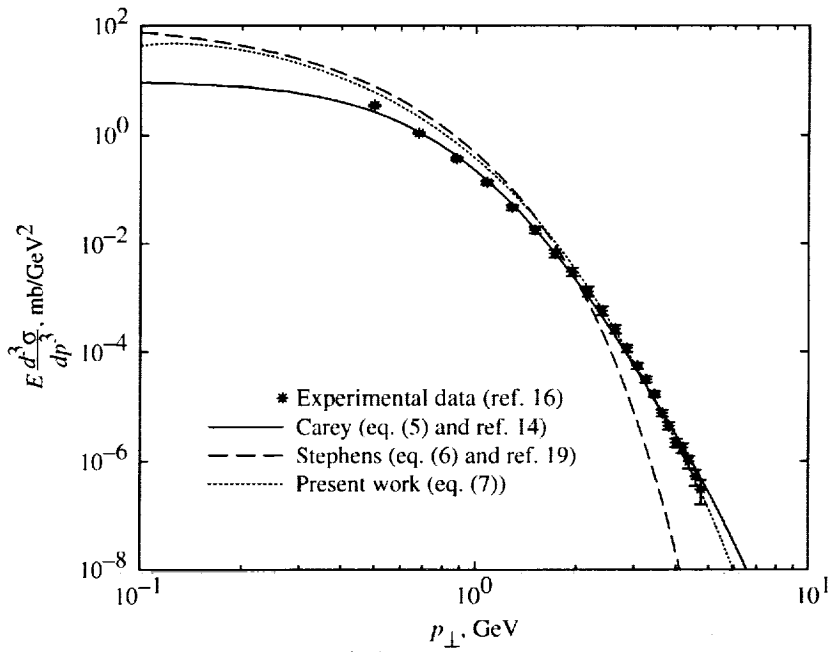


Figure 78. LIDCS plotted against transverse momentum for  $\pi^0$  production for  $E_{cm} = 30.8$  GeV and  $\theta^* = 53^\circ$ .

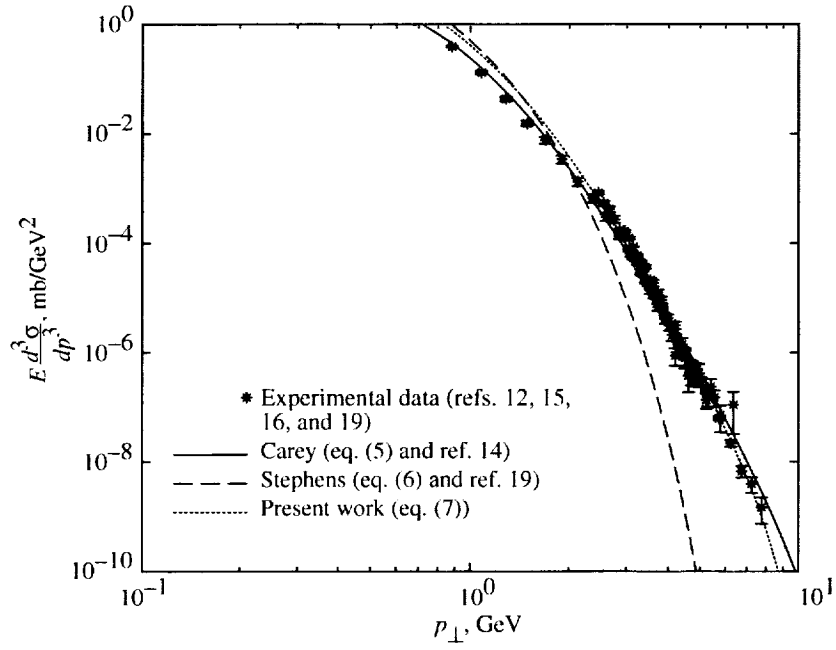


Figure 79. LIDCS plotted against transverse momentum for  $\pi^0$  production for  $E_{cm} = 30.8$  GeV and  $\theta^* = 90^\circ$  with data at  $30.6 < E_{cm} < 31$  GeV.

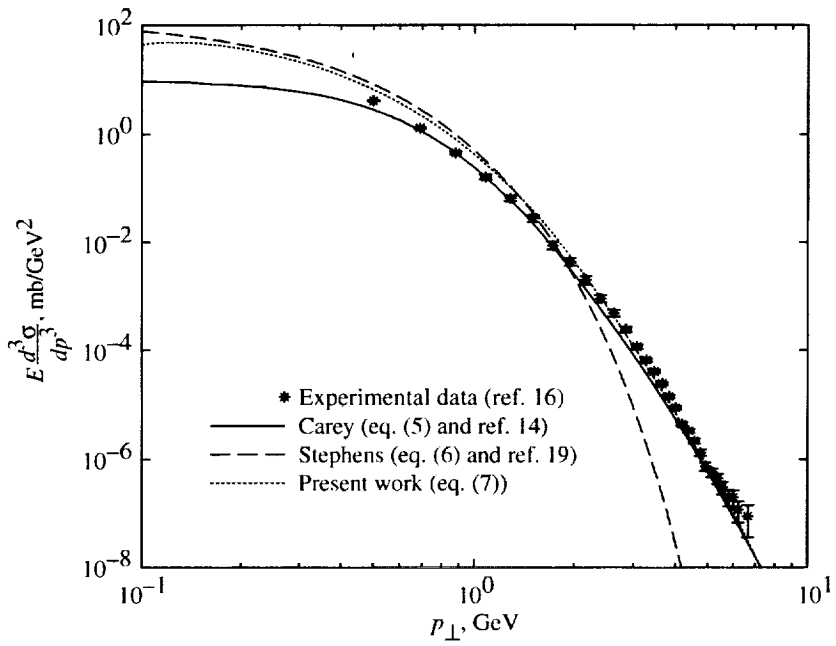


Figure 80. LIDCS plotted against transverse momentum for  $\pi^0$  production for  $E_{cm} = 45.1$  GeV and  $\theta^* = 53^\circ$ .

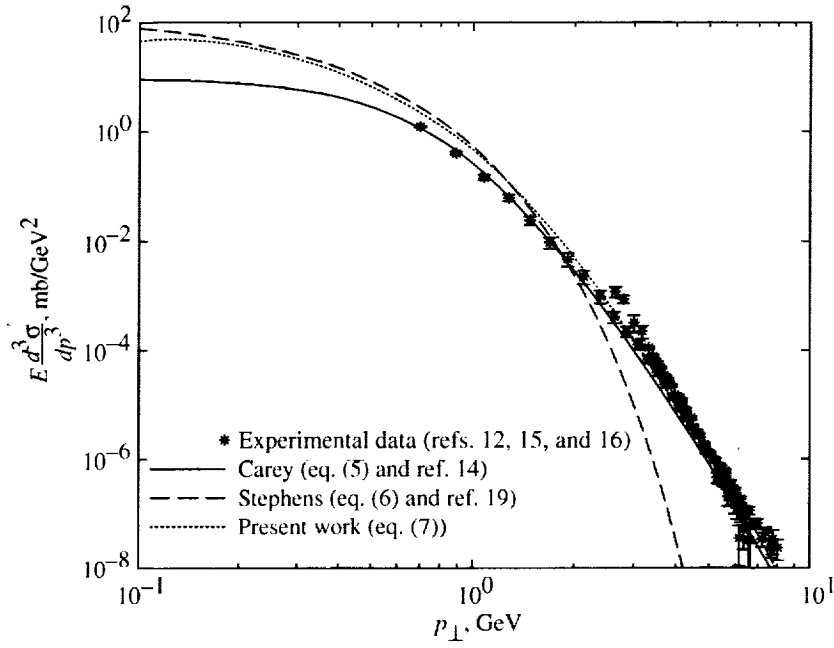


Figure 81. LIDCS plotted against transverse momentum for  $\pi^0$  production for  $E_{cm} = 45$  GeV and  $\theta^* = 90^\circ$  with data at  $E_{cm} = 44.8$  and  $45.1$  GeV.

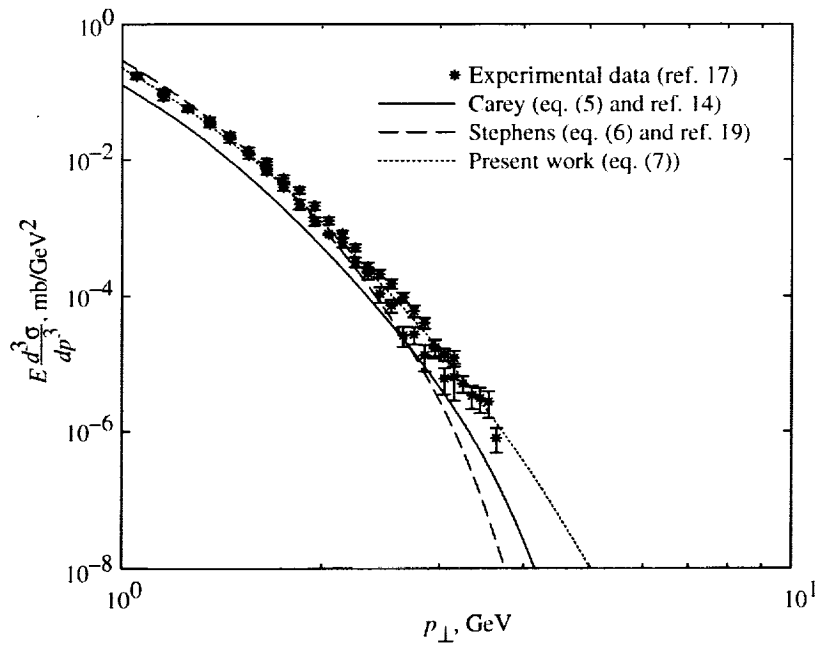


Figure 82. LIDCS plotted against transverse momentum for  $\pi^0$  production for  $E_{cm} = 52.8$  GeV and  $\theta^* = 11^\circ$  with data at  $\theta^* = 10^\circ$  and  $11^\circ$ .

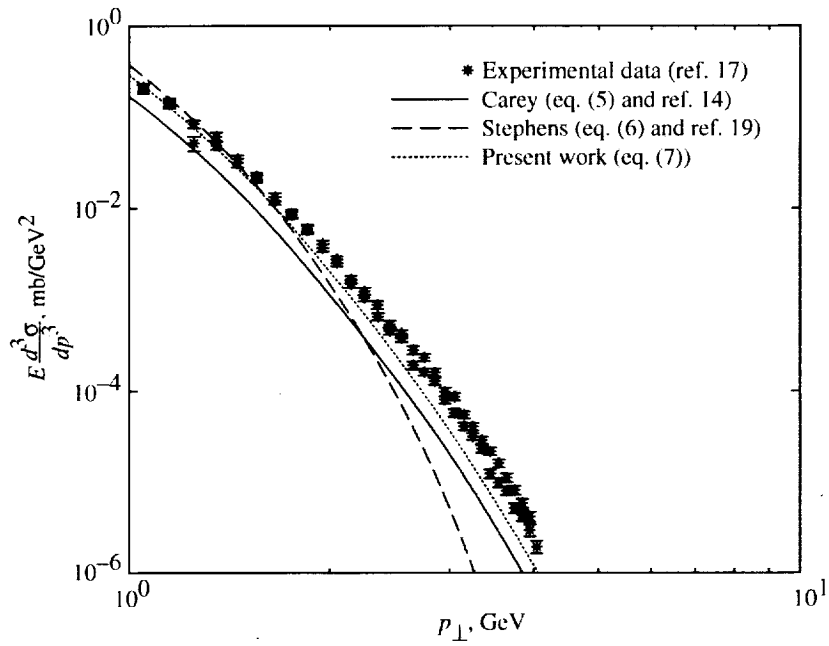


Figure 83. LIDCS plotted against transverse momentum for  $\pi^0$  production for  $E_{cm} = 52.8$  GeV and  $\theta^* = 16^\circ$  with data at  $\theta^* = 15^\circ$  and  $17.5^\circ$ .

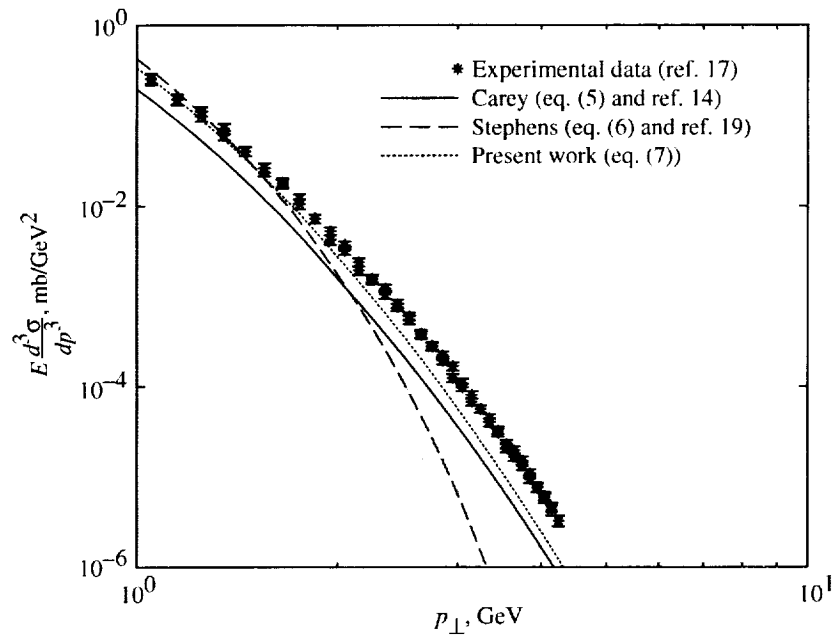


Figure 84. LIDCS plotted against transverse momentum for  $\pi^0$  production for  $E_{cm} = 52.8$  GeV and  $\theta^* = 21^\circ$  with data at  $\theta^* = 20^\circ$  and  $22^\circ$ .

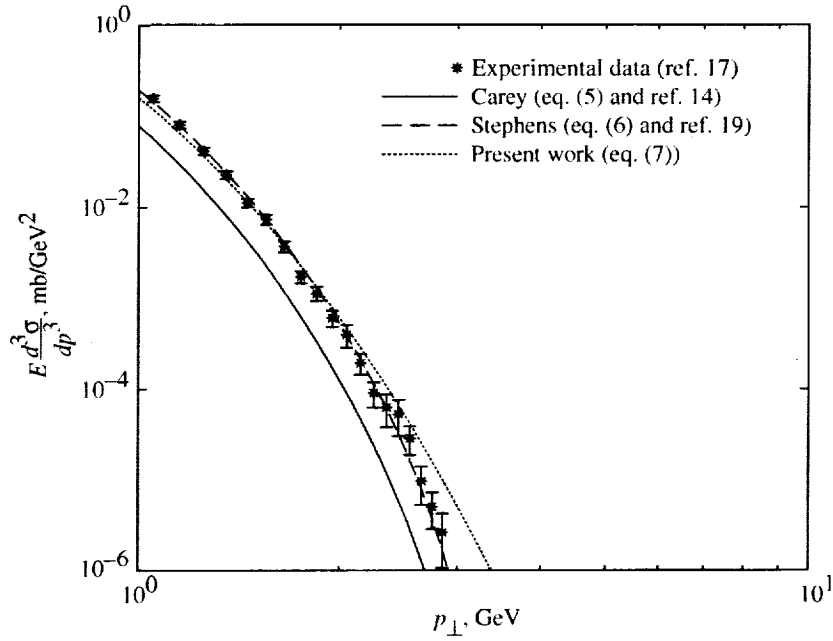


Figure 85. LIDCS plotted against transverse momentum for  $\pi^0$  production for  $E_{cm} = 52.8$  GeV and  $\theta^* = 7.5^\circ$ .

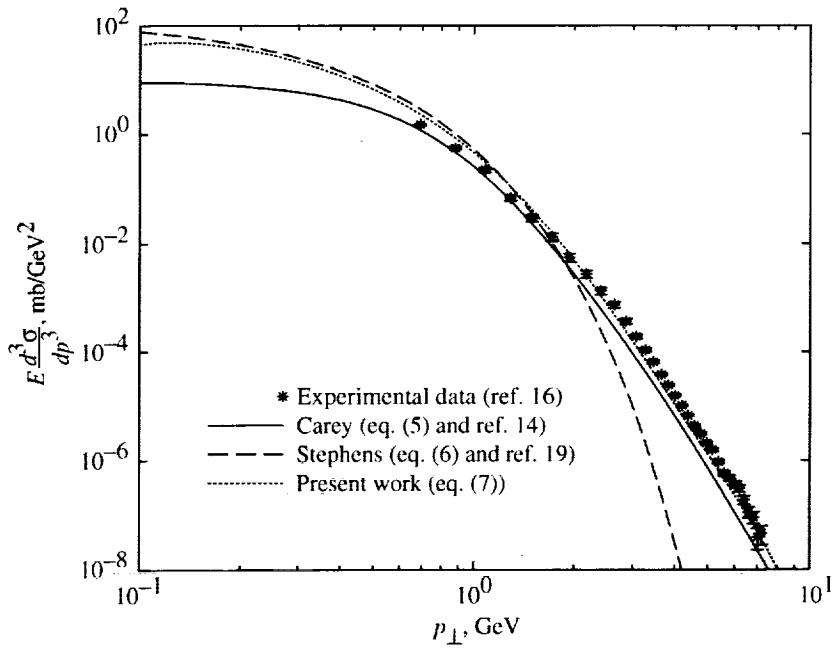


Figure 86. LIDCS plotted against transverse momentum for  $\pi^0$  production for  $E_{cm} = 53.2$  GeV and  $\theta^* = 53^\circ$ .

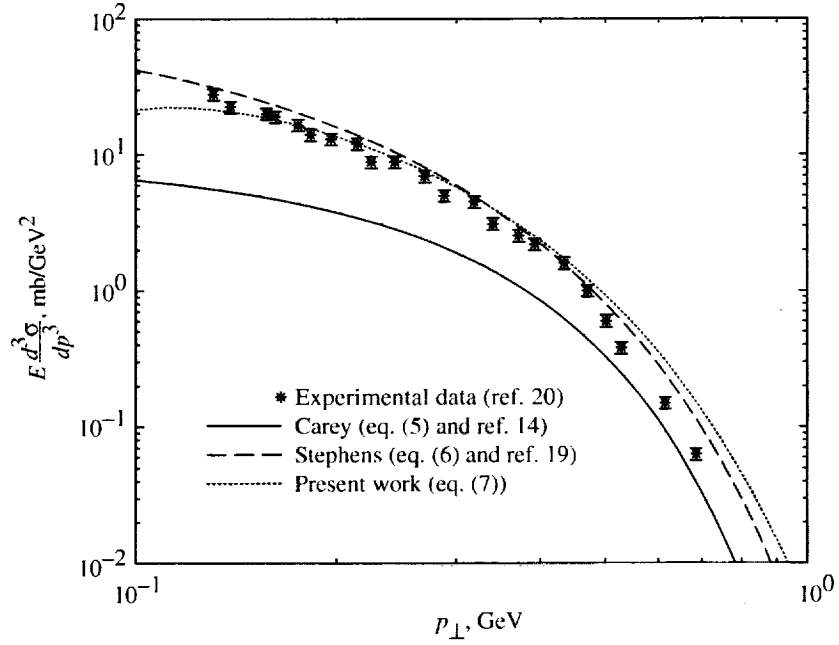


Figure 87. LIDCS plotted against transverse momentum for  $\pi^0$  production for  $E_{cm} = 7$  GeV and  $\theta^* = 21^\circ$  with data at  $20^\circ < \theta^* < 22^\circ$ .

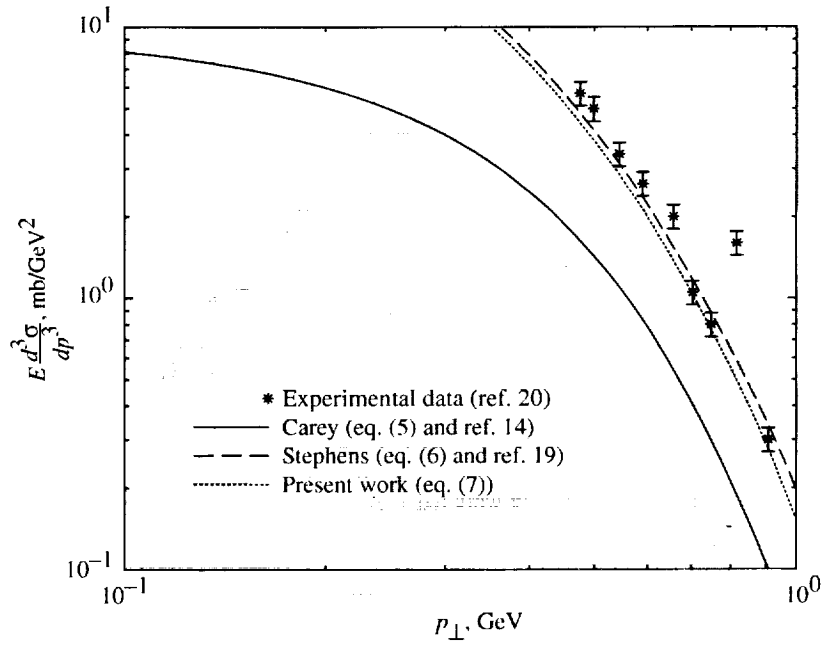


Figure 88. LIDCS plotted against transverse momentum for  $\pi^0$  production for  $E_{cm} = 7$  GeV and  $\theta^* = 60^\circ$  with data at  $58^\circ < \theta^* < 61^\circ$ .

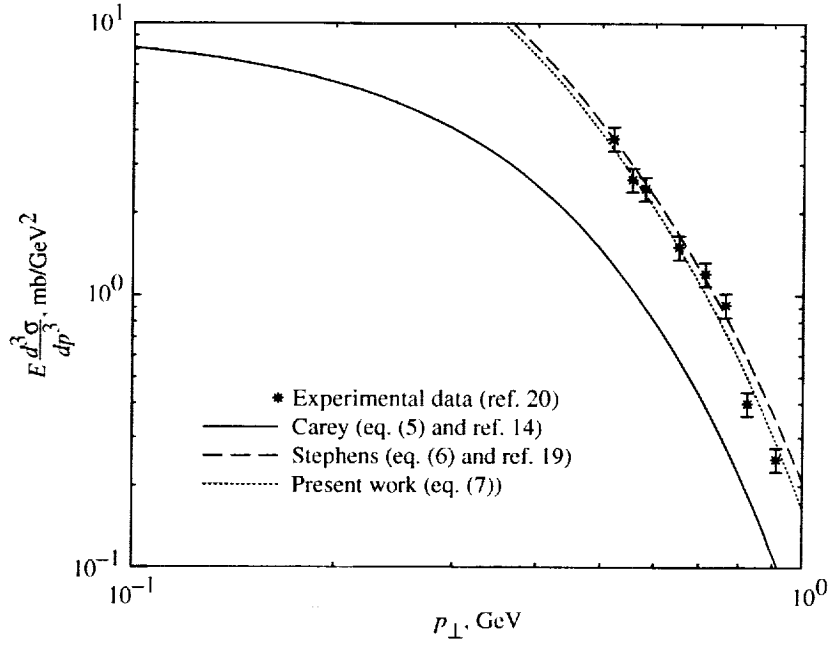


Figure 89. LIDCS plotted against transverse momentum for  $\pi^0$  production for  $E_{cm} = 7$  GeV and  $\theta^* = 63^\circ$  with data at  $63^\circ < \theta^* < 64^\circ$ .

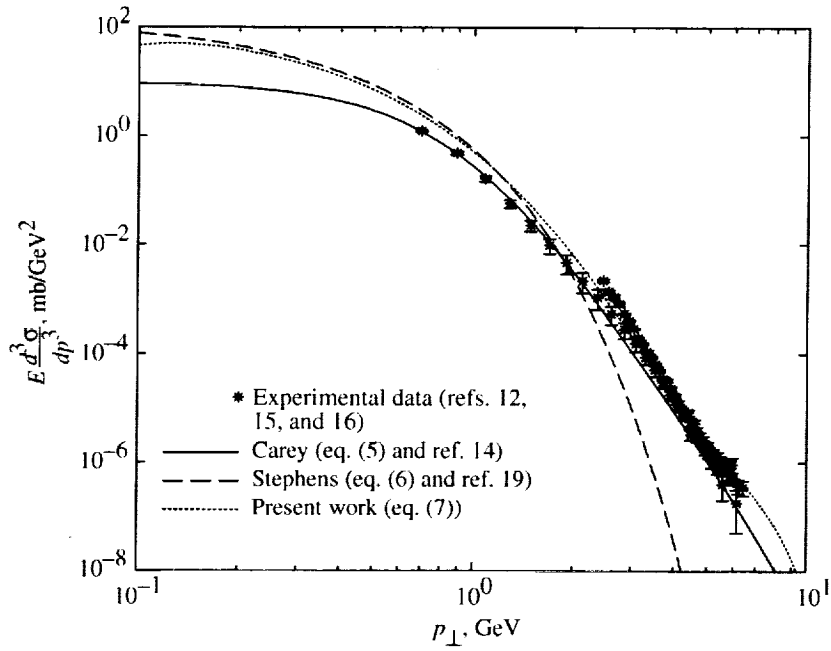


Figure 90. LIDCS plotted against transverse momentum for  $\pi^0$  production for  $E_{cm} = 62.6$  GeV and  $\theta^* = 90^\circ$  with data at  $E_{cm} = 62.4$  and  $62.9$  GeV.

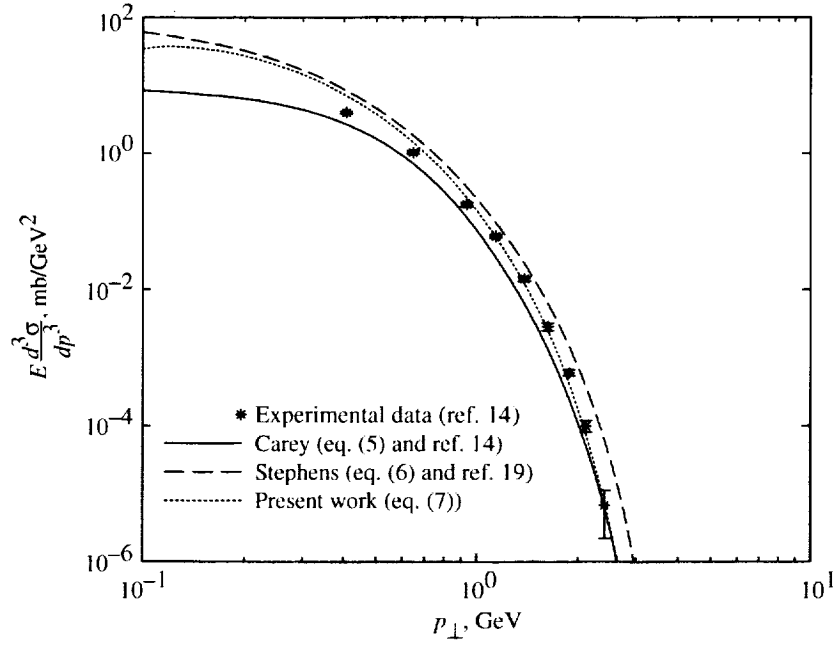


Figure 91. LIDCS plotted against transverse momentum for  $\pi^0$  production for  $E_{cm} = 9.8$  GeV and  $\theta^* = 45^\circ$  with data at  $44.9^\circ < \theta^* < 45.6^\circ$ .

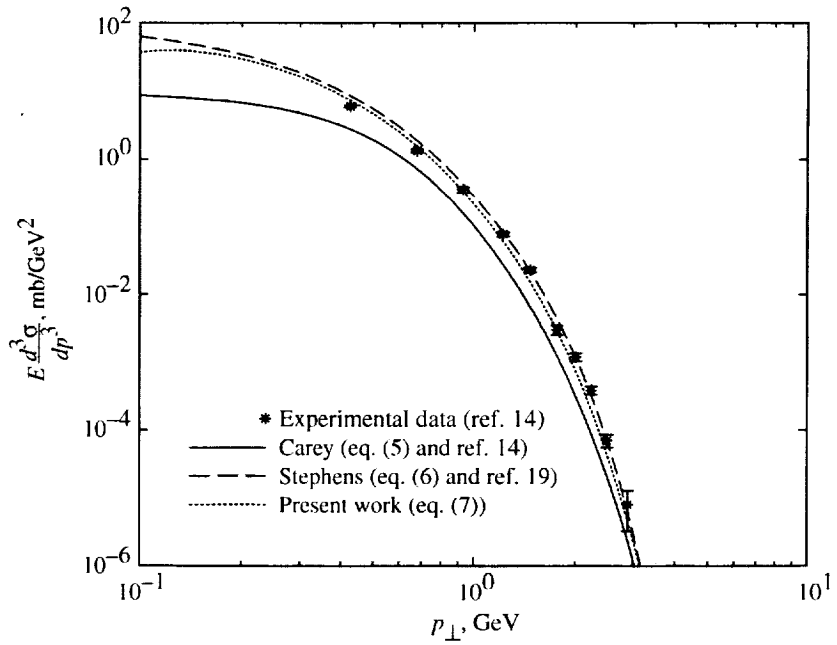


Figure 92. LIDCS plotted against transverse momentum for  $\pi^0$  production for  $E_{cm} = 9.8$  GeV and  $\theta^* = 64^\circ$  with data at  $63.6^\circ < \theta^* < 65.1^\circ$ .

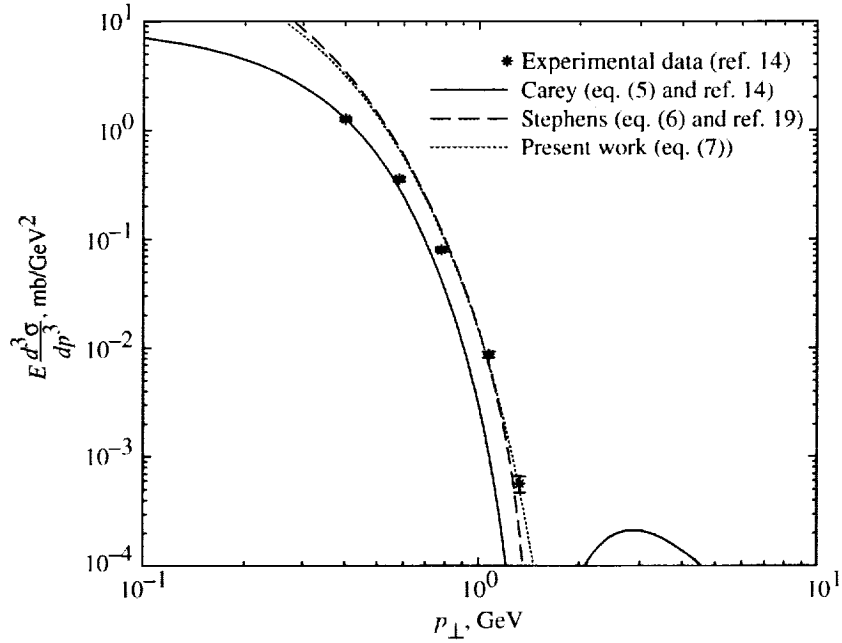


Figure 93. LIDCS plotted against transverse momentum for  $\pi^0$  production for  $E_{cm} = 9.8$  GeV and  $\theta^* = 18^\circ$  with data at  $17.6^\circ < \theta^* < 17.7^\circ$ .

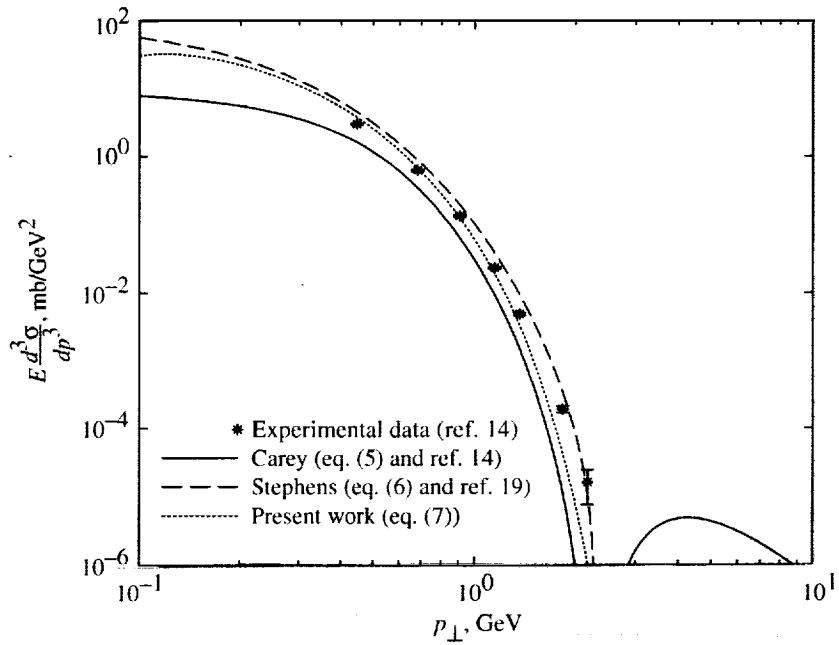


Figure 94. LIDCS plotted against transverse momentum for  $\pi^0$  production for  $E_{cm} = 9.8$  GeV and  $\theta^* = 29^\circ$  with data at  $28.9^\circ < \theta^* < 29.2^\circ$ .

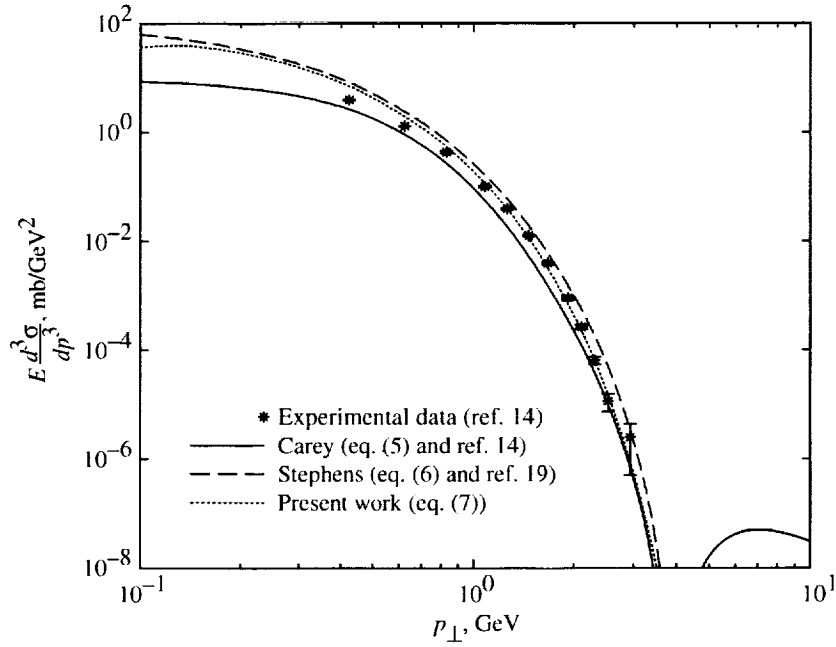


Figure 95. LIDCS plotted against transverse momentum for  $\pi^0$  production for  $E_{cm} = 9.8$  GeV and  $\theta^* = 55^\circ$  with data at  $54.6^\circ < \theta^* < 55.7^\circ$ .

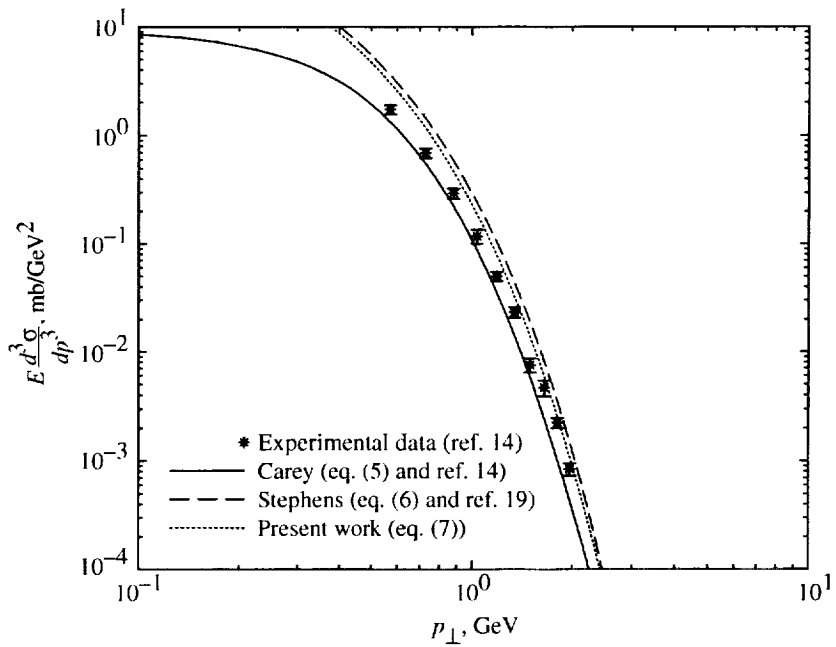


Figure 96. LIDCS plotted against transverse momentum for  $\pi^0$  production for  $E_{cm} = 9.8$  GeV and  $\theta^* = 69^\circ$  with data at  $68.0^\circ < \theta^* < 69.9^\circ$ .

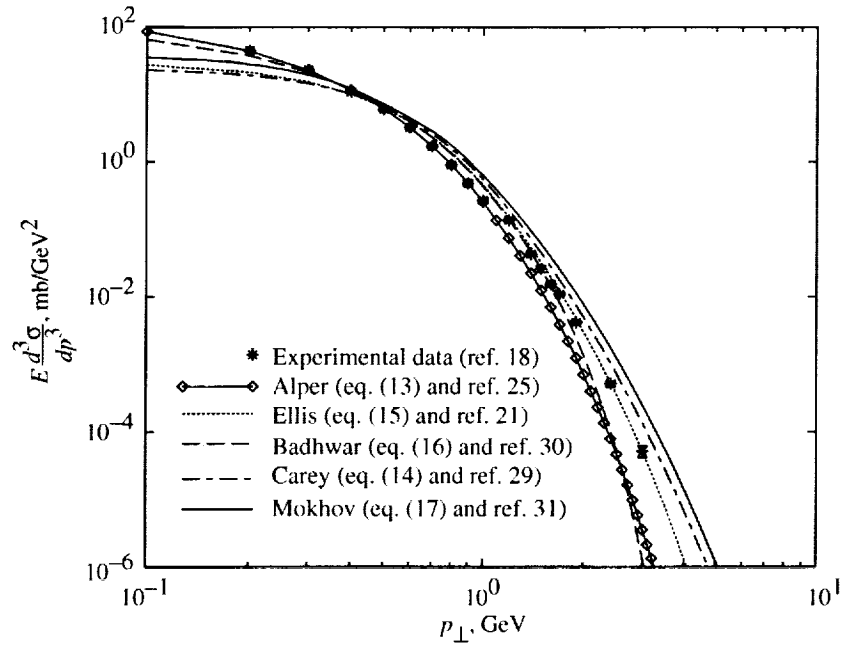


Figure 97. LIDCS plotted against transverse momentum for  $\pi^-$  production for  $E_{cm} = 23$  GeV and  $\theta^* = 90^\circ$ .

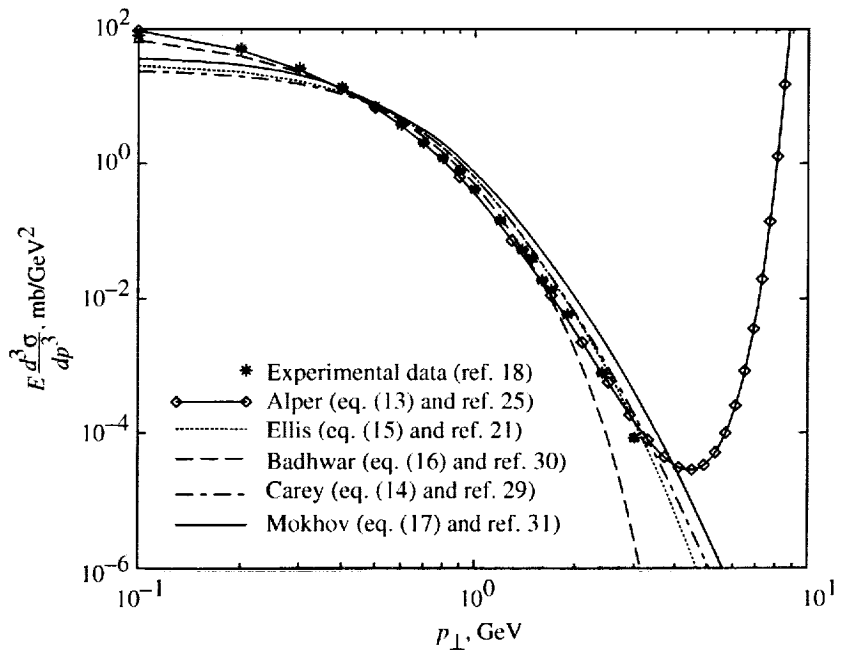


Figure 98. LIDCS plotted against transverse momentum for  $\pi^-$  production for  $E_{cm} = 31$  GeV and  $\theta^* = 90^\circ$ .

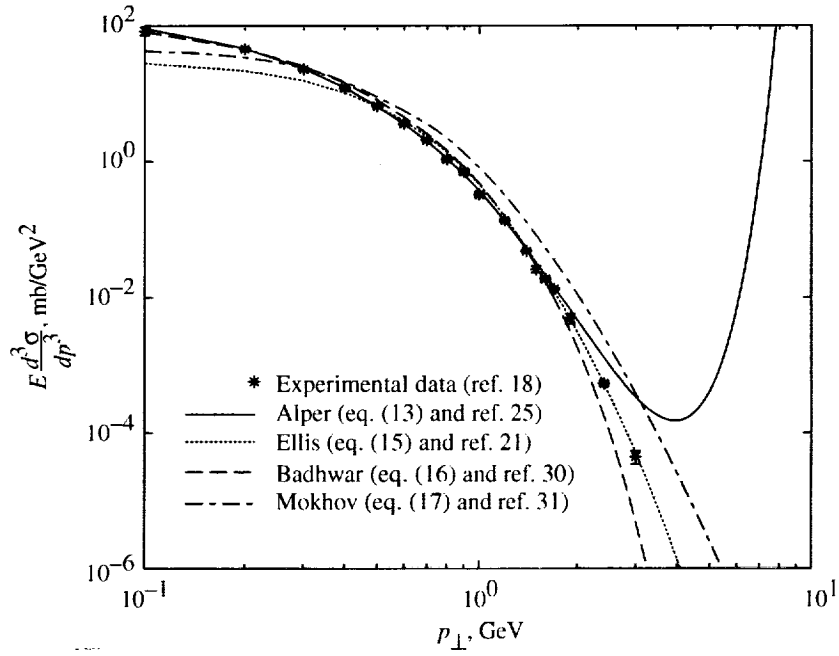


Figure 99. LIDCS plotted against transverse momentum for  $\pi^+$  production for  $E_{cm} = 23$  GeV and  $\theta^* = 90^\circ$ .

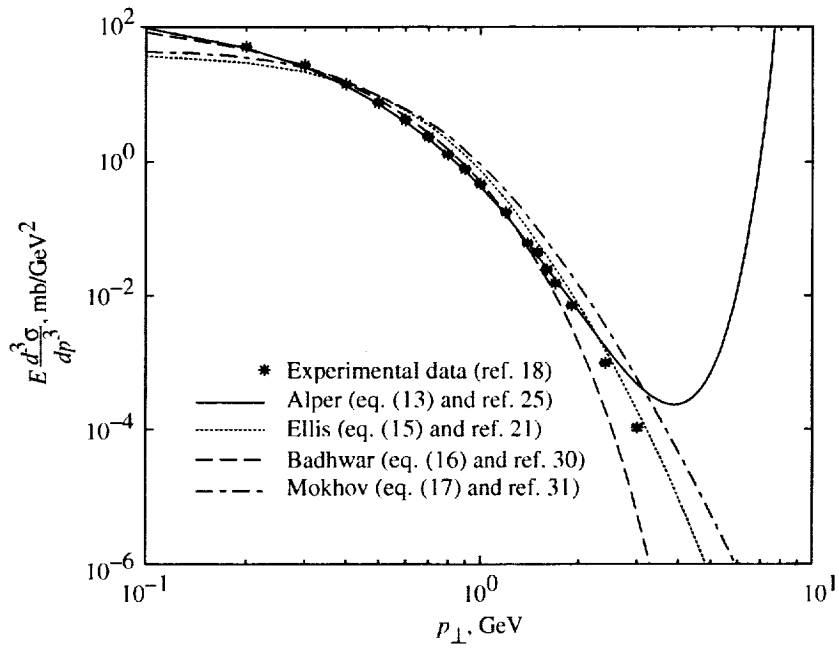


Figure 100. LIDCS plotted against transverse momentum for  $\pi^+$  production for  $E_{cm} = 31$  GeV and  $\theta^* = 90^\circ$ .

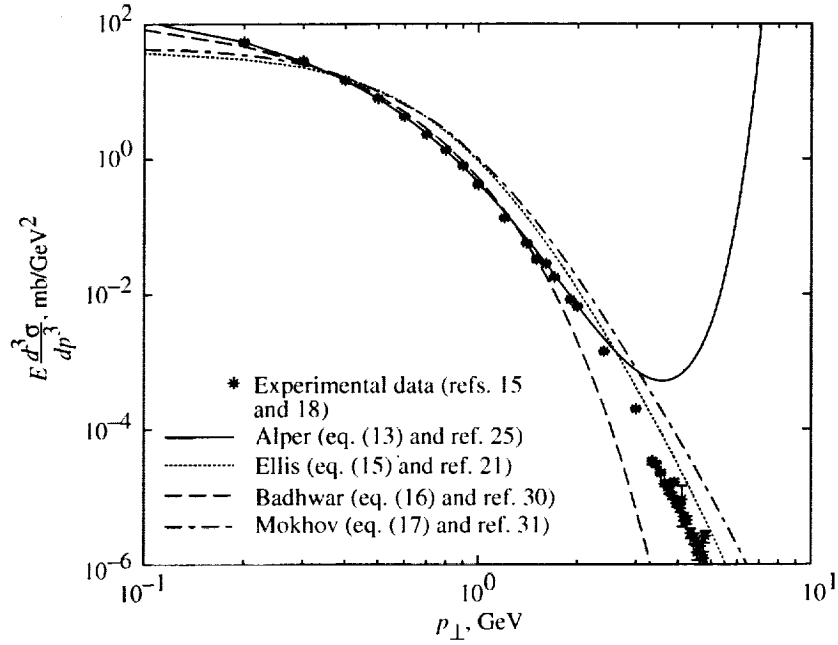


Figure 101. LIDCS plotted against transverse momentum for  $\pi^+$  production for  $E_{cm} = 45.0$  GeV and  $\theta^* = 90^\circ$  with data at  $E_{cm} = 45.0$  and  $44.8$  GeV.

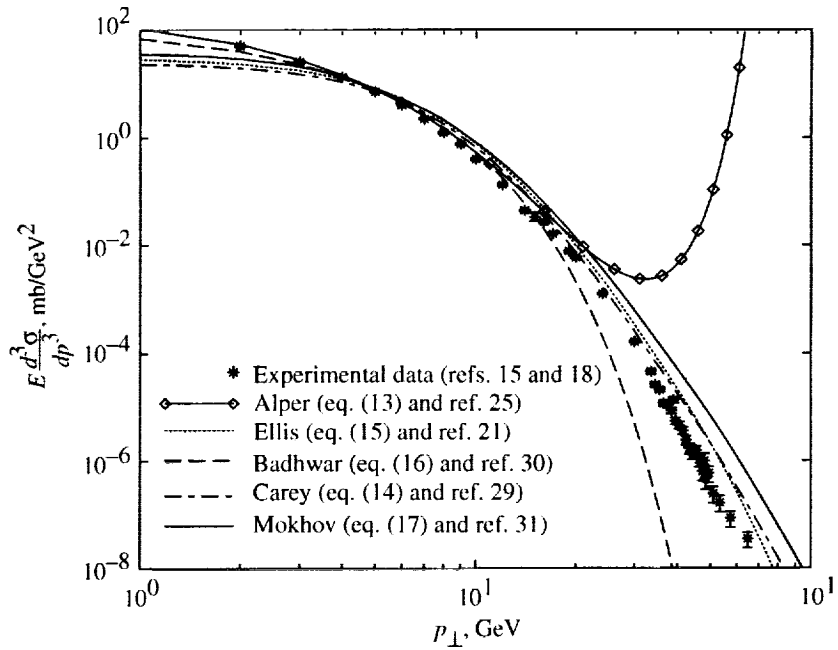


Figure 102. LIDCS plotted against transverse momentum for  $\pi^+$  production for  $E_{cm} = 45.0$  GeV and  $\theta^* = 90^\circ$  with data at  $E_{cm} = 45.0$  and  $44.8$  GeV.

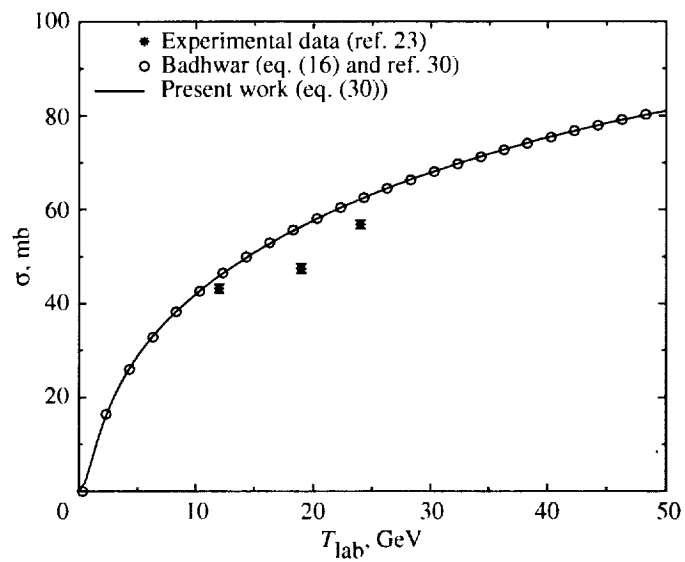


Figure 103. Parameterizations of total  $\pi^+$  production cross section plotted with numerically integrated LIDCS parameterizations.

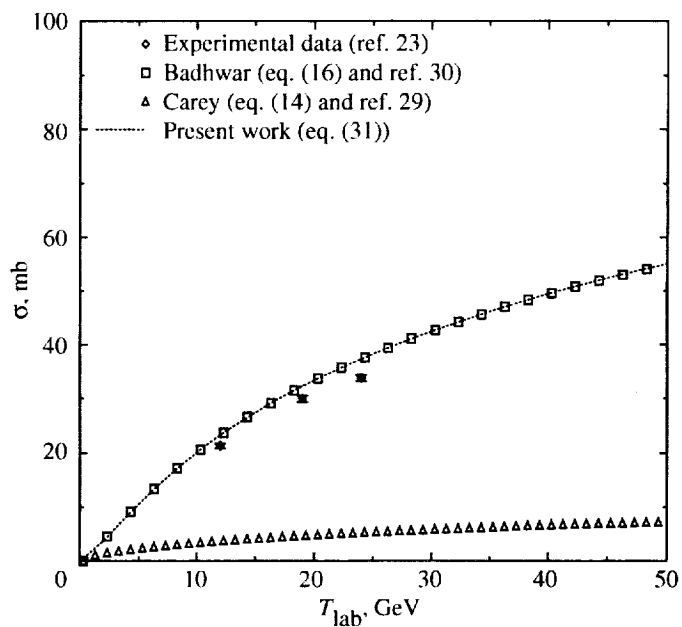


Figure 104. Parameterizations of total  $\pi^-$  production cross section plotted with numerically integrated LIDCS parameterizations.

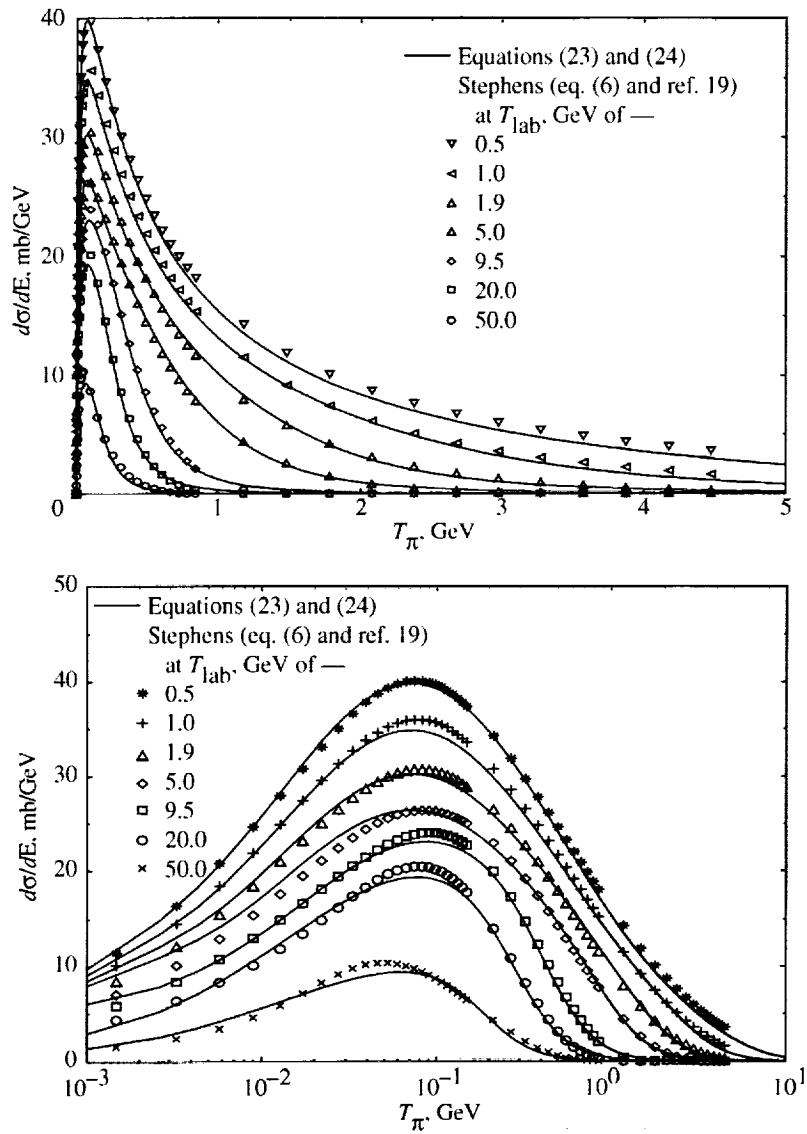


Figure 105.  $\pi^0$  spectral distributions. For detailed comparison, the horizontal axis is plotted both linearly (upper figure) and logarithmically (lower figure).

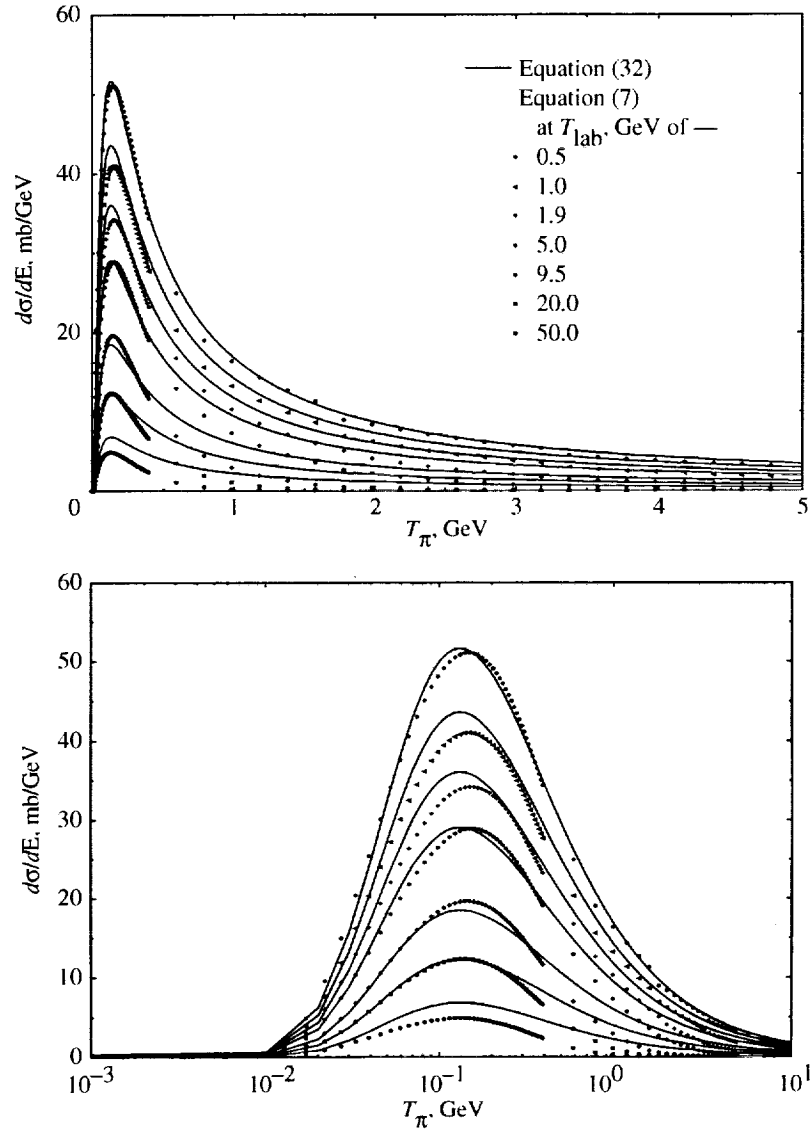


Figure 106.  $\pi^0$  spectral distributions. For comparison, horizontal axis is plotted both linearly (upper figure) and logarithmically (lower figure).

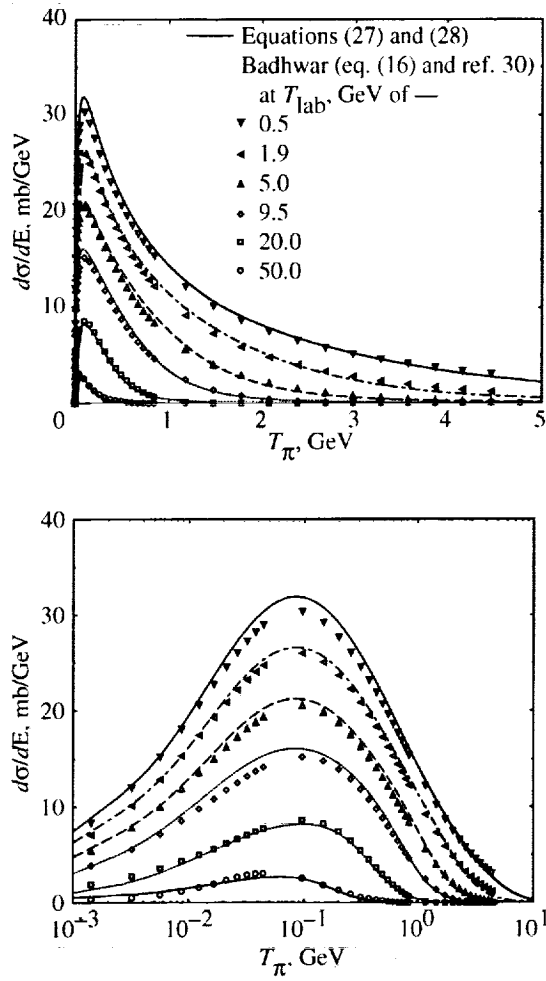


Figure 107.  $\pi^-$  spectral distributions. For comparison, horizontal axis is plotted both linearly (upper figure) and logarithmically (lower figure).

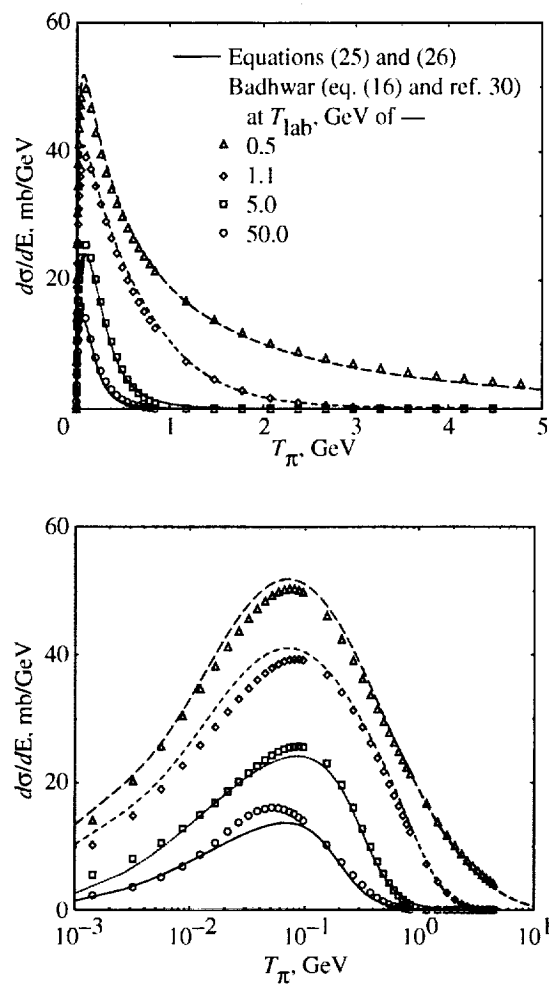


Figure 108.  $\pi^+$  spectral distribution. For comparison, horizontal axis is plotted linearly (upper figure) and logarithmically (lower figure).

REPORT DOCUMENTATION PAGE			Form Approved OMB No. 0704-0188	
Public reporting burden for this collection of information is estimated to average 1 hour per response, including the time for reviewing instructions, searching existing data sources, gathering and maintaining the data needed, and completing and reviewing the collection of information. Send comments regarding this burden estimate or any other aspect of this collection of information, including suggestions for reducing this burden, to Washington Headquarters Services, Directorate for Information Operations and Reports, 1215 Jefferson Davis Highway, Suite 1204, Arlington, VA 22202-4302, and to the Office of Management and Budget, Paperwork Reduction Project (0704-0188), Washington, DC 20503				
1. AGENCY USE ONLY (Leave blank)	2. REPORT DATE December 2000	3. REPORT TYPE AND DATES COVERED Technical Publication		
4. TITLE AND SUBTITLE Parameterized Cross Sections for Pion Production in Proton-Proton Collisions			5. FUNDING NUMBERS WU 101-21-23-03	
6. AUTHOR(S) Steve R. Blattnig, Sudha R. Swaminathan, Adam T. Kruger, Moussa Ngom, John W. Norbury, and R. K. Tripathi				
7. PERFORMING ORGANIZATION NAME(S) AND ADDRESS(ES) NASA Langley Research Center Hampton, VA 23681-2199			8. PERFORMING ORGANIZATION REPORT NUMBER L-18021	
9. SPONSORING/MONITORING AGENCY NAME(S) AND ADDRESS(ES) National Aeronautics and Space Administration Washington, DC 20546-0001			10. SPONSORING/MONITORING AGENCY REPORT NUMBER NASA/TP-2000-210640	
11. SUPPLEMENTARY NOTES Blattnig, Swaminathan, Kruger, Ngom, Norbury: University of Wisconsin-Milwaukee, Milwaukee, WI; Tripathi: Langley Research Center, Hampton, VA.				
12a. DISTRIBUTION/AVAILABILITY STATEMENT Unclassified-Unlimited Subject Category 93 Availability: NASA CASI (301) 621-0390			12b. DISTRIBUTION CODE Distribution: Standard	
13. ABSTRACT (Maximum 200 words) An accurate knowledge of cross sections for pion production in proton-proton collisions finds wide application in particle physics, astrophysics, cosmic ray physics, and space radiation problems, especially in situations where an incident proton is transported through some medium and knowledge of the output particle spectrum is required when given the input spectrum. In these cases, accurate parameterizations of the cross sections are desired. In this paper much of the experimental data are reviewed and compared with a wide variety of different cross section parameterizations. Therefore, parameterizations of neutral and charged pion cross sections are provided that give a very accurate description of the experimental data. Lorentz invariant differential cross sections, spectral distributions, and total cross section parameterizations are presented.				
14. SUBJECT TERMS Proton-proton collision; Lorentz invariant differential cross section; Spectral distributions; Total cross section parameterizations			15. NUMBER OF PAGES 85	
			16. PRICE CODE A05	
17. SECURITY CLASSIFICATION OF REPORT Unclassified	18. SECURITY CLASSIFICATION OF THIS PAGE Unclassified	19. SECURITY CLASSIFICATION OF ABSTRACT Unclassified	20. LIMITATION OF ABSTRACT UL	